ADVERTIMENT. L'accés als continguts d'aquesta tesi doctoral i la seva utilització ha de respectar els drets de la persona autora. Pot ser utilitzada per a consulta o estudi personal, així com en activitats o materials d'investigació i docència en els termes establerts a l'art. 32 del Text Refós de la Llei de Propietat Intel·lectual (RDL 1/1996). Per altres utilitzacions es requereix l'autorització prèvia i expressa de la persona autora. En qualsevol cas, en la utilització dels seus continguts caldrà indicar de forma clara el nom i cognoms de la persona autora i el títol de la tesi doctoral. No s'autoritza la seva reproducció o altres formes d'explotació efectuades amb finalitats de lucre ni la seva comunicació pública des d'un lloc aliè al servei TDX. Tampoc s'autoritza la presentació del seu contingut en una finestra o marc aliè a TDX (framing). Aquesta reserva de drets afecta tant als continguts de la tesi com als seus resums i índexs.

ADVERTENCIA. El acceso a los contenidos de esta tesis doctoral y su utilización debe respetar los derechos de la persona autora. Puede ser utilizada para consulta o estudio personal, así como en actividades o materiales de investigación y docencia en los términos establecidos en el art. 32 del Texto Refundido de la Ley de Propiedad Intelectual (RDL 1/1996). Para otros usos se requiere la autorización previa y expresa de la persona autora. En cualquier caso, en la utilización de sus contenidos se deberá indicar de forma clara el nombre y apellidos de la persona autora y el título de la tesis doctoral. No se autoriza su reproducción u otras formas de explotación efectuadas con fines lucrativos ni su comunicación pública desde un sitio ajeno al servicio TDR. Tampoco se autoriza la presentación de su contenido en una ventana o marco ajeno a TDR (framing). Esta reserva de derechos afecta tanto al contenido de la tesis como a sus resúmenes e índices.

WARNING. Access to the contents of this doctoral thesis and its use must respect the rights of the author. It can be used for reference or private study, as well as research and learning activities or materials in the terms established by the 32nd article of the Spanish Consolidated Copyright Act (RDL 1/1996). Express and previous authorization of the author is required for any other uses. In any case, when using its content, full name of the author and title of the thesis must be clearly indicated. Reproduction or other forms of for profit use or public communication from outside TDX service is not allowed. Presentation of its content in a window or frame external to TDX (framing) is not authorized either. These rights affect both the content of the thesis and its abstracts and indexes.

UNIVERSITAT POLITÈCNICA DE CATALUNYA
PROGRAMA DE DOCTORAT D'ENGINYERIA CIVIL

DEPARTAMENT DE MATEMÀTICA APLICADA III

NUMERICAL APPROACH FOR MODELING STEEL FIBER REINFORCED CONCRETE

by ALBA PROS PARÉS

Doctoral Thesis
Advisors: Pedro Díez and Climent Molins

Barcelona, 2011

Als meus pares, al Sergi

i especialment a l'Uri

Abstract

Numerical approach for modeling
Steel Fiber Reinforced Concrete

Alba Pros Parés

One alternative to overcome the main drawbacks of plain concrete in tension (its brittleness and weakness) is Steel Fiber Reinforced Concrete (SFRC), a technique introduced in the 70's, which consists of adding steel fibers into the concrete matrix. Due to the presence of the steel fibers into the concrete matrix, the residual strength and the energy dissipation of the material increase. Moreover, once a crack appears in the concrete, the steel fibers sew this fissure. The shape, the length and the slenderness of the fibers influence on the SFRC behavior. Moreover, the distribution and the orientation of the fibers into the concrete domain must be taken into account for characterizing the material.

In order to characterize the behavior of SFRC, a numerical tool is needed. The aim is to simulate the most standard and common tests and more complex setups.

This thesis proposes a numerical tool for modeling SFRC avoiding homogenized models (not accurate enough) and conformal meshes (too expensive). Therefore, the numerical tool accounts for the actual geometry of the fibers, discretized as 1D bars nonconformal with the concrete bulk mesh (2D or 3D domains). The two materials, corresponding to the concrete bulk and the fiber cloud, are defined independently, but coupled by imposing displacement compatibility. This compatibility is enforced following the ideas of the Immersed Boundary methods.

Two different models are considered for modeling the concrete bulk (a continuous one and a discontinuous one). The parametric study of each model is done for only plain concrete, before the addition of the steel fibers.

A phenomenological mesomodel is defined for modeling steel fibers, on the basis of the analytical expressions describing the pullout tests. This phenomenological mesomodel not only describes the behavior of the steel fibers, but also accounts for

the concrete-fiber interaction behavior. For each fiber, its constitutive equation is defined depending on its shape (straight or hooked) and the angle between the fiber and the normal direction of the failure pattern.

Both 2D and 3D examples are reproduced with the proposed numerical tool. The obtained results illustrate the presence of the steel fibers into the concrete matrix. The shape of the fiber influences of the SFRC behavior: the residual strength is higher for hooked fibers than for straight ones. Moreover, increasing the quantity of fibers means increasing the residual strength of the material.

The obtained numerical results are compared to the experimental ones (under the same hypothesis). Therefore, the proposed numerical approach of SFRC is validated experimentally.

Acknowledgments

While there only appears one author, this thesis has been developed in collaboration with many people. Therefore, I am indebted to a number of people and I wish to express my gratitude to all of them.

First of all I would like to thank Pedro Díez and Climent Molins for their advise, guidance and patience during this years. Their unconditional support and help have been essential for me. Both in the professional and personal field I have learned a lot of things from them. Thanks for all their hours dedicated to me and this thesis. I will always be indebted to them.

Pedro, I have already understood the sentence ”que funcioni no vol dir que estigui bé!”. Although I am the mathematician, thank you for all your mathematical advise.

Climent, you have been my engineering guide. All I know about engineering is due to of our conversations. Thank you for your ”has de ser més sistemàtica”.

Many thanks to Professor Antonio Huerta, who allowed me to be a member of LaCàN group and provided me the excellent framework for the everyday work. Moreover, I am very grateful with all the members of the LaCàN group for all these years together. All your comments and suggestions (mainly in the NMASE's) have been really useful and interesting for me. All my technical problems have been reduced thanks to David Ortin and Xevi Roca.

I would like to show my gratitude to all the members of the tribunal and the referees. Although it is difficult to find a blank in their crowded agendas, many thanks for their time and dedication.

Tots els de la sala de gràfics i els de dins heu aconseguit que cada dia fos un plaer anar a treballar. Gràcies per tots els comentaris científics, però encara més gràcies per tota la resta: els cafès, els dinars, els consells, les eternes converses,... Entre tots, hem fet una gran família. Gràcies Eloi per venir a la meva taula sempre que ho he necessitat, sembla que fer anar l'inkscape (i tota la resta de programes) amb tu al costat sigui més fàcil. I especialment, gràcies Elena per ser el meu pilar en tots els aspectes dins de la sala tots aquests anys!

Els meus amics (de mates i de Molins) m'han fet costat i m'han donat el seu suport al llarg de la tesis. Compartint estones amb ells (cafès, birres, esmorzars, dinars, berenars, sopars, festes, xerrades, running,...), he aconseguit oblidar els mals de cap de la tesis. A més, respondre preguntes com "què fas a la teva feina?" o "què té a veure el formigó amb les mates?" m'ha ajudat a entendre moltes coses de les que faig.

Moltes gràcies a tota la meva família per entendre i respectar el que faig. Als avis per suposar sempre que tot em va bé i creure en mi de manera incondicional. Però sobretot gràcies al Sergi i als pares per haver estat amb mi sempre, al meu costat. Gràcies per no deixar que em rendeixi mai! Tot el que he aconseguit i sóc us ho dec a vosaltres.

Finalment, només em queda donar-li les gràcies a l'Oriol. Uri, tu has fet que fos valenta. Gràcies pel teu suport incondicional, per ser-hi i per aconseguir sempre que tot el que és difícil sigui una mica més fàcil.

Contents

List of Figures

List of Tables

Chapter 1

Introduction

1.1 Motivation

Reinforced and prestressed concrete are the most common and used techniques for overcoming the main drawbacks of plain concrete (its brittleness and weakness under tension). Another alternative, presented in the 70's, is Steel Fiber Reinforced Concrete (SFRC), a technique which consists of adding steel fibers into the plain concrete matrix, as another component of the concrete mixture.

Due to the presence of the steel fibers into the concrete matrix, the energy dissipation and the residual strength of the material increase, particularly, in tension. Moreover, once the concrete matrix fractures, the steel fibers bridge the cracks.

SFRC has a large range of applications in civil engineering: bridges, pipes, airport runways, tunnel linings, pavements,... The use of SFRC significantly reduces the handling labor of construction (compared to the conventional reinforced concrete).

Apart form the concrete matrix properties, for characterizing the behavior of SFRC, the length, the shape and the slenderness of the steel fibers must be taken into account. Moreover, the orientation and the distribution of the steel fibers in the concrete matrix have strong influence on the response of the material.

The methods for characterizing SFRC and the quality control of the material properties clearly deserve further development. There is a current need of improving these methodologies in order to satisfy the individual request of further using of SFRC with increasing structural responsibilities.

A number of direct and indirect tests are used to determine the tensile behavior of SFRC. Bending tests of prismatic beam specimens are the most used to characterize the post-cracking response of SFRC. These can be either based on 3-point tests (EN-14651 (2005), RILEM-TC162-TDF (2003e)) or 4-point tests (NBN-B-15-238 (1992)). Other methods have also been used for the material characterization; some of them are indirect tension tests -splitting test (Tschegg and Linsbauer (1986)) and Barcelona test (Molins et al. (2009), UNE 83515 (2010))- and direct tension tests (RILEM-TC162-TDF (2001)). Barcelona test is the extension of the double punch test (DPT) (Molins et al. (2009)) to study the postcracking response of SFRC. In spite of being the uniaxial tensile test the more direct approach to characterize SFRC in tension, it presents difficulties inherent to their execution which hugely limit their use and current application (Barragán (2002)) and the number of available results. It is mainly used for research purposes.

For characterizing the response of SFRC considering the mentioned tests and in more complex setups, a numerical approach for describing SFRC is necessary.

The initial main objective of this research was simulating numerically the Barcelona test, namely, the Double Punch Test considering SFRC. Currently, the numerical tool for simulating SFRC tests is already available. Simulating the Barcelona test is the next application.

1.2 Objectives of the thesis

The main aim of this thesis is to develop a numerical approach for modeling SFRC allowing to simulate efficiently the most common standard tests considering SFRC. In this scenario, the following partial goals are considered:

- **Simulate standard tests considering only plain concrete:** before simulating different standard tests with SFRC and based on the state of the knowledge, the goal is to model plain concrete considering different material models.

Namely, both a continuous model and a discontinuous model are considered for characterizing plain concrete.

- **Set the material parameters of the models for plain concrete:** the material parameters of the chosen models for plain concrete must be calibrated for each different test. Thus, the obtained results for plain concrete can be validated with experimental results.
- **Develop the numerical tool for SFRC:** the objective is to define a numerical idea for coupling the two materials (concrete bulk and fiber cloud) accounting for the actual distribution of the fibers into the concrete matrix. Moreover, the aim is to define the mesh corresponding to the steel fibers nonconformal (without geometrical matching) with the concrete matrix discretization.
- **Reproduce the standard tests with SFRC:** considering the proposed numerical approach, the most common standardized tests aim to be reproduced considering SFRC. The presented tool must be applied considering both two and three dimensional meshes corresponding to the concrete bulk.
- **Validate the numerical tool for SFRC:** the results obtained simulating standard tests considering SFRC must be compared to experimental results available in different experimental campaigns. Therefore, the goal is to validate the proposed numerical approach.

1.3 Outline

The thesis is divided into five main parts: the motivations, the numerical models for plain concrete, the numerical approach for modeling SFRC, the three dimensional extension of the tool with the numerical results and validation and the most important concluding remarks and the future work.

Part I: Motivations. The introduction of the thesis (chapter 1) and the state of the art (chaper 2) correspond to the first part of the thesis, playing the role of the motivations for the rest of the thesis.

Part II: Numerical modeling of plain concrete. The numerical approach for modeling plain concrete accounts for considering two different material models for modeling plain concrete (a continuous one and a discontinuous one). The material parameters of each model must be calibrated for being able to reproduce standard tests. Indeed chapter 3 refers to the numerical modeling of plain concrete simulating the Double Punch Test and corresponds to the paper *Numerical Modeling of Double Punch Test for plain concrete* by Pros et al. (2011b). The test chosen for calibrating the material parameters in chapter 3 is the Double Punch Test, due to our first objective of the thesis. However, the parameter calibration can be used for all the tests.

Part III: The numerical approach for SFRC. Chapter 4 corresponds to the formulation of the numerical tool for SFRC. Two dimensional examples are presented. The ideas and the results presented are indeed presented in the paper *Modeling Steel Fiber Reinforced Concrete: numerical Immersed Boundary approach and a phenomenological mesomodel for concrete-fiber interaction* by Pros et al. (2011a).

Part IV: 3D extension of the numerical tool with experimental validation. The extension of the numerical tool for SFRC is presented in chapter 5 with the reproduction of some standard tests (using 3D meshes and realistic distribution of the fibers). Moreover, the obtained results are compared to experimental results (from different campaigns) in order to validate the numerical tool.

Part V: Conclusions and future work. Finally, in Chapter 6 the most important concluding remarks are summarized, followed by some open points which can be developed in the future.

Finally, at the end of this thesis three appendices are included. The full details of the deduction of the constitutive equations describing the behavior of the steel fibers are described in Appendix A. The study of the stability of the proposed numerical tool for modeling SFRC is explained in Appendix B. In Appendix C, the main contributions related to this thesis are presented: the talks in congress and the papers.

Chapter 2

State of the art

2.1 Introduction

This chapter aims at reviewing available literature concerning all the aspects studied during the thesis. Thus, the state of the art is focused in three different points: (1) experimental tests for characterizing both plain concrete and SFRC, (2) alternatives for modeling plain concrete and (3) numerical tools for modeling SFRC.

2.2 Experimental tests characterizing plain concrete and SFRC

Several experimental tests are commonly used for characterizing both plain concrete and SFRC. The most standard tests are described in the following:

- **Pullout tests** (Laranjeira et al. (2010a),Laranjeira et al. (2010b)) consist of a plain concrete specimen with only one steel fiber immersed on it which is pulled out (figure 2.1).

  Pullout tests describe all the phenomena of the SFRC not only for straight fibers (fiber debonding, matrix spalling, frictional sliding and fiber removal), but also for hooked fibers (which are the same for the case of straight fibers but, with

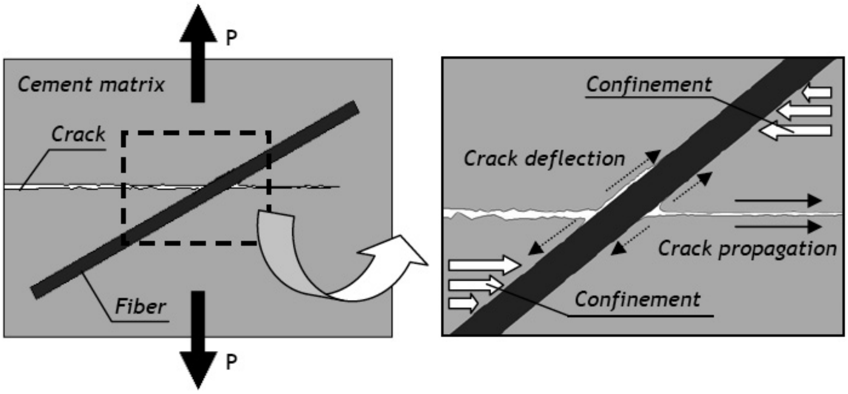

Figure 2.1: Pullout test scheme (Laranjeira et al. (2010a))

plastic deformations, magnifying the matrix spalling effects).

Fiber pullout tests have been used to characterize and optimize the bond strength on fiber reinforced concrete for decades because they allow evaluating the crack bridging capacity provided by fibers in brittle cementitious matrices. Moreover, the activation of toughening mechanisms in SFRC requires growing matrix crack to be deflected at the fiber-concrete interface which is represented by pullout tests. Therefore, the description of the pullout response covers the most significant phenomena with which crack bridging of SFRC can be explained. However, pullout and bond-slip relations are sensitive to fiber orientation. Thus, different orientations of the fibers must be taken into account in order to capture the whole interaction process.

- **Splitting test** is an indirect tension test (defined by Carneiro and Barcelos (1953) for plain concrete (also known as Brazilian test) and by Tschegg and Linsbauer (1986) considering SFRC) which consists of compressing a plain concrete cylinder placed horizontally by two steel plates (figure 2.2). The fracture pattern is a diametral vertical plane located in the middle of the cylinder.

  The tensile strength (f_t) of plain concrete and SFRC is measured indirectly through the obtained maximum vertical load. In chapter 3, the expression to obtain f_t is presented.

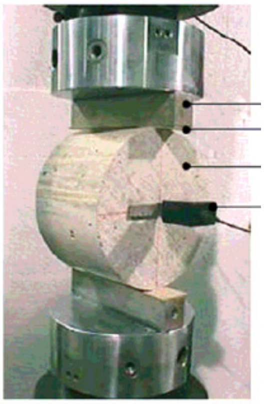

Figure 2.2: Scheme of the splitting test (Carmona et al. (1998))

- **Direct tension test** (RILEM-TC162-TDF (2001); Barragán (2002)) consists of a cylindrical specimen which is pulled axially (figure 2.3). Due to the brittleness of plain concrete in tension, a notch is typically performed in the middle of the specimen to enforce the crack always in the same place. Moreover, this brittleness in tension makes the direct tension test experimentally difficult to perform.

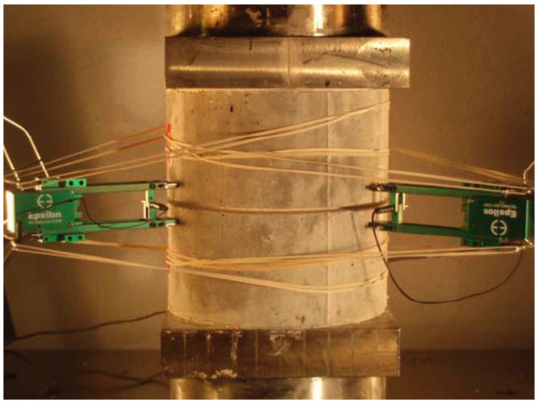

Figure 2.3: Scheme of the direct tension test (Laranjeira (2010))

In this case, an expression giving the relation between the obtained maximum vertical load and the residual strength of the material also exists and it is explained in chapter 3 too.

- **Three point bending test** is a bending test (figure 2.4) using a prismatic beam specimen loaded at the mid span (EN-14651 (2005); RILEM-TC162-TDF (2000)), which measures the flexural strength.

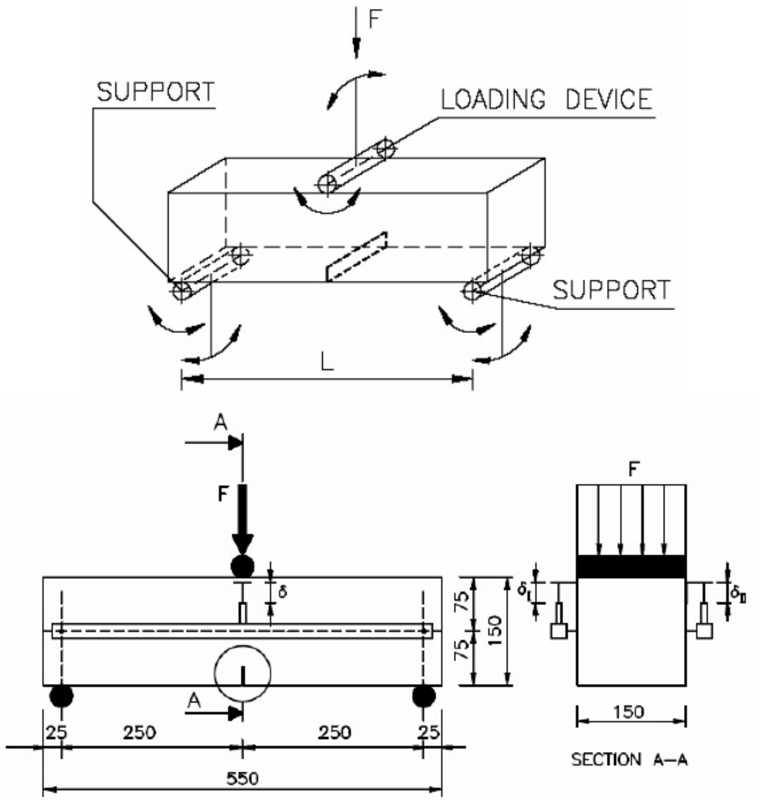

Figure 2.4: Scheme of the three point bending test (EN-14651 (2005))

- **Four point bending test** consists of a prismatic beam specimen placed horizontally, similar to the three point bending test, but with two loads applied each at one third of the span (figure 2.5). A Belgian standard (NBN-B-15-238 (1992)) and an American one (ASTMC-1018 (1992)) correspond to the four point bending layout.
- **Double punch test (DPT)** (introduced by Chen (1970); Chen and Yuan (1980); Chen and Tumbauer (1972)) consists in compressing axially a cylindrical concrete specimen with two steel circular punches centered at the top and the bottom of the specimen (figure 2.6). The geometry of the specimen is given by the height (l = 15cm) and the diameter (d = 15cm). The ratio between the

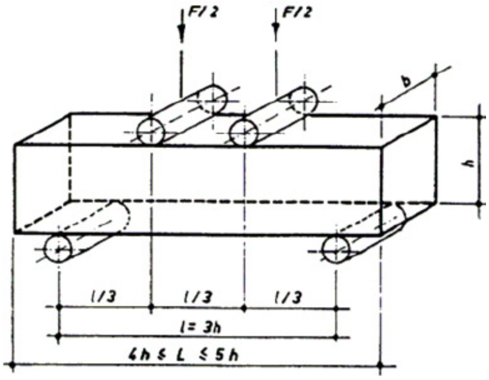

Figure 2.5: Scheme of the four point bending test (NBN-B-15-238 (1992))

diameters of the punches and the specimen is one fourth ($d' = \frac{1}{4}d = 3.75$cm). Occasionally, smaller specimens with identical geometrical proportions are used to study the influence of size effect (Chen and Yuan (1980)), concluding that the tensile strength interpreted from the DPT is relatively insensitive to the size of the specimen.

Figure 2.6: Scheme of the double punch test (Guàrdia (2007))

The DPT is used to indirectly measure the tensile strength of plain concrete, f_t. Indirect measures of tensile strength (Brazilian test, DPT, 3 and 4 point bending test,...) are often preferred to direct uniaxial tests because (1) they show a reduced scattering of the results, (2) they are easier to perform and (3) they do not suffer from the lack of uniformity of the stress distribution in the cross section of the specimen.

In the literature, the value of the tensile strength of plain concrete measured through the DPT, has been object of study by Chen and Yuan (1980); Bortolotti (1988); Marti (1989); Molins et al. (2007). These expressions are explained in chapter 3.

The extension of the DPT to assess the after cracking capacity of SFRC, the so called *Barcelona Test*, was introduced by Molins et al. (2007, 2009).

2.3 Models for plain concrete

For modeling plain concrete, several models can be chosen depending on the aims and the problems to be studied. As presented by Oliver et al. (2002); Jirásek (1998); Simone (2003), beyond a limited elastic range, macroscopical discontinuities appear in plain concrete as a mechanical response to extreme loading conditions. This behavior is called softening. The numerical approaches to model this nonlinear mechanical behavior can be classified as follows:

- **Cohesive crack model:** admits the presence of strong discontinuities, that is, jumps in the displacement field, and describes softening by a tension-separation law, which relates the tension stresses transmitted by the crack to the crack opening. A complete description of these models is presented by Planas et al. (2003).
- **Crack band model:** represents the region of localized deformation by a band of a small but finite thickness, separated from the remaining part of the body by two weak discontinuities, that is, curves or surfaces across which certain strain components have a jump, but the displacement field remains continuous. The theory of the crack band model for concrete is defined by Bažant and Oh (1983).
- **Continuum mechanics approach:** leads to continuously differentiable displacement field and the strain field remains continuous (as explained by Jirásek

(1998)). However, strain localization is manifested and it is necessary to regularize the model. Different models available in the literature are continuum mechanics approaches: damage models, plasticity, visco-elasticity, strong discontinuities,... In this thesis, a damage model is chosen as a continuous approach.

- **Discontinuous mechanics:** the discontinuous behavior of plain concrete is considered to be in the domain discretization (Oliver et al. (2002)). One possibility, for example, is to assume the failure pattern known *a priori* and discretize the problem domain taking into account the cracks (defining joint elements in this cracks). Another alternative, introduced by López et al. (1999), is based on considering all possible fracture paths modeled using joint elements allowing any possible failure direction.

Two alternatives are considered in the presented thesis: 1) a continuous model, the nonlocal Mazars damage model and 2) a discontinuous model based on joint elements.

2.3.1 Continuous approach: Damage Model

In the damage model chosen in this thesis, the constitutive equation is $\boldsymbol{\sigma} = (1-D)\mathbb{C}\boldsymbol{\varepsilon}$, where D is a scalar parameter accounting for the damage and obeying $0 \leq D \leq 1$. If $D = 0$, the material is considered to be healthy and if $D = 1$, it is completely damaged. In the above, $\boldsymbol{\sigma}$ and $\boldsymbol{\varepsilon}$ stand for stress and strain tensor, respectively. Moreover, $\mathbb{C}$ is the elastic forth tensor.

Then, the constitutive equations are:

$$\boldsymbol{\varepsilon} = \frac{1}{E\left(1-D\right)}\left[\left(1+\mu\right)\boldsymbol{\sigma} - \mu Tr\left(\boldsymbol{\sigma}\right)\boldsymbol{I}\right] \tag{2.1}$$

$$\boldsymbol{\sigma} = \frac{E\left(1-D\right)}{1+\nu}\left[\boldsymbol{\varepsilon} + \frac{\nu}{1-2\nu}Tr\left(\boldsymbol{\varepsilon}\right)\boldsymbol{I}\right] \tag{2.2}$$

where E stands for the Young modulus of the material, ν represents the Poisson coeficient and μ is the Lamé constant.

The damage parameter depends on y, $D = D(y)$, which is called *state variable* and depends on the strain field, $y = y(\varepsilon)$. Commonly, the damage starts when the state variable reaches a threshold Y_0 and it always increases, that is,

$$D = 0 \text{ for } y \leq Y_0 \qquad\qquad \dot{D} \geq 0 \text{ for } y > Y_0 \tag{2.3}$$

Mazars Damage Model

The Mazars Damage Model, introduced by Mazars (1986), is characterized for considering the damage as a linear combination of the damage generated under tension, D_t, and the damage under compression, D_c: $D = \alpha_t D_t + \alpha_c D_c$. Moreover, the damage follows an exponential law. In this damage model, the state variable is defined as $y = \varepsilon$.

The Mazars model can be written as

$$D_t = 1 - \frac{Y_0(1 - A_t)}{\varepsilon} - A_t e^{-B_t(\varepsilon - Y_0)} \qquad\qquad \alpha_t = \sum_i \frac{\varepsilon_{ti}\langle\varepsilon_i\rangle}{\varepsilon^2} \tag{2.4}$$

$$D_c = 1 - \frac{Y_0(1 - A_c)}{\varepsilon} - A_c e^{-B_c(\varepsilon - Y_0)} \qquad\qquad \alpha_c = \sum_i \frac{\varepsilon_{ci}\langle\varepsilon_i\rangle}{\widehat{\varepsilon}^2} \tag{2.5}$$

with α_t and α_c are defined satisfying

$$\alpha_t + \alpha_c = 1 \tag{2.6}$$

and

$$\langle \varepsilon_i \rangle = \frac{\varepsilon_i + |\varepsilon_i|}{2} \tag{2.7}$$

$$\widehat{\varepsilon} = \sqrt{\sum_i \left(\frac{\varepsilon_i + \mid \varepsilon_i \mid}{2} \right)^2} \tag{2.8}$$

where ε_i are the main strains.

ε_{ti} and ε_{ci} are calculated following the next scheme: given the stress field ($\boldsymbol{\sigma}$), the principal stress field ($\boldsymbol{\sigma}_{prin}$) is calculated and divided into the positive part of the field ($\boldsymbol{\sigma}^+_{prin}$) and the negative one ($\boldsymbol{\sigma}^-_{prin}$). For each part (the positive and the negative), the process for finding the principal field is applied in the inverse sense for getting $\boldsymbol{\sigma}^+$ and $\boldsymbol{\sigma}^-$. Then, the corresponding strain fields are computed: $\boldsymbol{\varepsilon}^+$ and $\boldsymbol{\varepsilon}^-$ and the principal fields of these strain fields are calculated: $\boldsymbol{\varepsilon}^+_{prin}$ and $\boldsymbol{\varepsilon}^-_{prin}$. Finally, again, the process for finding the principal field is applied in the inverse sense given ε_{ti} and ε_{ci}:

$$\boldsymbol{\sigma} \rightarrow \boldsymbol{\sigma}_{prin} \begin{cases} \boldsymbol{\sigma}^+_{prin} \rightarrow \boldsymbol{\sigma}^+ \rightarrow \boldsymbol{\varepsilon}^+ \rightarrow \boldsymbol{\varepsilon}^+_{prin} \rightarrow \boldsymbol{\varepsilon}_{ti} \\ \\ \boldsymbol{\sigma}^-_{prin} \rightarrow \boldsymbol{\sigma}^- \rightarrow \boldsymbol{\varepsilon}^- \rightarrow \boldsymbol{\varepsilon}^-_{prin} \rightarrow \boldsymbol{\varepsilon}_{ci} \end{cases} \tag{2.9}$$

with $\boldsymbol{\sigma} = \boldsymbol{\sigma}^+ + \boldsymbol{\sigma}^-$ and $\boldsymbol{\varepsilon}_i = \boldsymbol{\varepsilon}_{ti} + \boldsymbol{\varepsilon}_{ci}$.

The parameters A_t, B_t, A_c, B_c and the threshold Y_0 are fixed depending on the actual material properties.

Nonlocal Mazars Damage Model

Up to this point, the damage has been calculated in each point depending on the state variable y at the same point, but this localization brings to a pathological mesh dependence and the results are not realistic. In order to solve this problem, a nonlocal damage model is considered, as introduced by Pijaudier-Cabot and Huerta (1991); Rodríguez-Ferran and Huerta (2000); Pijaudier-Cabot and Bažant (1991). The main idea of a nonlocal damage model (regularized damage model) is that the damage depends on the state variable in a neighborhood (associated to a characteristic length) of the current point, instead of depending on the state variable in the same point (as in a local model). Therefore a nonlocal state variable $\widehat{Y}$ is considered which is defined as an average of the state variable in a neighborhood of each point:

$$\widehat{Y} = \frac{\displaystyle\int_V \alpha(d) y \mathrm{d}V}{\displaystyle\int_V \alpha(d) \mathrm{d}V} \qquad \alpha(d) = e^{-\left(\frac{2d}{l_c}\right)^2} \tag{2.10}$$

where the weight function α depends on the distance d to the current point and l_c is the characteristic length. This is another material parameter and its function is to define the nonlocality. In general, the value of the characteristic length is such that the neighborhood of each point involves two or three elements of any mesh discretizing the problem. Therefore, the nonlocal damage is $D = D(\widehat{Y})$.

In the present work, the integral-type nonlocal formulation explained above is taken into account for the model regularization. However, as introduced by Jirásek (1998), there exist two other ways of nonlocalization. They are gradient formulations and instead of dealing with integrals that represent spatial interactions, they can take the microstructure into account by incorporating the influence of gradients of internal variables into the constitutive relations. In the following, they are presented.

- *Explicit gradient formulation:* the damage is assumed to be driven not only by the local state variable y, but also by its Laplacean, which represents the "curvature" of the strain distribution:

  $$\widehat{Y} = y + l^2 \bigtriangledown^2 y \tag{2.11}$$

  where l is a material parameter with the dimension of length.

- *Implicit gradient formulation:* due to the presence of second derivates of the state variable, the numerical implementation of the explicit gradient formulation is not easy. To overcome this problem, the implicit gradient formulation defines the nonlocal variable indirectly as the solution of the differential equation:

$$\widehat{Y} - l^2 \bigtriangledown^2 \widehat{Y} = y \tag{2.12}$$

with the homogeneous Neumann boundary condition $\boldsymbol{n} \cdot \bigtriangledown \widehat{Y} = 0$ imposed on the entire boundary.

2.3.2 Other continuous approaches

Apart form the damage models, other continuous models are available for modeling plain concrete, as observed by Oliver et al. (2002); Simone (2003).

Plasticity

The theory of plasticity is used usually to describe the elastoplastic material behavior. The basic assumption is the decomposition of the strain tensor into an elastic ($\boldsymbol{\varepsilon}^p$) and a plastic ($\boldsymbol{\varepsilon}^p$) part:

$$\boldsymbol{\varepsilon} = \boldsymbol{\varepsilon}^e + \boldsymbol{\varepsilon}^p. \tag{2.13}$$

Therefore, the stress tensor is defined as

$$\boldsymbol{\sigma} = \mathbb{C}(\boldsymbol{\varepsilon} - \boldsymbol{\varepsilon}^p). \tag{2.14}$$

The plastic strain rate $\dot{\boldsymbol{\varepsilon}}^p$ is postulated as

$$\dot{\boldsymbol{\varepsilon}}^p = \dot{\lambda} f_\sigma, \tag{2.15}$$

where the rate $\dot{\lambda}$ of the plastic strain multiplier λ determines the magnitude of the plastic flow and $f_\sigma = \dfrac{\partial f}{\partial \boldsymbol{\sigma}}$ is a tensor which indicates the direction of the plastic strain-rate.

The loading-unloading conditions are expressed using the Kuhn-Tucker relations:

$$\dot{\lambda} \geq 0, \quad f \leq 0, \quad \dot{\lambda} f = 0. \tag{2.16}$$

In ideal plasticity, the yield function is defined as

$$f(\boldsymbol{\sigma}) = \sigma_e(\boldsymbol{\sigma}) - \sigma_0, \tag{2.17}$$

where σ_e is the effective stress and σ_0 stands for the yield stress.

Softening and hardening behavior is introduced by making the yield stress a function of κ, a scalar measure of the plastic strain tensor: $f(\boldsymbol{\sigma}, \kappa)$.

Simone (2003) proposes to consider two different yield functions. On one hand, the classical von Misses yield function:

$$f(\boldsymbol{\sigma}, \kappa) = \sqrt{3\boldsymbol{J}_{\sigma 2}} - \overline{\sigma}(\kappa), \tag{2.18}$$

being $\overline{\sigma}(\kappa)$ the uniaxial yield stress and $\boldsymbol{J}_{\sigma 2} = \dfrac{1}{2}\boldsymbol{\sigma}^d : \boldsymbol{\sigma}^d$ stands for the second invariant of the deviatoric stress trensor $\boldsymbol{\sigma}^d$.

On the other hand, the Rankine yield function, which is more used to describe the cracking in quasi-brittle materials. It is a principal stress criterion characterized by a vertex in the principal stress space.

Nonlinear hyperelastic models

The hyperelasticity models refer to the materials which can experience large elastic strain that is recoverable.

Considering W as the strain energy density of the material, the constitutive equation of the nonlinear hyperelastic models, as studied by Oliver (2002), are defined as:

$$\boldsymbol{\sigma} = \frac{\partial W(\boldsymbol{\varepsilon})}{\partial \boldsymbol{\varepsilon}}. \tag{2.19}$$

Therefore,

$$\dot{\boldsymbol{\sigma}} = \frac{\partial^2 W(\boldsymbol{\varepsilon})}{\partial \boldsymbol{\varepsilon} \otimes \partial \boldsymbol{\varepsilon}} : \dot{\boldsymbol{\varepsilon}} = \mathbb{E}_T(\boldsymbol{\varepsilon}) : \dot{\boldsymbol{\varepsilon}}, \tag{2.20}$$

where $\mathbb{E}_T(\boldsymbol{\varepsilon})$ is positive definite.

2.3.3 Discontinuous approach: Joint model

Another way of describing discontinuities numerically, apart from the continuous approach, is defined in this section. As introduced by Díez and Pegon (2002); Beer (1985); Snyman et al. (1991), in the Finite Element analysis in solid mechanics, some situations present a discontinuous behavior between finite elements which can be modeled with joint elements. One example could be fractures in the material, like in plain concrete. For example, López et al. (1999) propose to model any possible crack path of the material with joint elements, taking into account the aggregates of the concrete. In this thesis, the idea is to consider only the fracture pattern, known *a priori*, modeled with joint elements, whereas the rest of the specimen is assumed to be elastic.

The nodes in the interface zone must be defined twice in order to define the joint elements, which will correspond to the duplicated geometry. Joint elements allow interfaces sliding and separating. The constitutive equations must incorporate both contact and noncontact conditions. When the interfaces are in contact, frictional sliding is possible, with dilatant behavior. The joint model is already incorporated into CAST3M, the standard nonlinear finite element code used in this thesis, and into some other commercial codes. It is easy because joint elements use the same type of nodal quantities as the continuous elements.

Any constitutive equation modeling a joint element in a three-dimensional problem has three components. The first one corresponds to the joint plane normal direction and the other two are the tangential directions of the plane. The normal one corresponds to the contact or separation between the joint interfaces. Moreover, the ones in the joint plane correspond to the slide directions.

The nonlinear behavior of joints is characterized by slide and separation taking place at the joint plane. For a joint with no tensile strength, separation of joint planes will occur when the strain normal to the joint plane becomes positive. Alternatively, a tensile strength can be given to the joint. If the shear strength of the joint is exceeded, irreversible slide occurs.

The Mohr-Coulomb Joint model, for example, can be used to model the collapse pattern of plain concrete. Therefore, the governing equations of the joint model are written as

$$\sigma = k_{n1} \cdot u \quad \text{if} \quad \frac{-f_c}{k_{n1}} \leq u \leq u_0 \tag{2.21}$$

$$\sigma = (k_{n1} \cdot u_0 - k_{n2} \cdot u_0) + k_{n2} \cdot u \quad \text{if} \quad u \geq u_0 \tag{2.22}$$

$$\tau = -\tau_{max} \quad \text{if} \quad \frac{-\tau_{max}}{k_s} \leq v \tag{2.23}$$

$$\tau = k_s \cdot v \quad \text{if} \quad \mid v \mid \leq \mid \frac{\tau_{max}}{k_s} \mid \tag{2.24}$$

$$\tau = \tau_{max} \quad \text{if} \quad v \geq \frac{\tau_{max}}{k_s} \tag{2.25}$$

where $\tau_{max} = c + \sigma \tan(\varphi)$.

Table 2.1: Parameters of the model

Description	Symbol
first normal stiffness	k_{n1}
second normal stiffness	k_{n2}
displacement threshold from k_{n1} to k_{n2}	u_0
shear stiffness	k_s
maximum compression strength	f_c
cohesion	c
friction angle	φ

In equations (2.21)-(2.25), stresses applied are divided into two components (normal, τ, and shear, σ), and the displacements are also divided into u and v, corresponding to σ and τ, respectively. Moreover, in table 2.1, the relation between each parameter of the model and its meaning is presented.

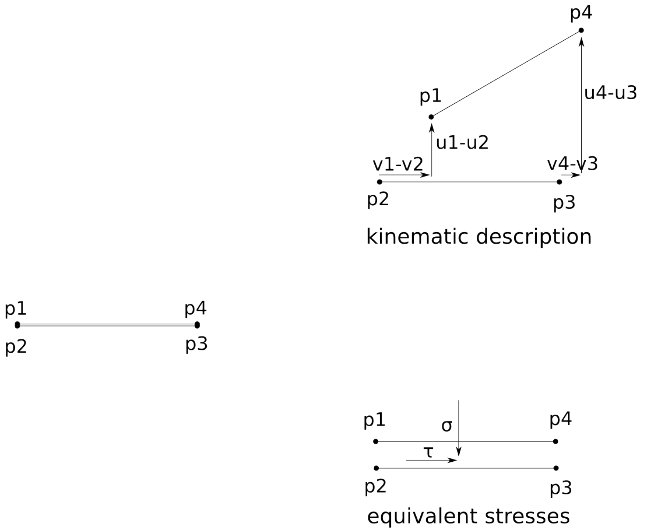

Figure 2.7: Stresses applied to a joint model and its displacements

In figure 2.7, it is shown (a) the relationship between stresses and displacements and (b) joint elements defined twice. There will be a normal component and two shear components with the same behavior, but in an orthogonal direction. Moreover, figure 2.8 reflects this constitutive law using two graphics: the normal and shear stresses.

2.4 Numerical strategies to model SFRC

A number of authors have recently introduced new models for SFRC. For instance, a numerical model considering an elasto-plastic material model for plain concrete with an exponential softening law turning into a linear softening law once all the fibers are activated is presented by Hofstetter et al. (2005). The crack propagation in SFRC considering a fracture mechanics approach is simulated by Zhang and li (2004).

On the other hand, Schumacher (2006) adapted the Compressive Damage Zone model (which is defined for plain concrete (Markeset and Hillerborg (1995))) for SFRC, adding extra parameters corresponding to steel fibers. The same author studies the

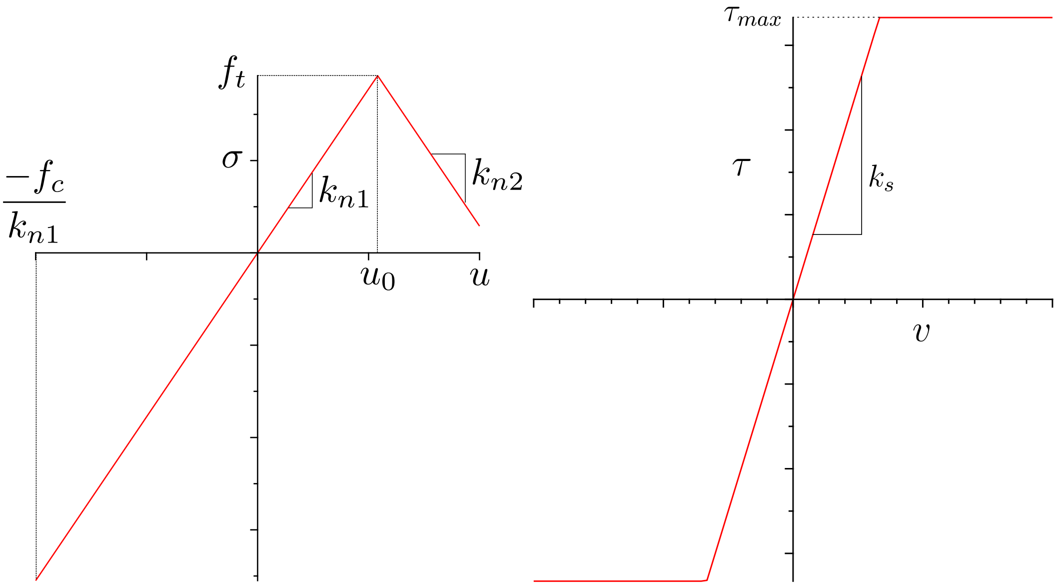

Figure 2.8: σ and τ evolution depending on the displacements

tensile behavior of SFRC considering a numerical model presented by Konig and Kutzing (1999). The orientation of the fibers is also studied by Schumacher (2006), considering a concrete specimen with a steel bar and a quantity of fibers. The discretization of the domain, as reproduced in figure 2.9, is done considering a conformal mesh for both domains (concrete and steel bar). Moreover, Konig and Kutzing (1999) use pullout tests to characterize fibers behavior keeping conformal the concrete and fiber meshes, similar as presented by Schumacher (2006).

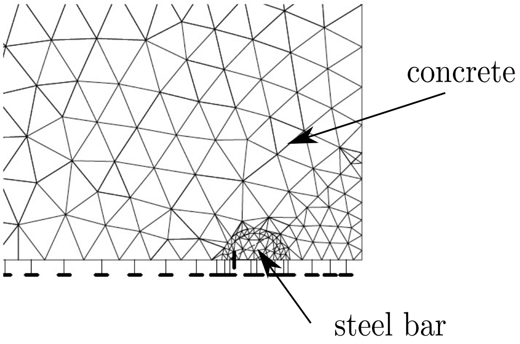

Figure 2.9: Mesh corresponding to the steel bar and the concrete concrete domain (from Schumacher (2006)).

Another approach is based on a numerical model for reinforced concrete, presented by Oliver et al. (2008), in which concrete is modeled considering a cohesive model based on a Continuum Strong Discontinuity Approach (CSDA). Moreover, fibers are defined with an elasto-plastic model and the interface is modeled using contact-friction elements. CSDA consists of a strong discontinuity kinematics projecting the continuous model (accounting for the constitutive equation of the material) onto the interfaces as a traction separation law.

The CSDA is applied to reinforced concrete considering the steel bars modeled with a different material than the concrete, reflecting the interfacial interaction between concrete and bars (bondslip and dowel action). In a mesoscopic scale, homogeneous elements are considered for the concrete and the reinforcement is discretized with appropriate interface elements between them to account for the concrete-reinforcement interaction. However, this mesoscopic approach needs large computational capacity. On the contrary, a macroscopic scale treatment allows considering the rebars embedded into the solid finite elements and discretizing the domain with coarser meshes (lower computational cost). Thus, Oliver et al. (2008) propose to model 2D reinforced concrete considering the CSDA with the mixture theory modeling the reinforced concrete. Figure 2.10 shows a mesh considered by Oliver et al. (2008) for applying their approach.

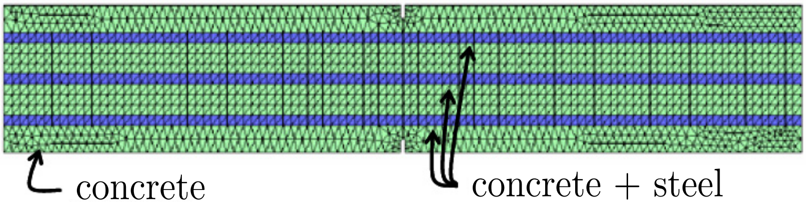

Figure 2.10: Domain considered by Oliver et al. (2008) for modeling reinforced concrete.

The CSDA can be applied also to SFRC. However, the CSDA idea brings to an homogenized model which do not allow to take into account the distribution of the fibers into the material.

Some analytical expressions providing constitutive equations for SFRC based on direct or inverse approaches giving macroscopic approximations are presented by Laranjeira (2010). In such constitutive models, SFRC is supposed to be an homogeneous material, useful for macromodeling the material behavior. However, the main drawbacks of this approach are that the homogenization process is not easy and the homogenized models do not account for the actual distribution of the fibers.

Most of the numerical methods proposed in the past have a common characteristic: concrete bulk and fiber cloud meshes are conformal (with geometrical matching), as observed in figures 2.9 and 2.10, corresponding to the approaches proposed by Schumacher (2006) and Oliver et al. (2008), respectively. Therefore, building up a conformal mesh for the whole system is cumbersome and computationally expensive. For pullout tests, considering only one fiber, conformal meshes are useful and relatively easy to generate. However, if several fibers are considered, these models are severely limited due to their computational cost.

There exist however previous attempts of using nonconformal meshes. These strategies were first introduced for standard reinforced concrete and, recently, also for SFRC.

For instance Phillips and Zienkiewicz (1976) and Balakrishnan and Murray (1986) introduce the idea of embedded reinforcement approach to deal with structures including curved walls with regular reinforcements. Phillips and Zienkiewicz (1976) consider the reinforcements to be discretized as one dimensional truss or beam elements. Moreover, perfect bond between steel and concrete is assumed. The finite element mesh layout is controlled by the reinforcements locations. Moreover, Phillips and Zienkiewicz (1976) and Elwi and Murray (1980) developed independent approaches for reinforced concrete performing the virtual work integration along the reinforcing layer and considering the reinforcement to be aligned with one of the local isoparametric element coordinate axes. Those approaches are useful for structures with curved walls with constant thickness and regular reinforcement.

A similar idea is presented by Elwi and Hrudey (1989) for concrete structures discretized with structured meshes and curved or draped reinforcements. In order to achieve the advantages of a regular mesh and, at the same time, be able to model complicated reinforcing details, an embedded representation of reinforcements is chosen. Curved reinforcements are difficult to discretize conformally to the concrete meshes, thus, concrete meshes are assumed to be regular and independent to the geometry of the reinforcements.

Referring to fiber reinforced concrete, Radtke et al. (2010b) introduce a nonconformal approach based on the partition-of-the-unity finite element method (PUFEMs). This strategy allows to avoid meshing the fibers. The displacement field $\mathbf{u}$ is considered discontinuous at the fiber boundary. Therefore, $\mathbf{u}$ is enhanced by a discontinuous enrichment, $\chi\widetilde{\mathbf{u}}$, where χ stands for an enrichment function which is discontinuous at the boundary of the fiber and constant otherwise. $\widehat{\mathbf{u}}$ is the regular part of the displacement field. Thus, $\mathbf{u} = \chi\widetilde{\mathbf{u}} + \widehat{\mathbf{u}}$, being $\widetilde{\mathbf{u}}$ and $\widehat{\mathbf{u}}$ continuous over the whole domain.

Apart form the strain tensor $\boldsymbol{\varepsilon}$, the displacement jump $[[\mathbf{u}]]$ over the fiber boundary is another quantity of interest. The constitutive behavior is composed by the relation of the bulk material and fiber behavior:

$$\boldsymbol{\sigma}_{\text{matrix}} = \mathbf{D}_{\text{matrix}} : \boldsymbol{\varepsilon} \tag{2.26}$$

$$\boldsymbol{\sigma}_{\text{fiber}} = \mathbf{D}_{\text{fiber}} : \boldsymbol{\varepsilon} \tag{2.27}$$

being $\mathbf{D}_{\text{matrix}}$ and $\mathbf{D}_{\text{fiber}}$ the fourth-order elastic material tensor of the matrix material and the fiber material, respectively.

Moreover, the constitutive relation for the fiber-matrix bond is defined as

$$\tau_{\text{fiber}} = \mathbf{D}_b[[\mathbf{u}]] \tag{2.28}$$

where $\mathbf{D}_{\text{b}}$ stands for the second-order elastic material tensor of the fiber-matrix bond.

The choice of the enrichment function is done depending on the thickness of the fiber. That is, if the fiber is assumed to be 2D or 3D, the enrichment function is defined as

$$\chi = \begin{cases} 1 \text{ inside of the fiber} \\ \\ 0 \text{ outside of the fiber} \end{cases} \tag{2.29}$$

However, assuming that the fiber is one dimensional, χ is defined as

$$\chi = \begin{cases} 1 \text{ in the boundary of the fiber} \\ \\ 0 \text{ in the rest of the domain} \end{cases} \tag{2.30}$$

Radtke et al. (2011) present the same ideas introduced by Radtke et al. (2010b), but considering a non-linear behavior of FRC. That is, instead of assuming a linear behavior for the concrete matrix (as Radtke et al. (2010b)), an isotropic damage model with exponential law is used. Thus, equation 2.26 turns to

$$\boldsymbol{\sigma}_{\text{matrix}} = (1 - w)\mathbf{D}^{e}_{\text{matrix}} : \boldsymbol{\varepsilon} \tag{2.31}$$

being w the damage variable and $\mathbf{D}^{e}_{\text{matrix}}$ the elastic material stiffness tensor.

Moreover, for avoiding mesh dependence, Radtke et al. (2011) regularize the model using an implicit gradient-enhanced damage model.

Radtke et al. (2010a) consider only a background mesh (corresponding to the concrete matrix) and the fibers (not discretized explicitly to ensure computational efficiency of the model) are represented by interaction forces. They consider the same isotropic damage model with exponential law (equation 2.31) for modeling the concrete matrix. On the contrary, fibers and fiber-matrix interfaces are represented by the reaction forces from the fibers to the matrix, which are represented by the fiber pullout forces:

$$\int_{\Omega^{+}_{fib}} \mathbf{p}^{+} d\Omega^{+}_{fib} = \mathbf{P}^{+} \tag{2.32}$$

being $\mathbf{p}^{+}$ the reaction forces from the fibers to the matrix along the fiber surface (Ω^{+}_{fib}) and $\mathbf{P}^{+}$ the force vector of the pullout.

The coupling between the fiber and the matrix models depends on the fiber pull-out distance, that is, the opening of the crack bridged by a fiber at the fiber crack intersection.

Chapter 3

Numerical modeling of plain concrete

3.1 Introduction

The main focus of this chapter is proposing numerical models for the Double Punch Test (DPT) in which the tensile strength (f_t) is an input parameter. The idea is to replace the naif linear elastic model by a more realistic one that has f_t already as one of material parameters and to identify the value of this material parameter that better fits the experimental results. These models are validated using experimental results and other analysis available in the open literature (Chen and Yuan (1980); Bortolotti (1988); Marti (1989); Molins et al. (2007)).

The information extracted from the experimental tests is translated into the parameters characterizing the mechanical properties of the analyzed concrete. In this case, the parameter to be assessed is precisely the tensile strength, f_t. Essentially, the data provided by the experimental setup is a force-displacement curve in which the peak points corresponding to the collapse are easily identified. The force corresponding to the peak point, P, is readily translated into the tensile strength value using a theoretical model simulating the mechanical behavior of the test, $f_t = \mathcal{F}(P)$. Currently, the underlying theoretical model used in this framework is an analytical solution of the linear elastic problem (Chau and Wei (2000a,b)). These models are a crude approximation of the actual behavior of the specimen close to the collapse regime but they still provide a good approach to the tensile strength by selecting a characteristic tensile stress in the linear elastic solution for the peak force, P.

Two different approaches are considered in order to model the mechanical behavior of the concrete in the DPT. Firstly (option A), a continuous model which has been successfully used modeling the common Brazilian test (Rodríguez-Ferran and Huerta (2000)), the nonlocal Mazars damage model (Mazars (1986); Bažant (2002); Jirásek (1998); Pijaudier-Cabot and Huerta (1991); Rodríguez-Ferran and Huerta (2000)). Secondly (option B), a model which introduces discontinuous fracture at the surfaces corresponding to an *a priori* defined cracking pattern, based on the experimentally observed fracture mechanisms (Díez and Pegon (2002); Beer (1985); Snyman et al. (1991)). On the fracture surfaces, joint elements with cohesive dilatant behavior are used to model the interfaces. In the rest of the specimen, the mechanical behavior is assumed to be linear elastic because the relevant deformation is concentrated in the fracture surfaces. Here, 3D finite element approximations are used complemented (for option B) with 2D joint elements. Both options A and B are solved using 3D finite elements.

Both options A and B provide approximations of the pre-peak and the post-peak behavior. Therefore, the information that may be extracted from the numerical tests is very rich and, in addition, to identify the parameters it may allow gaining further knowledge on the phenomenon.

The goal of this chapter is to analyze the features of the different models and their capabilities to properly approximate the experimental tests by fitting the experimental data available. An objective comparison is performed by setting a measure of the error between the experimental data and the model, this is equivalent to define a fitting criterion. Correspondingly, the parameter identification and the model validation are carried out both based on the same criterion.

All the experimental results are from an experimental campaign which consisted of the characterization of an specific concrete, including the double punch test. Hence, experimental data is available not only from the double punch test, but also from two different tests.

Thus, sophisticated models are used to identify the tensile strength from the DPT, instead of the linear elastic model. The advantage of using this approach is more relevant when DPT is used to identify the tensile behavior of steel fiber reinforced concrete. For fiber reinforced concrete (FRC), taking into account the post-peak behavior (and not only the peak) is extremely relevant. The present work has to be seen as a first step towards including steel fibers into these models in order to simulate the extension by of the DPT to assess the after cracking capacity of FRC (a test introduced in Molins et al. (2007, 2009), named as the *Barcelona Test*).

The remainder of this chapter is structured as follows. First, in section 3.2 the double punch test is presented, the problem statement is defined and the analytical expressions relating the tensile strength and the value of the maximum vertical load ($f_t = \mathcal{F}(P)$) are introduced, as well as the experimental campaign. Section 3.3 presents the numerical simulation: the continuous model and the discontinuous one. Then, in section 3.4, the numerical results are presented and contrasted. Moreover, the numerical results are validated with the experimental and analytical results available. Finally, the most important conclusions are listed.

3.2 Double Punch test

3.2.1 Description of the Double Punch Test

Double punch test was introduced by Chen (1970); Chen and Yuan (1980); Chen and Tumbauer (1972) as a tool to assess indirectly the tensile strength of plain concrete. It was presented as an alternative to the Brazilian test, which was so far the most common indirect tension test.

The test layout is illustrated in figure 3.1 and consists in compressing axially a cylindrical concrete specimen with two steel circular punches centered at the top and the bottom of the specimen. The geometry of the specimen is given by the height (l = 15cm) and the diameter (d = 15cm). The ratio between the diameters of the punches and the specimen is one fourth ($d' = \frac{1}{4}d = 3.75$cm).

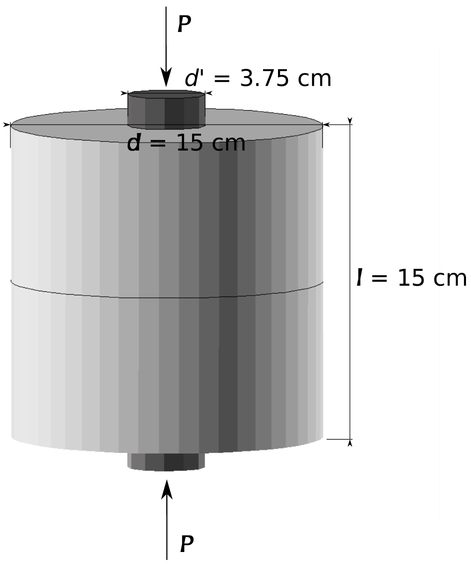

Figure 3.1: Double Punch Test layout

A typical failure mechanism presents three radial fracture planes. However, in the experimental results, the observed number of fracture planes ranges from two to four. The geometry of the collapse pattern is completed with two fracture cones beneath each punch. In figure 3.2 two different fracture patterns are illustrated.

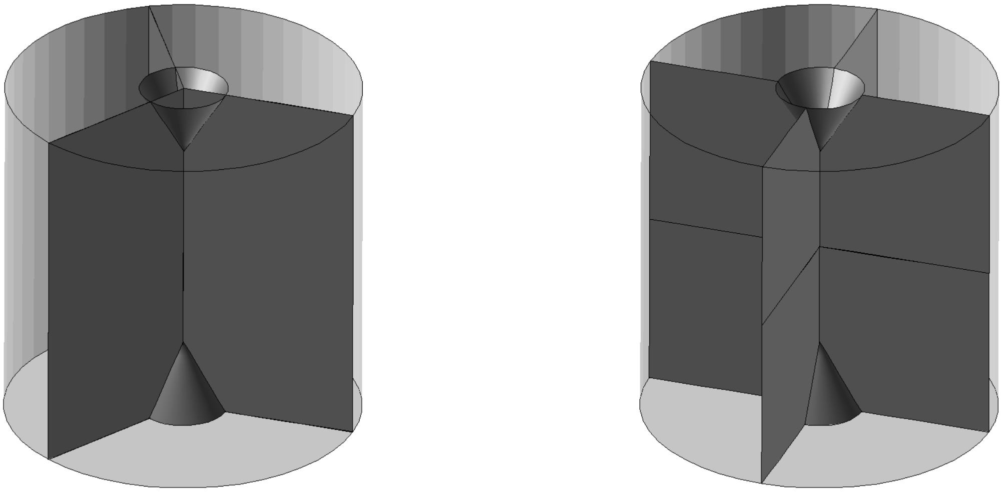

Figure 3.2: Two possible collapse mechanisms with three and four radial fracture planes

The goal of the present simulations is to describe the collapse of the specimen, with special interest in determining the peak load. Describing the chronological sequence of the cracks appearance, as discussed by Lilliu and Mier (2003, 1999), is beyond the scope of this thesis. In the models used here the fracture pattern is such that the specimen is partitioned into blocks that behave as rigid- bodies. Thus, the kinematics compatibility of the motion of these blocks undergoes a simultaneous development of the two basic mechanisms, namely the cone penetration and the separation of the crack planes.

The classical indirect tension test for plain concrete is the Brazilian test. DPT is often preferred to the Brazilian test because it is easier to carry out and the tensile strength is sampled in different cracked planes and, therefore, the quantity obtained corresponds to an average. On the contrary, the Brazilian test confines failure to a predetermined plane. Moreover, for Steel Fiber Reinforced concrete DPT captures better fibers influence than Brazilian test, due to their fracture mechanisms.

The experimental set up is a displacement controlled compression at a velocity of 0.5mm/min.

3.2.2 Close-form expressions for tensile strength determination

Some analytical expressions of the tensile strength are available in the literature for the DPT. The maximum compression load (P) and the dimensions of the test (d, d' and l) are the inputs in each analytical expression.

Chen and Yuan (1980) applied a limit analysis idealizing concrete as a linear elastic-perfectly plastic material with very large ductility obtaining

$$f_t = \frac{P}{\pi(1.2\frac{d}{2}l - (\frac{d'}{2})^2)}. \tag{3.1}$$

Moreover, in order to be more accurate, they carried out a finite element analysis considering concrete as an elastic plastic strain-hardening and fracture material and the final expression proposed is

$$f_t = \frac{0.75P}{\pi(1.2\frac{d}{2}l - (\frac{d'}{2})^2)}. \tag{3.2}$$

However, there are other analytical approximations of the tensile strength in the DPT given by different authors as follows.

Based on a nonlinear fracture mechanics approach, Marti (1989) proposed

$$f_t = 0.4\frac{P}{4(\frac{d}{2})^2}\sqrt{1 + \frac{d}{\lambda d_a}} \tag{3.3}$$

where d_a is the maximum aggregate size and λ is an experimental parameter depending on the material. This expression is given in order to analyze the size effect of the specimen on the tensile strength value.

Bortolotti (1988) assumed a modified Coulomb-like failure criterion for concrete getting

$$f_t = \frac{P}{\pi(\frac{d}{2}l - (\frac{d'}{2})^2 \cot\alpha)} \tag{3.4}$$

considering $\alpha = \frac{\pi}{2} - \frac{\phi}{2}$ with ϕ being the internal friction angle in the modified Coulomb's yield criterion.

Finally, Molins et al. (2007) presented another analytical expression based on limit analysis,

$$f_t = \frac{P}{9\pi l\frac{d'}{2}}. \tag{3.5}$$

In the following, these expressions are used for comparision purposes and we restrict ourselves to the expressions given in equations (3.1), (3.2) and (3.5).

3.2.3 Experimental campaign

The DPT is contrasted with two standard tests (the uniaxial compression test and the Brazilian test). The set up of these two tests is recalled bellow.

Uniaxial compression test

The uniaxial compression test, presented in figure 3.3, consists in a concrete cylinder subjected to compression. The load is applied in the whole surface of the top and the bottom of the specimen. The size of the specimen is set: $l = 30$ cm and $d = 15$ cm.

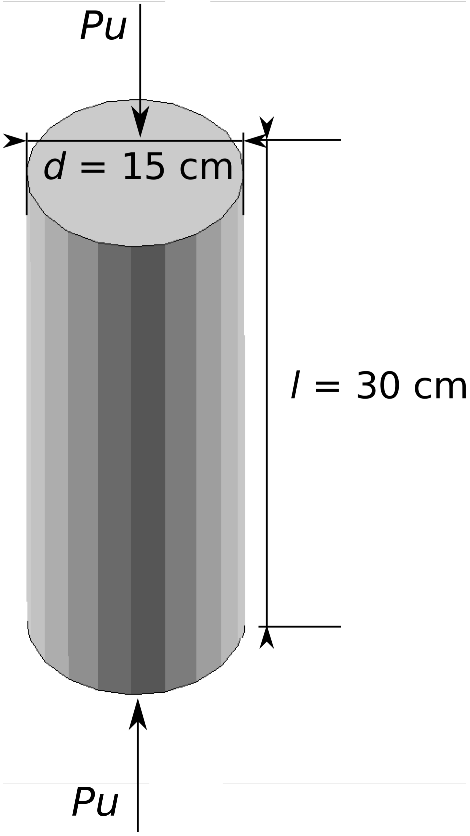

Figure 3.3: Description of the uniaxial compression test

This is a direct compression test which provides the compressive strength, f_c. The relationship between the compressive strength f_c and the maximum vertical load P_u is given by

$$f_c = \frac{4P_u}{\pi d^2} \tag{3.6}$$

where d stands for the diameter of the specimen.

Experimentally, the value obtained is $P_u = 8.9 \cdot 10^5$N, which is translated into f_c through equation (3.6): $f_c = 50.45$MPa.

Brazilian Test

On the other hand, the Brazilian test is an indirect tension test consisting in compressing a plain concrete cylinder placed horizontally by two steel plates (as shown in figure 3.4).

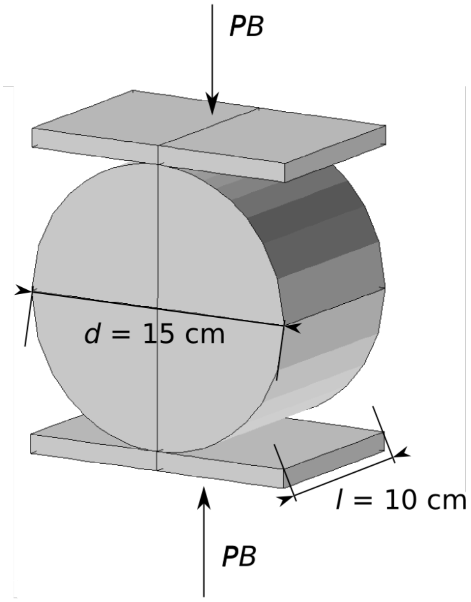

Figure 3.4: Description of the Brazilian test

For the Brazilian test, the relation between the tensile strength with the maximum vertical load is given by

$$f_t = \frac{2P_B}{\pi l d} \tag{3.7}$$

where l and d stand for the length and the diameter of the concrete specimen, respectively.

The given analytic expression is standard and there is agreement about its accuracy.

Experimentally, the average value obtained is $P_B = 8.6 \cdot 10^5$N, which is translated to the tensile strength, f_t, using the equation (3.7). Thus, the value of the tensile strength is set: $f_t = 3.84$MPa.

Experimental results

The data presented in table 3.1 is the result of an experimental campaign carried out in the *Departament d'Enginyeria de la Construcció* of the *Universitat Politècnica de Catalunya (UPC)*. The uniaxial compression test, the Brazilian test and the DPT are considered. The mean values are displayed and, in brackets, the coefficient of variation (standard deviation divided by the mean value) is presented. The Poisson ratio (ν) is assumed to be equal to 0.2.

Table 3.1: Experimental data

Description	Symbol	Value
Young's modulus	E	35.5GPa
Compressive strength (from the uniaxial compression test)	f_c	50.45MPa (2.69%)
Tensile strength (from the Brazilian test)	f_t	3.84MPa (8.36%)
Maximum load (from the DPT)	P	$1.52 \cdot 10^5$N (4.10%)

The DPT campaign consists in six test, three of them showed three fracture radial planes and the other three showed four fracture radial planes.

In this case, the uniaxial compression test (giving f_c), the Brazilian test (giving f_t as far as the Brazilian test is considered to be reliable) and the output of the DPT (the maximum vertical load P) are available for the same material. Numerical models are needed to find the expected value P of the DPT for a given f_t. Although analytically some expressions relating f_t and P for the DPT are available, they present scattering.

The relation $f_t = \mathcal{F}_B(P_B)$ for the Brazilian test is reliable, therefore, the numerical models are validated firstly for this test.

3.3 Numerical modeling

Two different techniques are considered to simulate numerically the double punch test. On one hand, a continuous model, the nonlocal Mazars damage model (based on Mazars (1986) and Bažant (2002)), which has already been used in previous simulations of indirect tension tests (Rodríguez-Ferran and Huerta (2000)). On the other hand, a discontinuous model is considered based on introducing joint elements along the cracks. This model defines *a priori* the cracking pattern (known through the experimental tests and the analytical description of the DPT). Then, joint elements are used to model the cracks. The rest of the specimen is modeled as an elastic material.

The behavior of the DPT is a fully 3D phenomenon and, therefore, 3D modeling is required for both cases.

3.3.1 Nonlocal Mazars damage model

In the nonlocal Mazars damage model (presented in section 2.3.1), the parameters A_t, B_t, A_c, B_c and the threshold Y_0 are set depending on the material modeled, taking into account the relationship between damage parameters and experimental parameters.

The constitutive equation under tension for a uniaxial test can be written as

$$\sigma = \begin{cases} E \cdot \varepsilon, & \varepsilon \leq Y_0 \\ \\ \left[\dfrac{Y_0(1 - A_t)}{\varepsilon} + A_t \cdot e^{-B_t(\varepsilon - Y_0)} \right] \cdot E \cdot \varepsilon, & \varepsilon > Y_0 \end{cases} \tag{3.8}$$

and the constitutive equation under compression is deduced for a uniaxial test

$$\sigma = \begin{cases} E \cdot \varepsilon, & \varepsilon \leq Y_0 \\ \\ \left[\dfrac{Y_0(1-A_c)}{\varepsilon} + A_c \cdot e^{-B_c(\varepsilon - Y_0)}\right] \cdot E \cdot \varepsilon, & \varepsilon > Y_0 \end{cases} \tag{3.9}$$

Now, the damage parameters deduction is presented based on (3.8) and (3.9).

- Imposing that *if* $\varepsilon = Y_0 \quad \Rightarrow \quad \sigma = f_t$ in (3.8), it results

$$Y_0 = \frac{f_t}{E} \tag{3.10}$$

- Under tension, $\lim_{\varepsilon \to \infty} \sigma = \sigma_\infty$, with σ_∞ standing for the residual tensile strength, is considered. Therefore, using (3.8),

$$E \cdot Y_0 \cdot (1 - A_t) = \sigma_\infty \quad \Rightarrow \quad A_t = 1 - \frac{\sigma_\infty}{E \cdot Y_0} \tag{3.11}$$

- $B_t = 10000 \cdot (1 + \xi)$, where ξ is a parameter measuring the material ductility.
- Under compression, $\sigma'(\varepsilon_{max}) = 0$. Let us derivate (3.9), getting

$$B_c = \frac{1}{\varepsilon_{max}} \tag{3.12}$$

- Imposing $\sigma(\varepsilon_{max}) = f_c$ under compression in (3.9) and using $B_c = \dfrac{1}{\varepsilon_{max}}$, A_c is obtained:

$$A_c = \frac{f_c - E \cdot Y_0}{-E \cdot Y_0 + E \cdot \varepsilon_{max} \cdot e^{\left(-1 + \frac{Y_0}{\varepsilon_{max}}\right)}} \tag{3.13}$$

- To ensure, under compression, that $0 \leq D \leq 1$ it is necessary to impose that

$$0 \leq A_c \leq 1 \tag{3.14}$$

In figure 3.5, the plain concrete damage model is presented in two graphics, one corresponding to the tension behavior (3.5(a)) and another to compression (3.5(b)).

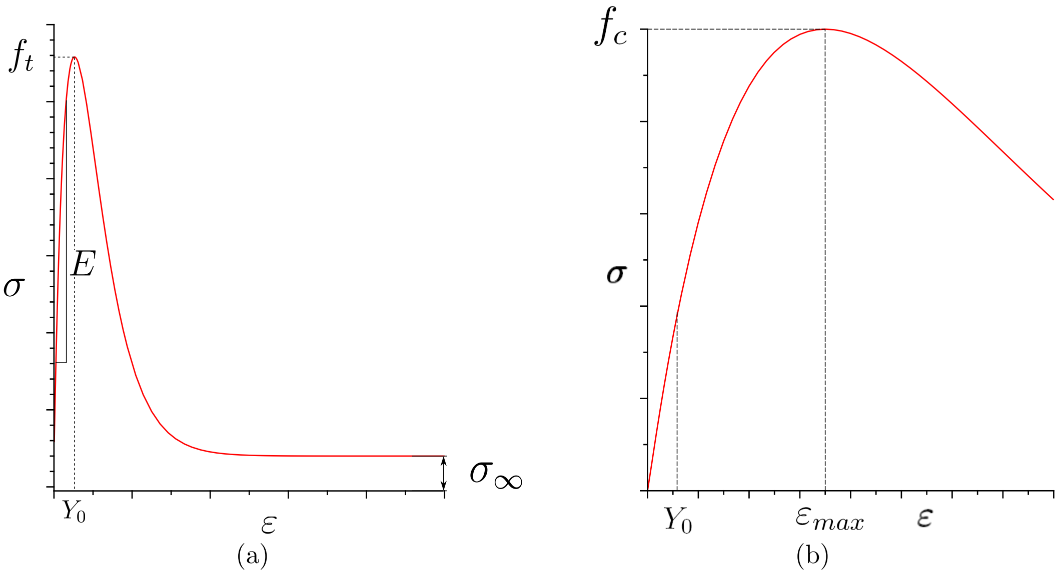

Figure 3.5: Uniaxial test. (a) Tension. (b) Compression.

Moreover, the characteristic length (l_{car}) is another material parameter to be set for regularizing the model.

3.3.2 Heuristic crack model with joints

An alternative to the damage model is a discontinuous model which considers the whole specimen as an elastic material and the cracking pattern defined using joint elements, presented in section 2.3.3.

The parameter deduction of the joint model is presented as follows: The first normal stiffness (N/m^3) is defined as $k_{n1} = \dfrac{E}{l}$, where l stands for the specimen height, as well as the shear stiffness, (N/m^3), $k_s = \dfrac{E}{l}$. Otherwise, the second normal stiffness (N/m^3) must satisfy that $k_{n2} \leq 0$, because the negative branch is a modeling artifact to account for the sudden loss of strenght associated with cracking, while preserving the mathematical regularity of the model. The threshold from k_{n1} to k_{n2}

is defined as $u_0 = \frac{f_t}{k_{n1}}$ and the cohesion (N/m^2) is $c = f_c$. Finally, the friction angle is fixed as $\varphi = 54°$, as found in the literature (Bortolotti (1988)).

3.4 Numerical results and validation

All the results obtained considering both the continuous and the discontinuous model are presented. Both the Brazilian test and the double punch test are simulated. Moreover, the results are validated and compared with the analytical expressions and with the experimental data.

3.4.1 Nonlocal Mazars damage model

For simulating numerically considering the nonlocal Mazars damage model, six material parameters must be set: damage threshold (Y_0), characteristic length (l_{car}), tension parameters (A_t and B_t) and compression parameters (A_c and B_c).

From the experimental campaign, the value of the compressive strength obtained through the uniaxial compression test is available, $f_c = 50.45$MPa. Therefore, through the uniaxial compression test, any parameter may be evaluated, but the relation between the two compression parameters is set. Hence, when A_c and B_c satisfy the given equation (3.13), the value of the compressive strength is set (f_c).

The value given by the experimental campaign from the Brazilian test is the tensile strength, $f_t = 3.84$MPa. Therefore, through the equation (3.10), the value of Y_0 is set.

Hence, herein, some consideration must be taken into account:

- $Y_0 = \frac{f_t}{E} = \frac{3.84 \cdot 10^6}{35.5 \cdot 10^9} = 1.08 \cdot 10^{-4}$
- Considering any value of A_c satisfying $0 \leq A_c \leq 1$ is enough to ensure that $0 \leq D \leq 1$ and the chosen value does not influence on the results, therefore, $A_c = 1$.

- the relationship obtained from the uniaxial compression test between A_c and B_c must be satisfied (equation (3.13)), considering $f_c = 50.45\text{MPa}$. Thus, $B_c = 266$.
- $A_t = 1 - \frac{\sigma_\infty}{E} = 1$, because the residual strength under tension is $\sigma_\infty = 0$ for plain concrete
- $B_t = 10000 \cdot (1 + \zeta)$, with $0 < \zeta < 1$, depending on the material. Hence, $B_t = 2500$.
- Observing the specimen size of the test and the expected fracture pattern, the caracteristic length (l_{car}) is set.

Brazilian test

Considering the previous information for simulating numerically the Brazilian test, the value of the tensile strength can be obtained (calculated through the value of the maximum vertical load, considering the equation (3.7)). All the material parameters are set previously, except l_{car} which is set observing the expected fracture pattern of the test and its sizes. Hence, the optimal material parameters are presented in table 3.2.

Table 3.2: Optimal values of the material parameters of the nonlocal Mazars damage model for the Brazilian test

Material parameter	Value
Y_0	$1.08 \cdot 10^{-4}$
l_{car}	$2 \cdot 10^{-2}\text{m}$
A_t	1
B_t	2500
A_c	1
B_c	266

Vertical displacements are prescribed at the top of the specimen through one steel plate, which is modeled as an elastic material. Moreover, both horizontal and vertical symmetric conditions are imposed, thus, only a quarter of the specimen is taken into account during the whole simulation.

After the simulation, in figure 3.6, the value of the maximum vertical load depending on the vertical displacement is presented and, as expected, the maximum value is $P_B = 8.8 \cdot 10^5$N, which corresponds to $f_t = 3.74$MPa (considering the equation (3.7)).

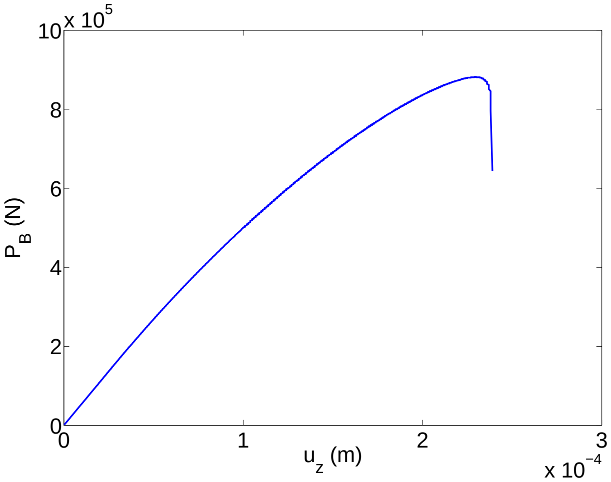

Figure 3.6: Brazilian test with the nonlocal Mazars damage model. u_z(m) - P_B(N).

In order to analyze the fracture pattern of the Brazilian test, the damage distribution obtained numerically is presented in figure 3.7.

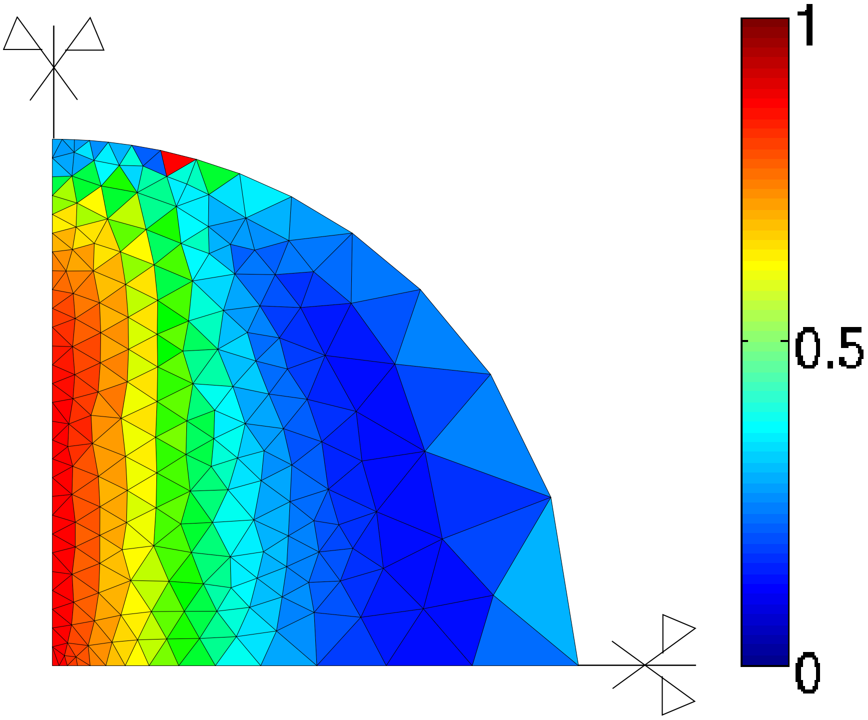

Figure 3.7: Damage distribution at the load peak

Double Punch Test

In this case, again, taking into account all the experimental information there is only one degree of freedom when setting the material parameters, l_{car}, which depends on the test size and the fracture pattern. l_{car} is set to adjust the numeric results with the experimental ones. Hence, the same parameter combination suitable for the Brazilian test is chosen, but with a different value of the characteristic length (as presented in table 3.3).

Table 3.3: Optimal values of the material parameters of the nonlocal Mazars damage model for the double punch test

Material parameter	Value
Y_0	$1.08 \cdot 10^{-4}$
l_{car}	$2.5 \cdot 10^{-3}$m
A_t	1
B_t	2500
A_c	1
B_c	266

Displacements are imposed at the top punch which are modeled as an elastic material. Symmetric conditions are imposed in order to work with half of the problem.

The vertical load versus the maximum vertical displacement is presented in figure 3.8. It is possible to observe that the maximum value ($1.92 \cdot 10^5$N) is close to the one obtained experimentally ($1.52 \cdot 10^5$N) and the vertical displacement value ($2.55 \cdot 10^{-4}$m) also is next to the experimental one. In addition, after the peak, it is possible to capture the behavior.

Figure 3.9 shows different views of the specimen with the damage distribution to be able to observe the whole cracking pattern. Looking at the damage distribution, four radial vertical cracking planes are observed (figures 3.9(a) and 3.9(b)). Moreover, the cone formation under the punch is presented, as expected, in the inside view of the specimen (figure 3.9(c)). Although the cracking pattern is detected, it is not possible to capture the whole pattern.

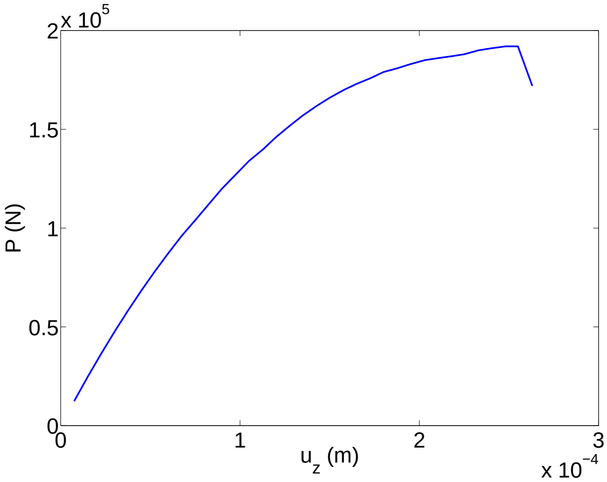

Figure 3.8: Double punch test with the nonlocal Mazars damage model. u_z(m) - P(N).

Although different meshes (for the same geometry) have been used with the numerical simulation of the double punch test considering the nonlocal Mazars damage model, the fracture pattern is always the same, as expected, and placed as observed in figure 3.9, as well as the value of the maximum vertical load.

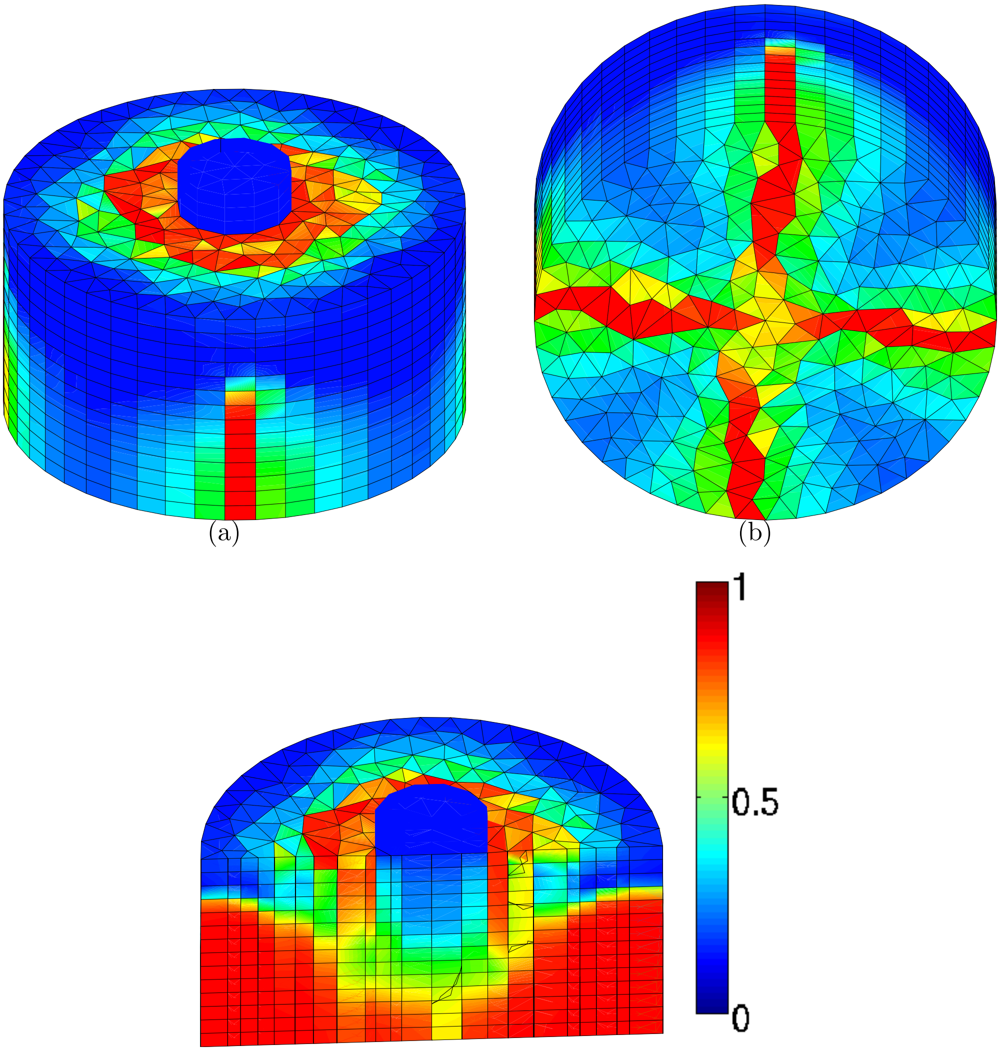

(a) (b)

(c)

Figure 3.9: Damage distribution at the end of the simulation. (a) Top view. (b) Bottom view. (c) Inside view.

3.4.2 Heuristic model with joint elements in the cracking pattern

Brazilian test

Observing the damage distribution (figure 3.7), the Brazilian test is simulated modeling the cracking pattern with joint elements, meanwhile the rest of the specimen is considered elastic. In figure 3.10, joint elements are in red, meanwhile, the linear ones are in blue.

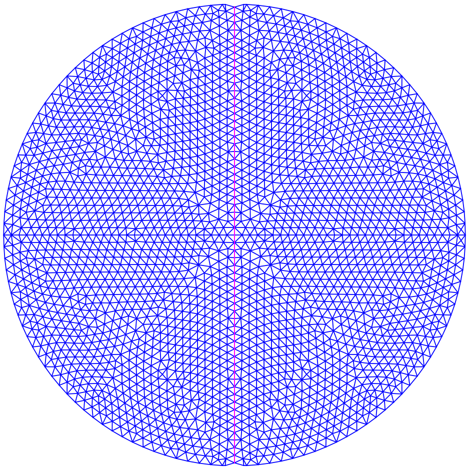

Figure 3.10: Brazilian test mesh for the discontinuous model

All the material parameters of the joint elements for the Brazilian test are set based on the experimental data ($f_t = 3.84$MPa and $f_c = 50.45$MPa) and the specimen height ($l = 0.1$m), as presented in table 3.4.

Vertical displacements are prescribed at the top and bottom sheets, modeled under an elastic model, and the whole specimen is taken into account.

Figure 3.11 presents the maximum vertical load (P_B) depending on the vertical displacement (u_z) and the maximum value of P_B is $P_B = 8.8 \cdot 10^5$N, which corresponds to $f_t = 3.72$MPa, considering the equation 3.7.

Table 3.4: Values of parameters for the Brazilian test

Symbol	Value
k_{n1}	$\dfrac{35.5 \cdot 10^9}{0.1}\mathrm{N/m^3}$
k_{n2}	$\dfrac{-35.5 \cdot 10^9}{0.1}\mathrm{N/m^3}$
u_0	$\dfrac{3.84 \cdot 10^6}{35.5 \cdot 10^9}\mathrm{m}$
k_s	$\dfrac{35.5 \cdot 10^9}{0.1}\mathrm{N/m^3}$
f_t	3.84MPa
c	50.45MPa
φ	54^o

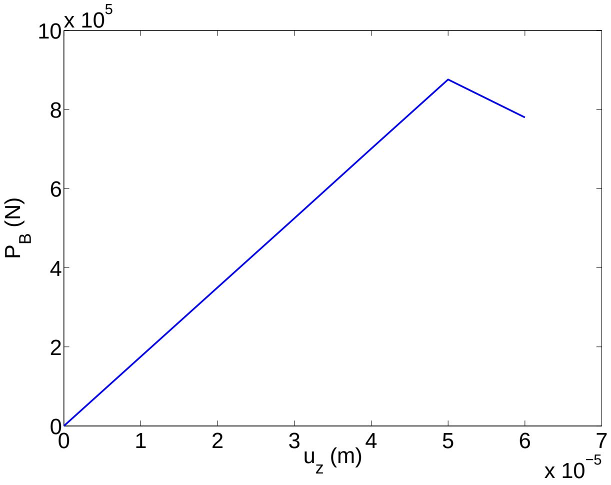

Figure 3.11: Brazilian test with the joint model. u_z(m) - P_B(N).

Double punch test

In order to simulate the double punch test considering the heuristic crack model with joint elements defined here, two different meshes are considered (as presented in figure 3.12): one with three radial planes and another with four radial planes.

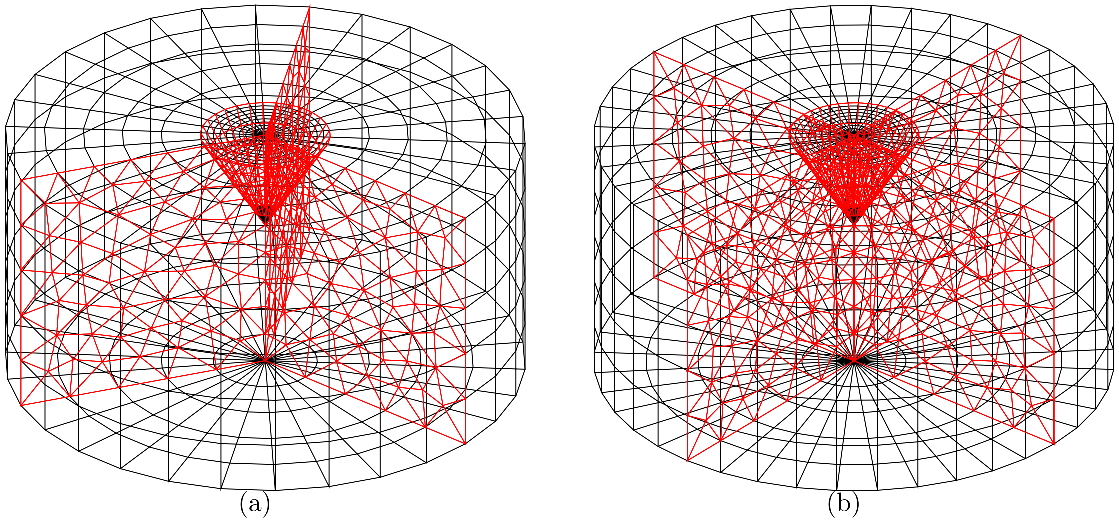

Figure 3.12: Double punch test including joint elements meshes. (a) three radial cracking planes. (b) four radial cracking planes.

Although double punch test is modeled in 3D, all joint elements are two-dimensional and triangular for the fracture planes and quadrilateral for the cone. The tip of the cone is not included in the mesh because it would be a point defined too many times. Besides, three auxiliary planes are defined corresponding to the specimen's cracking planes, but inside the cone. They are necessary to define properly the joint elements. For the case of four radial planes, also four auxiliary planes are defined inside the cone (corresponding to the intersection between the cone and the two diametral planes).

Firstly, three fracture radial planes are considered. All the material parameters are set using the experimental data and they are the same than for the Brazilian test, except the specimen height (herein, $l = 0.075$m) as presented in table 3.5. Moreover, the material parameters in the auxiliar joint elements inside the cone are defined in order to not influence on the results.

Table 3.5: Values of parameters for the Double Punch Test

Symbol	Value
k_{n1}	$\dfrac{35.5 \cdot 10^9}{0.075}\mathrm{N/m^3}$
k_{n2}	$\dfrac{-35.5 \cdot 10^9}{0.075}\mathrm{N/m^3}$
u_0	$\dfrac{3.84 \cdot 10^6}{35.5 \cdot 10^9}\mathrm{m}$
k_s	$\dfrac{35.5 \cdot 10^9}{0.075}\mathrm{N/m^3}$
f_t	3.84MPa
c	50.45MPa
φ	54^o

Vertical displacements are imposed at the top punch which is modeled as an elastic material. Horizontal symmetric condition is taken into account, thus, only half of the specimen is considered in the current simulation.

In figure 3.13, the maximum vertical load obtained is presented versus vertical displacement. As observed, it is possible to capture the behavior after reaching the peak load. The maximum vertical load ($1.55 \cdot 10^5$N) is in the same rang of values than the load obtained experimentally ($1.52 \cdot 10^5$N). Moreover, the value of the vertical displacements corresponding to the peak load ($5.25 \cdot 10^{-4}$m) is also close to the corresponding experimental value.

It is also observed that both the horizontal displacement (Δh) and the vertical displacement (Δv), corresponding to the peak load, keep the same ratio than the relation between the two cathetus of the cone's generator triangle. That is, if the horizontal cathetus measures $c_h = 1.875$ cm and the vertical one, $c_v = 3$ cm, $\dfrac{c_h}{\Delta h} = \dfrac{c_v}{\Delta v}$ is satisfied.

Figure 3.14 represents the deformed mesh after the simulation from different points of views. The cone is penetrating the specimen, meanwhile the three cracking planes are opening in their normal directions.

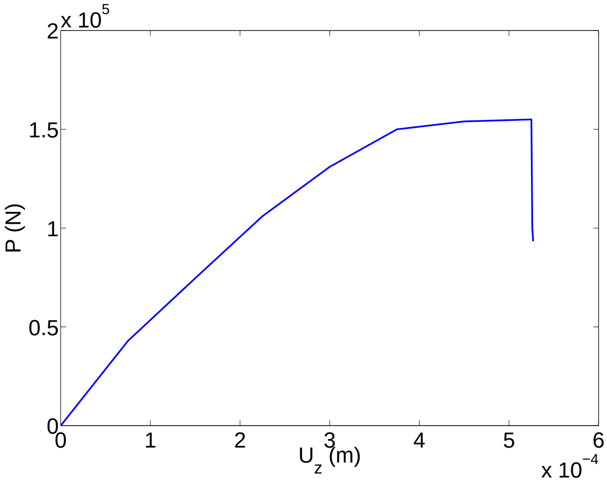

Figure 3.13: Double punch test modeled using joint elements considering three cracking planes. u_z(m) - P(N).

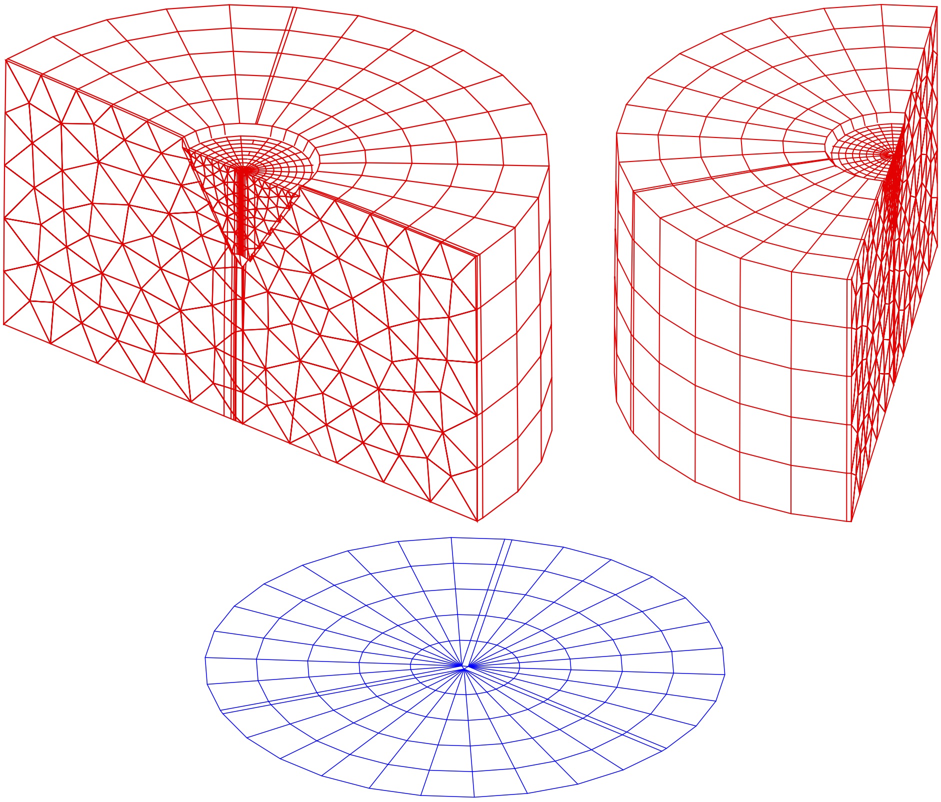

Figure 3.14: Double punch test modeled using joint elements considering three cracking planes. Deformed meshes amplified ×10.

Once the results considering three cracking planes defined *a priori* are analyzed, four radial cracking planes are considered with the same material parameters (presented in table 3.5) than in the previous case. However, herein, the fracture pattern is different, so the same value of the maximum vertical load under the same conditions is not expected.

In figure 3.15 the results are presented and it is observed that the behavior is the same both with three and four radial cracking planes. Moreover, after the load peak, it is possible to obtain further results. Besides, the maximum vertical load ($1.56 \cdot 10^5$N) is still the same as the experimental value, and very close to the value obtained with three cracking planes. The value of the vertical displacement ($5.25 \cdot 10^{-4}$m) is also in the expected range of values.

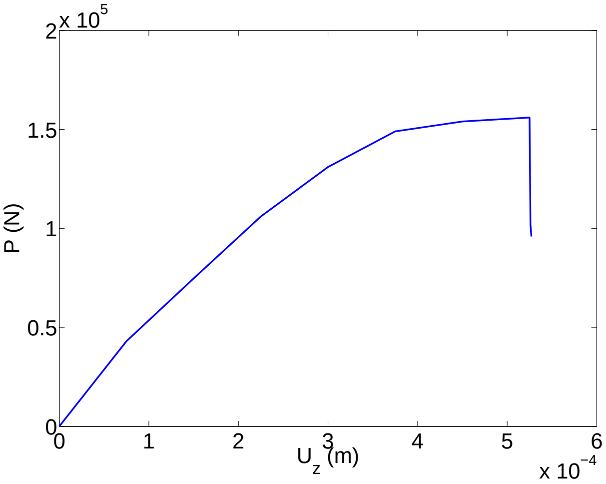

Figure 3.15: Double punch test modeled using joint elements considering four radial cracking planes. u_z(m) - P(N).

Once all the material parameters are set (for both cases, three and four radial fracture planes), a geometric parameter is studied: the cone's height. When defining *a priori* the fracture pattern, cone's height is an input. After considering different values of the cone height, it has been found that the value providing results in agreement with the experimental outcome is $h = 3$cm. Note that this is also coinciding with the cone height observed in experiments.

3.4.3 Validation

Considering $f_c = 50.45$MPa and $f_t = 3.84$MPa set, in table 3.6 all the numerical results are presented and compared both with analytical expressions and experimental results.

- Analytical expressions:
  - $P_1 = f_t\pi(1.2l\frac{d}{2} - (\frac{d'}{2})^2)$, from Chen and Yuan (1980).
  - $P_2 = \frac{f_t\pi(1.2l\frac{d}{2} - (\frac{d'}{2})^2)}{0.75}$, from Chen and Yuan (1980).
  - $P_3 = f_t 9\pi l\frac{d'}{2}$, from Molins et al. (2007).
- Experimental value: $P_{exp} = 1.52 \cdot 10^5$N

These values are compared to the numerical results considering the continuous model, P_{cont}, and the discontinuous one with three fracture radial planes, P_{disc3}, and four fracture radial planes, P_{disc4}.

The errors are computed considering $\text{Error}(P_i) = |\frac{P_i - P_j}{Pi}| \cdot 100\%$, being P_i the maximum vertical load obtained analytically or experimentally, and P_j the rest of the values.

Table 3.6: Model Validation

Description	P(N)	Error(P_1)	Error(P_2)	Error(P_3)	Error(P_{exp})
P_1	$1.51 \cdot 10^5$	0%	24.4%	4.1%	0.6%
P_2	$2.01 \cdot 10^5$	33.11%	0%	38.6%	32.2%
P_3	$1.45 \cdot 10^5$	3.4%	27.8%	0%	5%
P_{exp}	$1.52 \cdot 10^5$	0.6%	24.4%	5%	0%
P_{cont}	$1.92 \cdot 10^5$	27%	4.5%	32%	26.3%
P_{disc3}	$1.55 \cdot 10^5$	2.7%	22.9%	6.9%	2%
P_{disc4}	$1.56 \cdot 10^5$	3.3%	22.4%	7.6%	2.6%

3.5 Concluding remarks

To sum up, all the important conclusions of this chapter are presented in the following.

The double punch test has been simulated using two different techniques: (a) the nonlocal Mazars damage model and (b) an elastic model considering the cracking pattern modeled with joint elements. In both cases, results are as expected, very close to the experimental and analytical ones (i.e. in the same range of values, as shown in table 3.6). These two numerical models are validated through the Brazilian test, taking into account the experimental information from the uniaxial compression test, the Brazilian test and the double punch test.

All the parameters (both the material and the geometrical ones) are set for both numerical models for each test. However, it is not proved that these material parameter combinations are unique. Experimental results are necessary to set all the parameters and, in general, the definition of the test.

After trying different material combinations for the nonlocal Mazars damage model, always taking into account all the conditions found during the present work, the optimal parameter combination is found. In this case, the only different parameter for the two different indirect tension tests (the Brazilian test and the double punch test) with the same concrete is the characteristic length which depends on the fracture pattern and the test size.

For the joint model, it is again observed that with a different fracture pattern (three or four planes), the same material parameters is used. Likewise, for the Brazilian test and the double punch test, except for the specimen height.

Compared with the available experimental results and some of the analytical expressions, the most suitable model is the discontinuous one considering both, three and four cracking radial planes because fits better the experimental results. However, using the joint model, it is necessary to know the fracture pattern before the simulation. Meanwhile, with the nonlocal Mazars damage model, the failure pattern is not set *a priori*. Moreover, the fracture pattern obtained considering the damage model fits with the experimental one and the obtained peak value corresponds to other analytical expressions.

Time calculation and computational cost are shorter using the discontinuous model than with the nonlocal Mazars damage model, due to the number of nonlinear elements in each model.

Both the nonlocal Mazars damage model and the model including joint elements in the cracking pattern are valid alternatives to simulate the double punch test, which was designed for studying the tensile strength (f_t) of concrete. Therefore, these numerical simulations allow to control f_t, for any material parameters considering both models. In both cases, f_t is an input of the problem and the maximum vertical load, P, is the output of the problem.

Having at hard these two alternatives allows reproducing numerically the behavior of the DPT described by different authors and also with experimental results available.

Up to now, the double punch test has been simulated numerically for plain concrete. Then the next step is including fibers into these models in order to simulate the double punch test for steel fiber reinforced concrete (a test introduced by Molins et al. (2007) and Molins et al. (2009), defined as the *Barcelona Test*).

Chapter 4

Numerical tool for modeling Steel Fiber Reinforced Concrete

4.1 Introduction

In this chapter, an alternative for modeling numerically SFRC is presented, based on the ideas introduced by Pros et al. (2008). The goal is to avoid conformal meshes and homogenized models. In the current proposal, concrete and fiber meshes are independent, nonconformal, and the actual geometry of all the fibers is defined inside the concrete mesh. Moreover, although concrete and fiber models interact, they are defined independently. The main idea considered herein for coupling the two models is based on the Immersed Boundary (IB) methods (Boffi and Gastaldi (2003); Boffi et al. (2007); Mittal and Iaccarino (2003)), which were introduced for a fluid with a solid immersed in it (here, concrete is thought as the fluid and the fibers are like the solid structure immersed in the fluid). Then, displacement compatibility between the two models is imposed. In order to describe the whole debonding process between the fibers and the plain concrete, a mesomodel for steel fibers is presented, which is translated into the constitutive equations for fibers. These constitutive equations depend on the angle between the fiber and the normal direction of the failure pattern. They also depend on the shape of the fiber (straight or hooked). The model for plain concrete is defined independently, being typically a nonlinear model.

The remainder of this chapter is structured as follows. First, in section 4.2, the problem statement of SFRC is presented. In section 4.3, the discrete approach of the problem is described. Section 4.4 presents the models considered for each material: (a) a nonlinear mesomodel for steel fibers accounting for the whole behavior between plain concrete and steel fibers and (b) nonlinear models for plain concrete. Then, in section 4.5, two numerical examples of the proposed model are presented: a pullout test (considering different fiber orientations) and the direct tension test considering both plain concrete and SFRC (with straight and hooked fibers). The chapter is closed with some concluding remarks and perspective future work.

4.2 Problem statement

The problem to be solved is stated as follows. An open bounded domain is considered $\Omega \subset \mathbb{R}^d$, with $d = 2$ or $d = 3$, as shown in figure 4.1, which is composed by two different subdomains: $\overline{\Omega} = \overline{\Omega_C \cup \Omega_S}$, being Ω_C and Ω_S the volumes occupied by the concrete and steel, respectively. Thus, the whole domain Ω represents the SFRC.

The boundary of the domain is divided into two parts referring to the boundary conditions: $\partial\Omega = \overline{\Gamma}_N \cup \overline{\Gamma}_D$, with $\Gamma_N \cap \Gamma_D = \emptyset$, being Γ_N and Γ_D associated with the Neumann and Dirichlet boundary conditions, respectively. Moreover, the internal boundary Γ_{int}, defining the interface between concrete and steel, is given by $\Gamma_{\text{int}} = \overline{\Omega_C} \cap \overline{\Omega_S}$.

The unknown function $\boldsymbol{u}$, taking values in Ω, is the displacement field fulfilling the following boundary value problem

$$-\nabla \cdot \boldsymbol{\sigma}(\boldsymbol{u}) = \boldsymbol{b}_C \qquad \text{in } \Omega_C \tag{4.1a}$$

$$-\nabla \cdot \boldsymbol{\sigma}(\boldsymbol{u}) = \boldsymbol{b}_S \qquad \text{in } \Omega_S \tag{4.1b}$$

$$\boldsymbol{u} = \boldsymbol{u_D} \qquad \text{on } \Gamma_D \tag{4.1c}$$

$$\boldsymbol{\sigma}(\boldsymbol{u}) \cdot \boldsymbol{n} = g_N \qquad \text{on } \Gamma_N \tag{4.1d}$$

$$\boldsymbol{\sigma}(\boldsymbol{u}) \cdot \boldsymbol{n}|_{\Omega_S} = \boldsymbol{\sigma}(\boldsymbol{u}) \cdot \boldsymbol{n}|_{\Omega_C} \qquad \text{on } \Gamma_{\text{int}} \tag{4.1e}$$

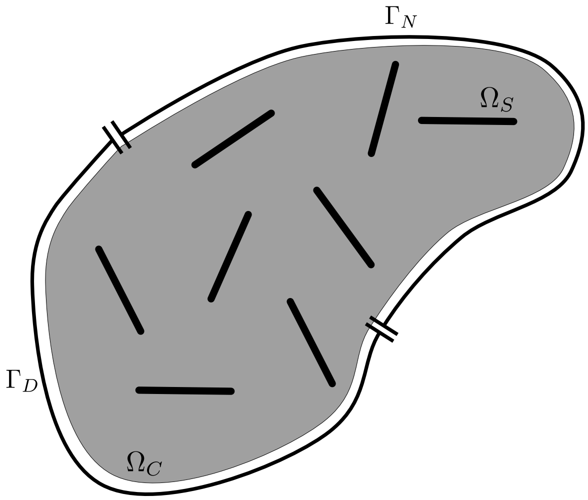

Figure 4.1: General domain

where $\boldsymbol{b}_C$ and $\boldsymbol{b}_S$ stand for the body loads in the concrete and steel and $\boldsymbol{u_D}$ and g_N are the prescribed displacements and tractions on Γ_D and Γ_N.

For solving the current problem, different options could be considered. As pointed out in the state of the art (chapter 2), one possibility is defining conformal meshes for the two domains Ω_C and Ω_S with different material models. Another option consists in considering an homogenized model for the complete domain. In this thesis, a third option is presented avoiding conformal meshes (too expensive and not affordable for large number of steel fibers) and homogenized models (not accounting for the actual geometry of the fibers).

The proposed approach is based on the Immersed Boundary (IB) methods (Boffi and Gastaldi (2003); Boffi et al. (2007); Mittal and Iaccarino (2003)) which were introduced for solving problems considering a solid structure immersed in a fluid. The main idea of these methods is to neglect the space occupied by the solid structure. The fluid is considered to occupy the whole domain and the velocities of both solid and fluid are made compatible in the coinciding points. Then, the effect of the solid in the fluid is accounted for by adding an interaction force. The two systems (fluid and solid structure) are considered separately and compatibility is enforced by adding the corresponding interaction forces. The discretization of the problem is therefore

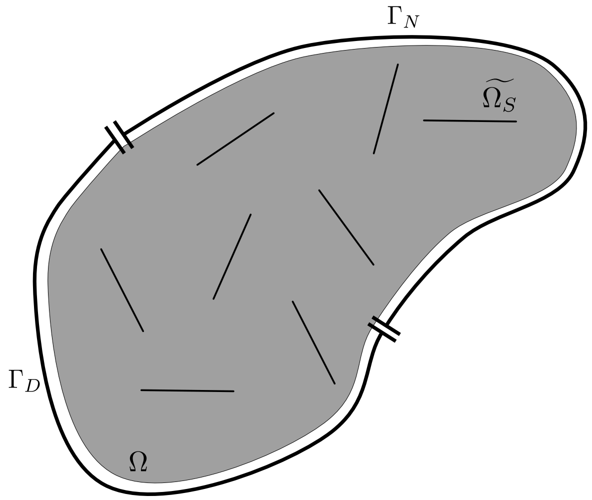

Figure 4.2: Ideal domain

simplified because the mesh of the whole domain (the fluid) may be very simple (eventually a cartesian mesh) and the mesh for the solid body does not require to be conformal with it. The models corresponding to the fluid and the solid are defined independently.

Here, the same approach is used, taking the plain concrete the role of the fluid, and the fiber cloud the role of the solid structure. Therefore, the problem to be solved is redefined. First, the geometrical conception is adapted to the new scheme. It is assumed that the geometrical support of the fibers is a 1D manifold (with measure zero in $\mathbb{R}^d$). Thus, Ω_S is replaced by an ideal version $\widetilde{\Omega_S}$, see figure 4.2. The two subdomains Ω_C and Ω_S are therefore replaced by Ω and $\widetilde{\Omega_S}$, respectively. Note that the fiber cloud domain, $\widetilde{\Omega_S}$, is defined overlapping the new concrete domain, Ω, that is, for each fiber point, there is another point in the concrete background with the same coordinates.

Secondly, the problem statement is reformulated by adapting the equilibrium equations (4.1) to this new geometry. The unknown displacement field $\boldsymbol{u}$ takes values in every point $\boldsymbol{x} \in \Omega$. The compatibility of displacements between the concrete bulk and the fiber cloud is ensured by the fact that $\widetilde{\Omega_S} \subset \Omega$. The equilibrium equations in

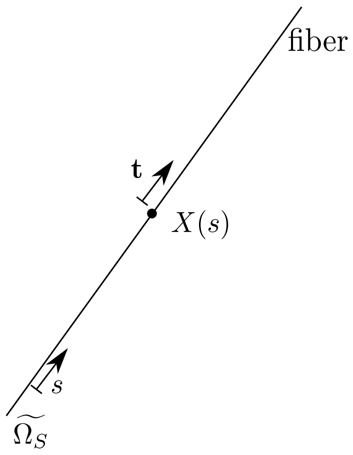

Figure 4.3: Fiber parametrization

the concrete bulk (4.1a), (4.1c) and (4.1d) read

$$-\nabla \cdot \boldsymbol{\sigma}(\boldsymbol{u}) = \boldsymbol{b}_C + \boldsymbol{f}_{S\to C} \qquad \text{in } \Omega \tag{4.2a}$$

$$\boldsymbol{\sigma}(\boldsymbol{u}) \cdot \boldsymbol{n} = g_N \qquad \text{on } \Gamma_N \tag{4.2b}$$

$$\boldsymbol{u} = \boldsymbol{u_D} \qquad \text{on } \Gamma_D \tag{4.2c}$$

being $\boldsymbol{f}_{S\to C}$ the interaction force accounting for the effect of the fibers in the concrete bulk described by equation (4.1e).

The interaction force $\boldsymbol{f}_{S\to C}$ is defined taking into account the equilibrium equation in the fibers, (4.1b). An arc length s is introduced for each fiber using the parametrization $X(s)$, as illustrated in figure 4.3. The displacement along the fiber is given by the displacement field $\boldsymbol{u}$ taking values in the concrete bulk, the restriction of $\boldsymbol{u}$ to $\widetilde{\Omega_S}$ is denoted by $\boldsymbol{u}_S$.

The expression for $\boldsymbol{f}_{S\to C}$ at a point $\boldsymbol{x} \in \widetilde{\Omega_S} \subset \Omega$ is given by

$$\boldsymbol{f}_{S\to C}(\boldsymbol{x}) = \int_{\widetilde{\Omega_S}} \boldsymbol{f}(s)\delta_0(\boldsymbol{x} - \boldsymbol{X}(s))ds. \tag{4.3}$$

where δ_0 is the Dirac delta and $\boldsymbol{f}(s)$ is a force density distributed along the fiber line and defined as

$$\boldsymbol{f}(s) = \frac{d\,\sigma_S(\boldsymbol{u}_S)}{d\,s}\boldsymbol{t} \tag{4.4}$$

being σ_S a unidimensional stress defined in the fiber and $\boldsymbol{t}$ the unit vector in this direction. Fibers are considered with no bending stiffness, therefore, $\boldsymbol{f}(s)$ is defined as aligned with the longitudinal direction (normal to the cross section).

4.3 Discrete approach for coupling the model for the concrete bulk and the fiber cloud

The problem is discretized defining independently one mesh for the concrete bulk and one mesh for the fiber cloud. The mesh for the concrete bulk is kept simple while preserving the geometrical features of the sample, for instance the notch, see figure 4.4. The discretization of the fiber cloud is a series of straight bar elements (in the examples included in this work each fiber is discretized with five elements). No conformity or geometrical matching is enforced between the discretizations of the concrete bulk and the fiber cloud. For a given discretization, the corresponding unknowns of the discrete problem are the nodal values of the displacements in the concrete bulk and in the steel fiber cloud. These nodal vectors are denoted by u_c and u_s respectively and they are *a priori* independent. The displacement compatibility must be enforced specifically. The discrete form of the equilibrium equations (4.2) (equilibrium in the concrete bulk), is expressed in terms of nodal force vectors and reads

$$F_c^{\text{int}} = F_c^{\text{ext}} + F_{s\to c}, \tag{4.5}$$

where the nodal vector F_c^{ext} is the discrete version of the external force vector and accounts for the effect of $\boldsymbol{b}_C$ and g_N, $F_{s\to c}$ stands for the discrete form of $\boldsymbol{f}_{S\to C}$ and F_c^{int} corresponds to the internal forces, that is, the discrete vector version of $-\nabla \cdot \boldsymbol{\sigma}(\boldsymbol{u})$.

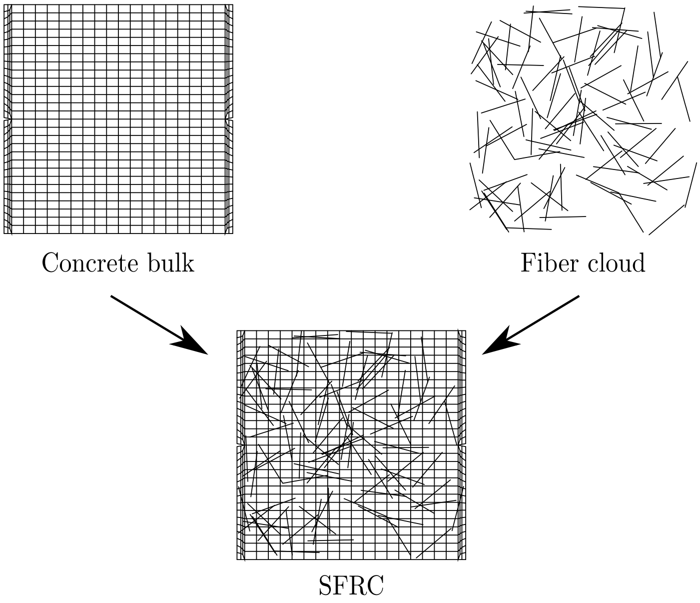

Figure 4.4: Non conforming meshes for the concrete bulk and the fiber cloud

A similar expression holds for the equilibrium in the fiber cloud:

$$F_s^{\text{int}} = F_s^{\text{ext}} + F_{c \to s} \tag{4.6}$$

where the first terms are analogous to the previous equation and $F_{c \to s}$ is an interaction force from the concrete bulk into the steel fibers.

4.3.1 Linear case

In the case the concrete bulk is assumed to be linear, the following relation holds: $F_c^{\text{int}} = K_c u_c$, being K_c the stiffness matrix of the concrete bulk. In the same basis, if the mechanical behavior of the fibers is linear, one has that $F_s^{\text{int}} = K_s u_s$, being K_s the stiffness matrix of the fiber cloud. The displacement compatibility between the displacement fields in the concrete bulk and the fiber cloud, u_c and u_s is expressed in algebraic form via the projection operator Π: $u_s = \Pi u_c$. This linear restriction is enforced via the Lagrange multipliers method. When added to the discrete equilibrium equations (4.5) and (4.6), the following system yields

$$\begin{bmatrix} K_c & 0 & \Pi^{\mathsf{T}} \\ 0 & K_s & -I_s \\ \Pi & -I_s & 0 \end{bmatrix} \begin{bmatrix} u_c \\ u_s \\ \widetilde{\lambda} \end{bmatrix} = \begin{bmatrix} F_c^{\text{ext}} \\ F_s^{\text{ext}} \\ 0 \end{bmatrix},$$

Note that the number of rows of the matrix Π corresponds to the number of degrees of freedom of the fibers and its number of columns is the number of degrees of freedom of the concrete bulk.

In order to identify the discrete interaction forces, $F_{s\to c}$ and $F_{c\to s}$, the previous system is rewritten as

$$\left\{ \begin{array}{rcll} K_c u_c & = & F_c^{\text{ext}} - \Pi^{\mathsf{T}} \widetilde{\lambda} & \text{concrete equilibrium} \\ K_s u_s & = & F_s^{\text{ext}} + \widetilde{\lambda} & \text{fiber cloud equilibrium} \\ \Pi u_c & = & u_s & \text{displacement compatibility} \end{array} \right.$$

that is, the interaction force from the fibers to the concrete is $F_{s\to c}(u_s) = -\Pi^{\mathsf{T}} \widetilde{\lambda}$ and the interaction force from the concrete to the fibers is precisely the Lagrange Multiplier, $F_{c\to s}(u_c) = \widetilde{\lambda}$.

In the remainder of the thesis, and according with the hypothesis of neglecting the volume of the steel fibers, the external forces on the fibers are also assumed to be zero, $F_s^{\text{ext}} = 0$.

Remark 1. *Essential boundary conditions in the concrete bulk. In SFRC, Dirichlet boundary conditions are imposed only in the concrete bulk. The general form of a linear restriction is $Au_c^* = u_D^*$, being A a rectangular matrix and u_D^* the vector of prescribed values. Considering Lagrange multipliers for imposing these boundary conditions, the concrete stiffness (K_c), displacement (u_c) and the external forces (F_c^{ext}) are defined* *as follows:*

$$K_c = \begin{bmatrix} K_c^* & A^T \\ A & 0 \end{bmatrix}, \; u_c = \begin{bmatrix} u_c^* \\ \lambda^* \end{bmatrix} \; \textit{and } F_c^{ext} = \begin{bmatrix} F_c^{ext*} \\ u_D^* \end{bmatrix}$$

being K_c^* *and* u_c^* *the structural concrete stiffness and displacement, respectively, without the Lagrange multipliers. Vector* λ^* *is the Lagrange multiplier and* F_c^{ext*} *represents the external load applied in the concrete bulk.*

Therefore, the system to be solved for the problem considering the Lagrange Multipliers method without accounting for the fibers interaction would be

$$K_c u_c = F_c^{ext}.$$

Thus, this allows writing in a unified manner the loading term, both if displacements or forces are prescribed.

4.3.2 Nonlinear case

In a realistic case, fibers and concrete are modeled as nonlinear materials. Thus, the general form of the discrete nonlinear system to be solved reads:

$$\begin{aligned} F_c^{\text{int}}(u_c) &= F_c^{\text{ext}} + F_{s\to c}(u_s) \\ F_s^{\text{int}}(u_s) &= F_{c\to s}(u_c) \\ \Pi u_c &= u_s \end{aligned}$$

A classical incremental-iterative approach is used. The external load is split into loading steps. The external load in the concrete at step k is denoted by $F_c^{\text{ext},k}$. The generic load increment is denoted by ΔF_c^{ext}, such that $F_c^{\text{ext},k+1} = F_c^{\text{ext},k} + \Delta F_c^{\text{ext}}$ (for the sake of simplicity, the notation omits the dependence on k of the increments).

It is assumed that equilibrium is reached for step k (step k is converged), namely u_c^k, u_s^k, $F_{c\to s}^k$ and $F_{s\to c}^k$ are known and satisfy

$$\begin{aligned} F_c^{\text{int}}(u_c^k) &= F_c^{\text{ext},k} + F_{c\to s}^k \\ F_c^{\text{int}}(u_c^k) &= F_{s\to c}^k \\ \Pi u_c^k &= u_s^k \end{aligned}$$

Then, we seek the solution at the next step $k+1$. The problem reads, given the solution at step k and ΔF_c^{ext}, find u_c^{k+1}, u_s^{k+1}, $F_{c\to s}^{k+1}$ and $F_{s\to c}^{k+1}$ satisfying

$$\begin{aligned} F_c^{\text{int}}(u_c^{k+1}) &= F_c^{\text{ext},k+1} + F_{c\to s}^{k+1} = F_c^{\text{ext},k} + \Delta F_c^{\text{ext}} + F_{c\to s}^{k+1} \\ F_s^{\text{int}}(u_s^{k+1}) &= F_{s\to c}^{k+1} \\ \Pi u_c^{k+1} &= u_s^{k+1} \end{aligned}$$

In order to solve the incremental nonlinear problem, an iterative method is used. iterations are required for finding Δu_c and Δu_s such as:

$$\begin{aligned} u_c^{k+1} &= u_c^k + \Delta u_c \\ u_s^{k+1} &= u_s^k + \Delta u_s \end{aligned}$$

Therefore, assuming the approximation

$$\begin{aligned} F_c^{\text{int}}(u_c^{k+1}) &\approx F_c^{\text{int}}(u_c^k) + K_c \Delta u_c \\ F_s^{\text{int}}(u_c^{k+1}) &\approx F_s^{\text{int}}(u_s^k) + K_s \Delta u_s \end{aligned}$$

the initial trial increment (iteration $i = 0$) aims at determining the approximations $\delta u_{c,0}$ and $\delta u_{s,0}$ to Δu_c and Δu_s. The first iteration is then computed by solving the following system of equations:

$$\begin{bmatrix} K_c & 0 & \Pi^{\mathsf{T}} \\ 0 & K_s & -I_f \\ \Pi & -I_f & 0 \end{bmatrix} \begin{bmatrix} \delta u_{c,0} \\ \delta u_{s,0} \\ \widetilde{\lambda} \end{bmatrix} = \begin{bmatrix} \Delta F_c^{\text{ext}} \\ 0 \\ 0 \end{bmatrix}.$$

being $\widetilde{\lambda}$ the corresponding Lagrange multiplier.

For the next iterations, $i = 1, 2, 3 \ldots$, the displacement increments are assumed to have the form $\Delta u_c \approx \sum_{j=0}^{i} \delta u_{c,j}$ and $\Delta u_s \approx \sum_{j=0}^{i} \delta u_{s,j}$.

Since the approximation to u_c^{k+1} and u_s^{k+1} at iteration $i-1$ is available, the residual is computed as

$$\begin{aligned} r_{c,i-1} &= F_c^{\mathrm{ext},k+1} - F_c^{\mathrm{int}}(u_c^{k+1}) - \Pi^{\mathsf{T}}\widetilde{\lambda} \\ r_{s,i-1} &= F_s^{\mathrm{int}}(u_s^{k+1}) - \widetilde{\lambda} \end{aligned}$$

The next iteration i is obtained solving

$$\begin{bmatrix} K_c & 0 & \Pi^{\mathsf{T}} \\ 0 & K_s & -I_f \\ \Pi & -I_f & 0 \end{bmatrix} \begin{bmatrix} \delta u_{c,i} \\ \delta u_{s,i} \\ \widetilde{\lambda} \end{bmatrix} = \begin{bmatrix} r_{c,i-1} \\ r_{s,i-1} \\ 0 \end{bmatrix}.$$

For each loading step, the iteration loop is performed until convergence is reached. The stopping criterion consists in fulfilling simultaneously the following conditions: $\|r_{c,i}\| < tol_r$, $\|r_{s,i}\| < tol_r$ and $\|\Delta u_{c,i}\| < tol_u$, being tol_r and tol_u the prescribed tolerances for the residual and the displacement, respectively.

4.4 Modeling the nonlinear behavior: a phenomenological mesomodel

The approach introduced above allows defining the constitutive models for the concrete bulk and the steel fiber cloud independently. This section is devoted to describe the models used for both materials. A classical nonlocal damage model is proposed for concrete. The steel fiber cloud is modeled using an elasto-plastic mesomodel accounting for the interaction between plain concrete and steel fibers.

4.4.1 Plain concrete

Concrete is a brittle material which can be modeled considering both continuous and discontinuous models. Pros et al. (2011b) consider two different alternatives for plain concrete. On one hand, a continuous model: Mazars damage model. In this case the model is considered nonlocal in order to avoid mesh dependence. The failure pattern is obtained and the value of the maximum vertical load (which is the variable chosen for validate the numerical models) is satisfactory. On the other hand, a discontinuous model is considered: the failure pattern is known *a priori* (through the experimental results and the numerical results from considering the continuous model) and it is modeled considering joint elements (allowing both sliding and separation), while the rest of the specimen is elastic. Although it is necessary to know the fracture pattern before the simulation, the results are also close to the experimental ones.

Therefore, these alternatives can be considered for modeling plain concrete, as well as any other nonlinear model available and suitable for plain concrete.

Another useful damage model is the one presented by Oliver et al. (2008) with less material parameters and easier to control than the Mazars damage model. For the examples in the present work, this damage model is considered. The general formulation of this damage model is introduced by Oliver et al. (2008) and Oliver (2002). In the latter, the author shows that the model is regularized because it involves an internal length parameter.

4.4.2 Steel fibers and concrete-fiber interaction

The model considered for steel fibers accounts for the whole process of slipping and debonding of the fiber into plain concrete and, precisely, allows capturing the whole behavior between the fibers and plain concrete bulk. Therefore, an elasto-plastic angle dependent model with softening is adopted for the steel fibers. The interaction is modeled with the monolithic model imposing displacement compatibility described in the previous sections of this chapter (based in the IBM). The concept of monolithic strategy is used here by opposition to the strategy devised by Pros et al. (2008) in which the linear system of equations is solved using a staggered scheme corresponding to a block Gauss-Seidel method.

An alternative approach would be considering steel fibers being modeled with an elasto-plastic model and the interaction between concrete and fibers defined describing the whole process (slipping, folding, debonding,etc.). Although the steel fiber model would be easy, the interaction is more complex to perform.

The mesomodel for the steel fibers is expected to account for the whole interaction process between concrete and fibers and to characterize the behavior of the steel fibers. This aims at describing the effect of different phenomena, resulting in a global behavior at the meso-scale. The mesomodel is assumed to include in a single constitutive relation the effects of the nonlinear behavior of the steel, the slipping, folding, debonding and also the sliding of the fiber with respect to the concrete. Thus, the constitutive equations of steel fibers are deduced from experimental results and analytical descriptions of pullout tests.

Pullout tests consist of a plain concrete specimen with only one steel fiber immersed on it, which is pulled out. In figure 4.5, the scheme of a pullout test is presented. Fortunately, there is a recent analytical phenomenological description of pullout tests is available based on experimental results (Laranjeira et al. (2010a,b)). These analytical expressions depend on the angle between the fiber and the load direction (ϕ), represented in figure 4.5, and on the shape of the fiber, which can be straight or hooked (as displayed in figure 4.6). The whole expressions are described in Appendix A.

For the case of considering straight fibers, the pullout results presented by Laranjeira et al. (2010a) are reproduced in figure 4.7. Different results are presented considering different orientations of the fibers (with reference to the load direction).

In this thesis, the outputs from the pullout tests, crack width and pullout load (w, P) are translated into the constitutive equations for the steel fibers (ε, σ) following the expressions for a given discretization of the steel fibers

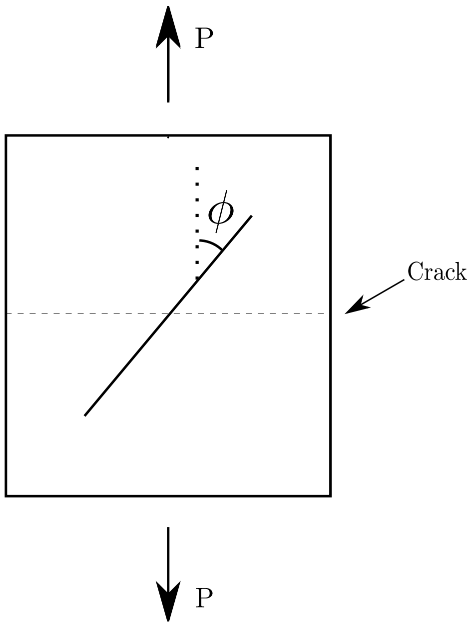

Figure 4.5: Pullout test scheme with the angle (ϕ) between the fiber and the loading direction

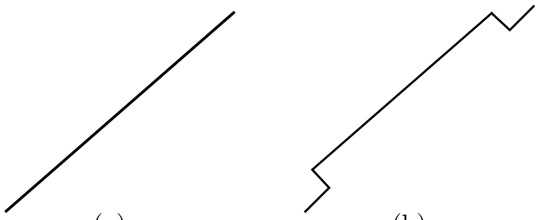
(a) (b)

Figure 4.6: Different shape of the fiber: (a) straight and (b) hooked

$$
\begin{aligned}
P \rightarrow \sigma &= \frac{P}{A_{\text{fiber}} \cdot \cos\phi} \\
w \rightarrow \varepsilon &= \begin{cases} \dfrac{w \cdot \cos\phi}{L} & \text{if} \quad w \leq w_1 \\ \dfrac{w_1 \cdot \cos\phi}{L} + \dfrac{(w - w_1) \cdot \cos\phi}{L_{\text{elem}}} & \text{if} \quad w \geq w_1 \end{cases}
\end{aligned}
\tag{4.7}
$$

with A_{fiber} and L standing for the area and the length of the fiber, respectively, and L_{elem} being the element size of the fiber (for the given discretization). It is considered that while the fiber has not plastified ($w \leq w_1$), the whole geometry of the fiber has the same behavior. However, once the fiber has plastified ($w \geq w_1$), the deformation

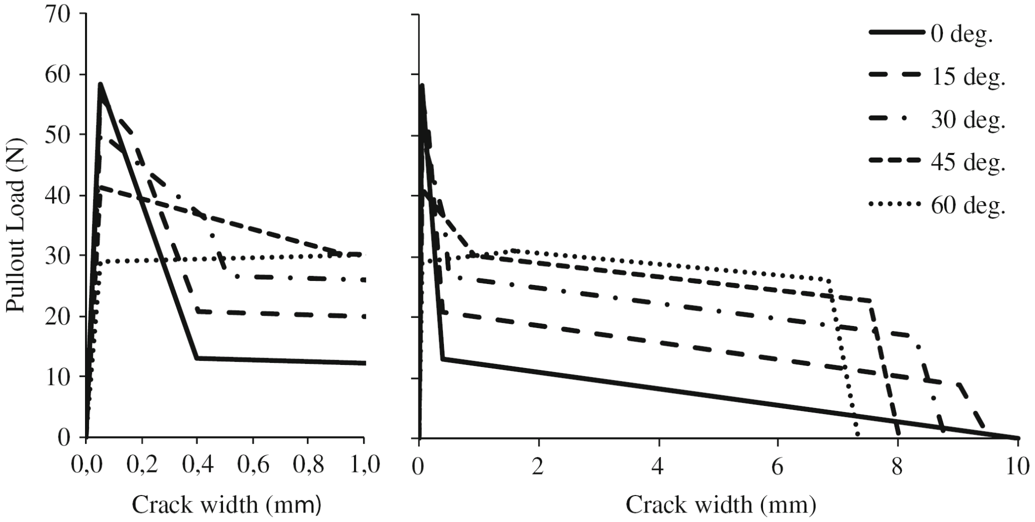

Figure 4.7: Pullout test results considering straight fibers for different values of ϕ, image from Laranjeira et al. (2010a).

of the fiber is supposed to be concentred only in one element of the fiber.

$(w,\ P)$ are defined in the axis of the pullout test, as presented in figure 4.8, and the constitutive equations of the fibers $(\varepsilon,\ \sigma)$ must be defined in the axis of the fiber. Therefore, it is necessary to project $(w,\ P)$ into the fiber: $(w_F,\ P_F)$, being $P_F = P\cos\phi$ the tension of the fiber and $w_F = \dfrac{w}{\cos\phi}$ the fiber elongation associated with the crack.

In general, the angle is computed between the fiber and the normal direction of the fracture pattern. However, for the pullout tests, the load direction is perpendicular to the failure pattern, therefore, the normal direction coincides with the load direction.

In the common situations the volumetric proportion of steel fibers into plain concrete is $\leq 1\%$. In this case, the behavior of the fiber inside concrete is the same as if it was isolated, and it is not necessary taking into the account the fiber-fiber interaction. However, if the volumetric proportion of fibers is larger than 1%, this assumption may be unrealistic. Accounting for the fiber-fiber interaction is out of the scope of this thesis.

Therefore, for each fiber immersed in the concrete bulk, a different constitutive equation is considered depending on its shape (straight or hooked) and on the angle

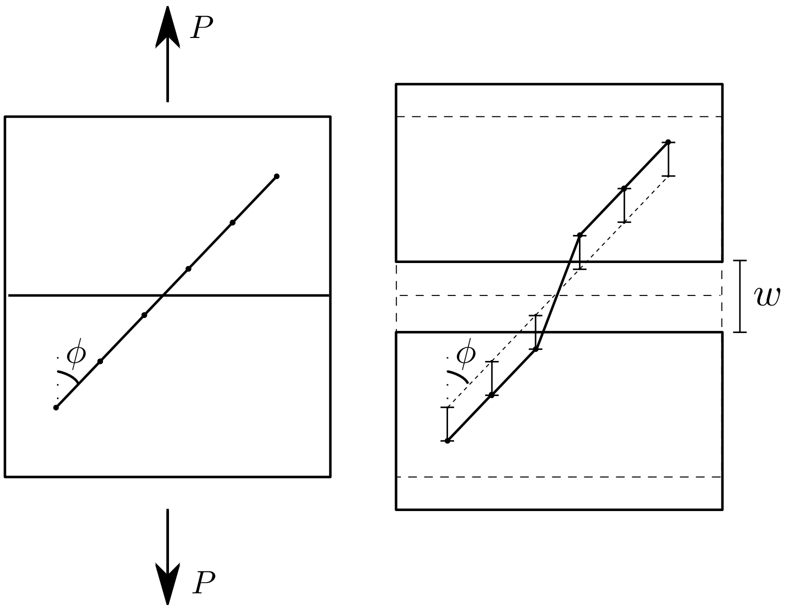

Figure 4.8: w and P before and after the cracking.

between the considered fiber and the normal direction of the failure pattern. In figure 4.9, different constitutive equations are presented for different angles and considering both straight and hooked fibers. These equations are obtained through analytical expressions of the pullout tests and defined in the fiber axis.

It is observed that the presented constitutive equations are angle dependent with softening and at the final stages of the deformation, the stresses (σ) tend to zero.

4.5 Examples

After describing the numerical approach for modeling plain concrete, two numerical examples are presented. On one hand, two pullout tests considering different orientations of the fibers are showed and, on the other hand, a direct tension test is simulated. Both cases are academic examples in two dimensions under the condition of plane stress.

In all the examples presented in the present work, plain concrete is modeled with the damage model explained by Oliver et al. (2008). For all cases: plain concrete and

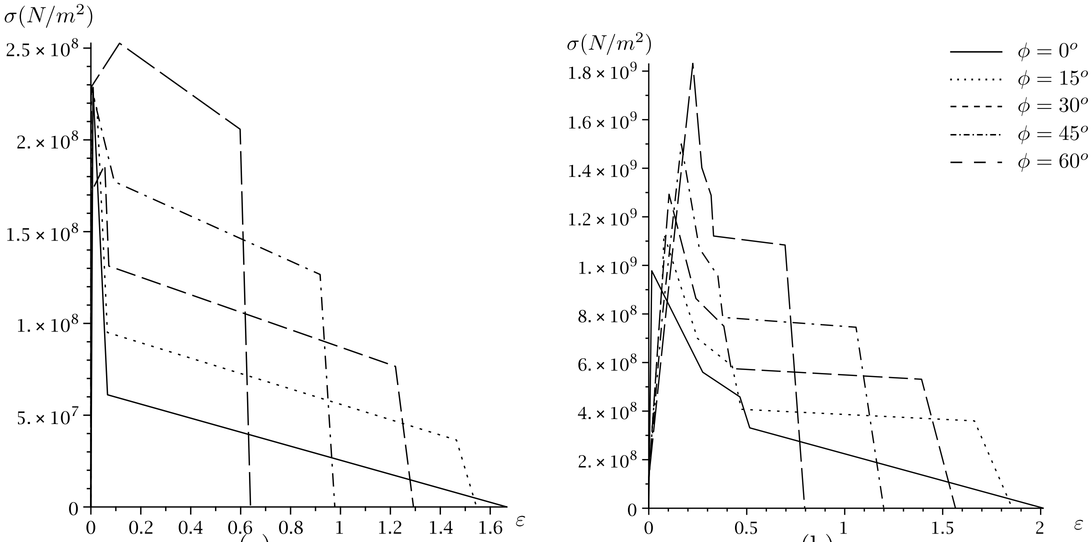

(a) (b)

Figure 4.9: Constitutive equations for steel fibers with different orientation considering both straight (a) and hooked (b) shapes.

SFRC, the material parameters considered are the same (table 4.1).

Table 4.1: Material parameters for the damage model for plain concrete

Young Modulus	$E = 30 \cdot 10^9$Pa
Poisson coefficient	$\mu = 0$
Fracture energy	$\sigma_u = 10$N
Element size	$l_e = 0.5$mm
Tensile strength	$f_t = 3.5 \cdot 10^6$Pa

4.5.1 Pullout test

Herein, two pullout tests are reproduced. The size of the fibers considered in both cases is presented in table 4.2 and the concrete specimen size is 25mm × 12.5mm.

First, as represented in figure 4.10(a), a straight single fiber with no inclination with respect to the load direction is considered immersed on the plain concrete. The steel fiber is fixed (in the bottom part of the concrete specimen, which is not included

Table 4.2: Fiber dimensions for the pullout tests

Length	Embedded length	Diameter
30mm	10mm	0.5mm

in the model) and the top part of the concrete bulk is pulled up considering prescribed displacements at the top of the specimen. The nodes of the fiber embedded in the lower part are blocked, assuming that all the deformation is concentrated in the rest of the fiber. Plain concrete is simulated considering a damage model. The constitutive equation of the steel fiber is taken from figure 4.9(a) and Appendix A for the case of straight fibers and $\phi = 0^o$. Moreover, in figure 4.10(b), the results are displayed in a load-displacement curve. Qualitatively, the behavior of the numerical model is in good agreement with the corresponding results obtained experimentally (Laranjeira et al. (2010a)) and to the curves presented in figure 4.7. In order to obtain a quantitative matching of the model, the concrete model has to be further validated.

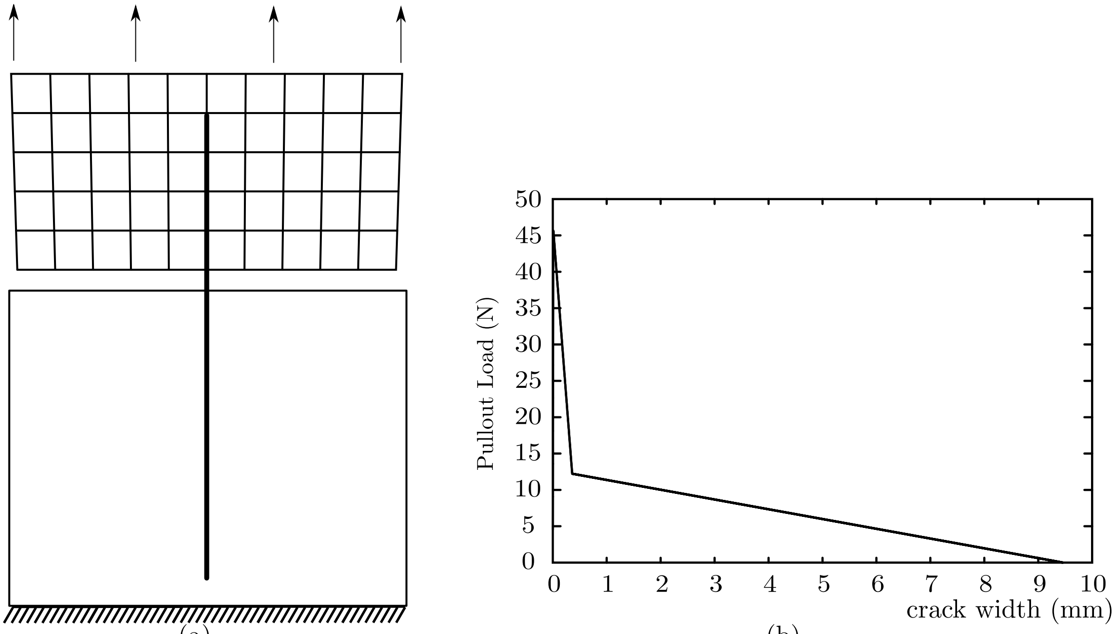

(a) (b)

Figure 4.10: Pullout test considering $\phi = 0^o$

After considering a straight fiber with no inclination, another case is simulated: the pullout test considering an inclined straight fiber with $\phi = 30^o$ immersed in the plain concrete. Again, displacements are prescribed at the top of the plain concrete specimen and the fiber is fixed. Herein, the model for the plain concrete is the same than in the previous case, the damage model, but the constitutive equation of the fiber is different, based on the information from the figure 4.9(a) and Appendix A. In figure 4.11(a), the scheme of the example is presented and in figure 4.11(b) the obtained results are shown in a load-displacement curve which is the expected one (Laranjeira et al. (2010a)).

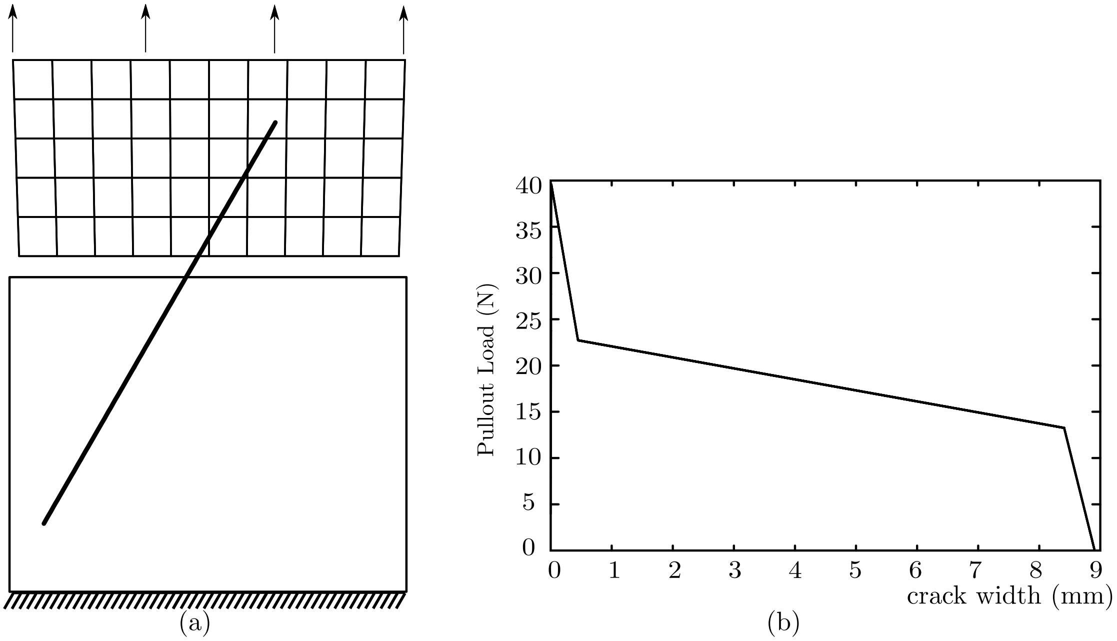

(a) (b)

Figure 4.11: Pullout test considering $\phi = 30^o$

In both examples of pullout tests, it is observed that the obtained curve (w, P) is in good agreement with the results obtained experimentally and to the analytical curves presented by Laranjeira et al. (2010a) corresponding to each case (depending on the orientation of the fiber), as expected. That is due to the fact that the constitutive equation of each fiber is deduced form pullout results depending on the angle.

4.5.2 Direct tension test

The direct tension test is simulated considering three different cases: (a) only plain concrete (figure 4.12(a)), (b) SFRC with straight fibers (figure 4.12(b)) and (c) SFRC with hooked fibers (figure 4.12(c)). The direct tension test consists in a rectangular specimen made of plain concrete or SFRC fixed at the bottom and under a direct load pulling at the top (shown in figure 4.12), precisely, prescribed displacements are considered at the top of the concrete specimen. The size of the specimen of plain concrete is 75mm × 75mm in all the examples of the direct tension loading presented. The simulation is carried out considering plane stress and the considered thickness of the specimen is 75mm.

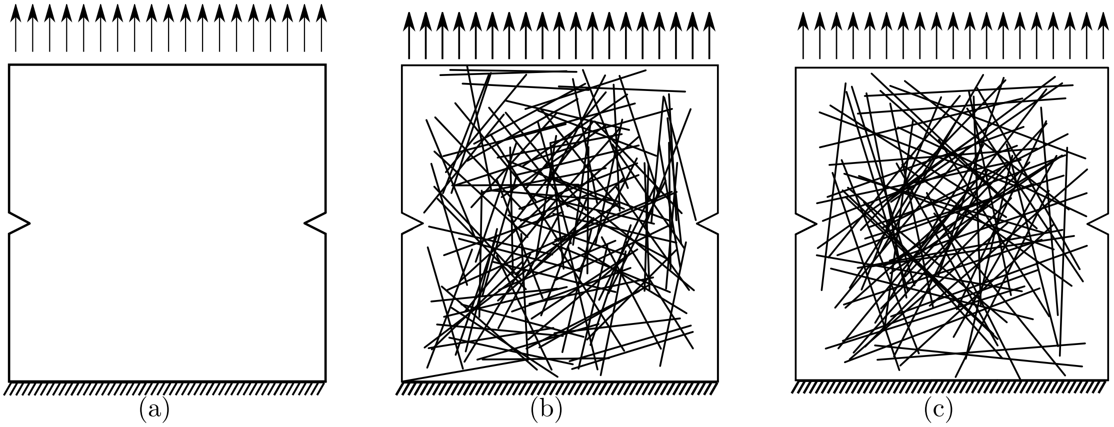

Figure 4.12: Direct tension test considering (a) plain concrete, (b) SFRC with straight fibers and (c) SFRC with hooked fibers

In order to avoid damage dispersion and to ensure having the crack pattern placed in the same place for all the cases, a notch is performed in the three meshes.

For the case of SFRC, the steel fibers are distributed and orientated randomly into the plain concrete bulk. Both the location of one end-point, p_i, and the angle of the fiber with respect to the horizontal, α, are assumed to be random variables with uniform probability distributions. That means that, for rectangular domains, each coordinate of p_i ranges in a real interval and α ranges in $[0, \pi[$ (three random variables in 2D that would turn out to be five, three coordinates and two angles, in

3D). Since the length of the fibers, L, is given as problem data, once p_i and α are generated, the other end-point of the fiber is readily computed by doing

$$p_f = p_i + L\,(\cos\alpha, \sin\alpha).$$

If the end-point p_f lies outside of the concrete domain, the fiber generated is discarded.

In table 4.3 the dimensions of the fibers (based on the values presented by Laranjeira (2010)) for each case are displayed.

Table 4.3: Fiber dimensions

Shape	Length	Diameter	Number of fibers
Straight	30mm	0.5mm	140
Hooked	50mm	0.5mm	84

For the two cases of SFRC, as the length of the fibers is not the same for straight fibers than for hooked fibers, different quantities of fibers are considered into plain concrete. In order to compare under the same conditions, the same volumetric substitution amount of steel fibers into plain concrete are considered: 0.23%.

For the steel fibers, the constitutive equations considered are based on figure 4.9 and Appendix A. The corresponding angle between the fiber and the load direction (which is perpendicular to the failure zone and, thus, coincides with the normal direction of the failure pattern) is computed and then, the corresponding constitutive equation is defined considering the equations and the input data presented in Appendix A.

In figure 4.13, the obtained results from the simulation of the direct tension test are presented: three load-displacement curves (one for each case: plain concrete, SFRC with straight fibers and SFRC with hooked fibers) in which one can observe (a) the increase of the fracture energy and (b) the appearance of the residual strength due to the presence of the steel fibers into plain concrete. Moreover, it is observed that the appeared residual strength is higher for the SFRC with hooked fibers than for the SFRC with straight fibers. Therefore, the effects of the fibers are captured and, moreover, it is observed that hooked fibers influence more than straight fibres into the plain concrete. For a better analysis of the results, a zoom near to the load peak is done and presented in figure 4.14.

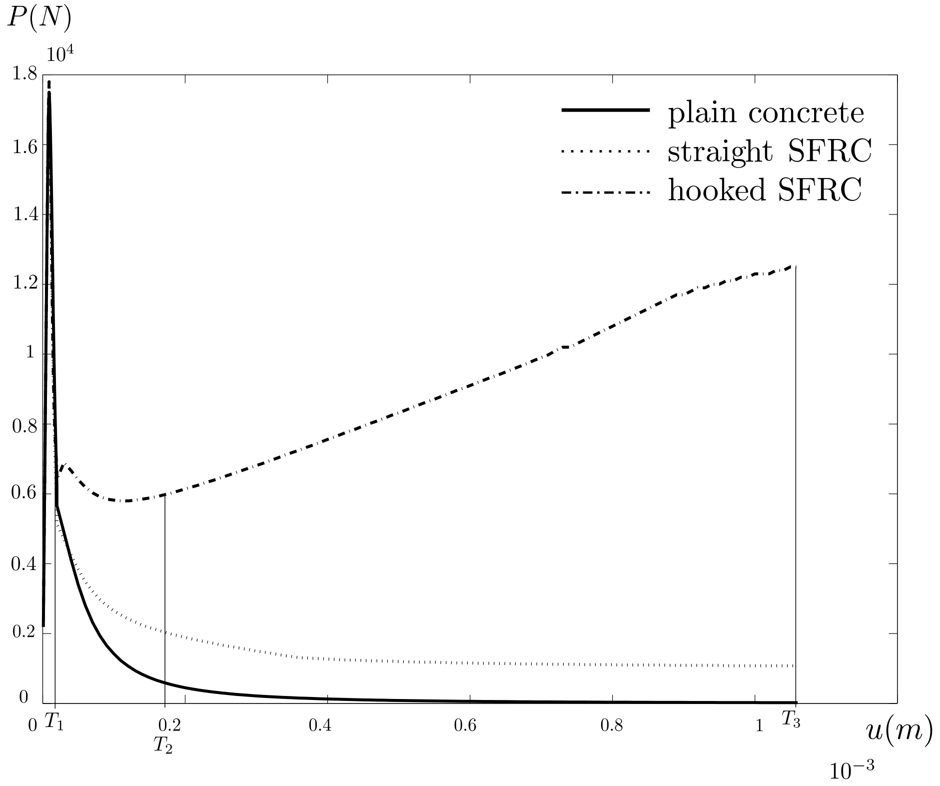

Figure 4.13: Direct tension test results considering plain concrete, SFRC with straight fibers and SFRC with hooked fibers.

In order to study the behavior in all the cases, three sampling times (pseudo-time in the quasistatic loading process) are selected, T_1, T_2 and T_3, as represented in figure 4.13. The initial time step is represented by T_0. On one hand, figures 4.15, 4.16 and 4.17 show the deformed mesh of plain concrete in this three different time steps and in the initial step, for the three different materials: plain concrete, SFRC considering straight fibers and SFRC with hooked fibers. The influence of the fibers is observed in these deformed meshes.

Note that the deformed meshes for both straight and hooked fibers are practically equal (figures 4.16 and 4.17). The differences between the two types of fibers appear

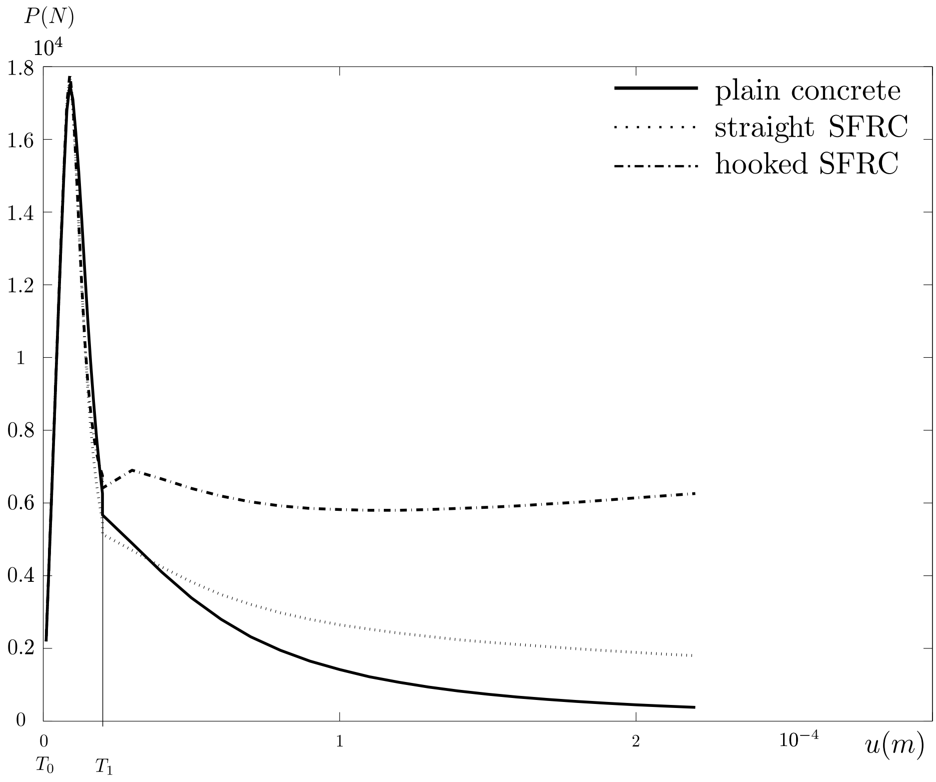

Figure 4.14: Zoom of the direct tension test results considering plain concrete, SFRC with straight fibers and SFRC with hooked fibers.

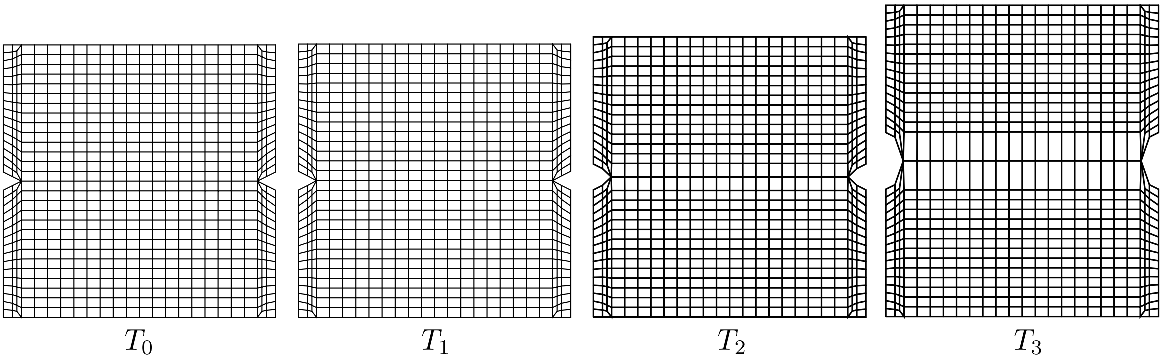

Figure 4.15: Deformed meshes for plain concrete (amplified ×10)

in the load-displacement curves (figures 4.13 and 4.14). The tests are displacement driven and therefore the displacement fields (and hence the deformed meshes) are similar.

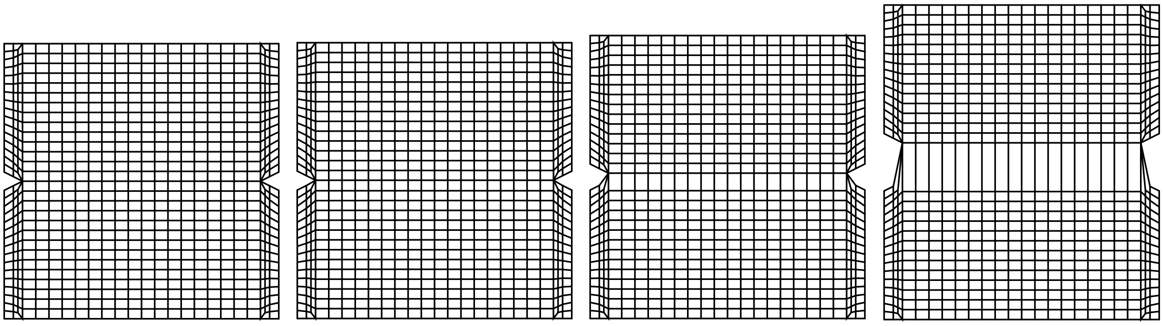

T_0 T_1 T_2 T_3

Figure 4.16: Deformed meshes for straight SFRC (amplified ×10)

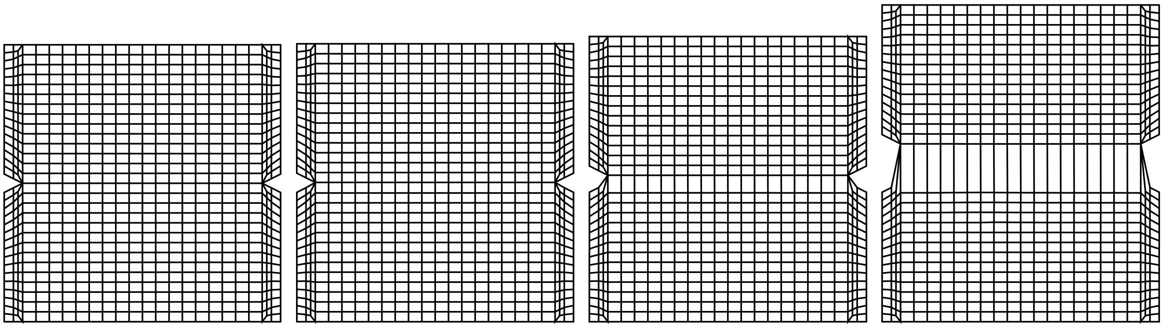

T_0 T_1 T_2 T_3

Figure 4.17: Deformed meshes for hooked SFRC (amplified ×10)

On the other hand, figures 4.18 and 4.19 show the fibers that are not in the elastic range (plastified) in the different time steps for the case of SFRC considering straight fibers and hooked fibers, respectively. The number of the plastified fibers is presented in brackets for each case. It is observed that the plastified fibers are the ones that cross the fracture pattern and the number of plastified fibers increases with the time. Moreover, there are more plastified hooked fibers than straight fibers due to the fact that hooked fibers are longer and, therefore, more hooked fibers cross the fracture pattern.

For the whole comprehension of the behavior, three straight and three hooked fibers are studied in figures 4.20 and 4.21 considering the three time steps located into the constitutive equation of each different fiber for both cases. All the studied fibers

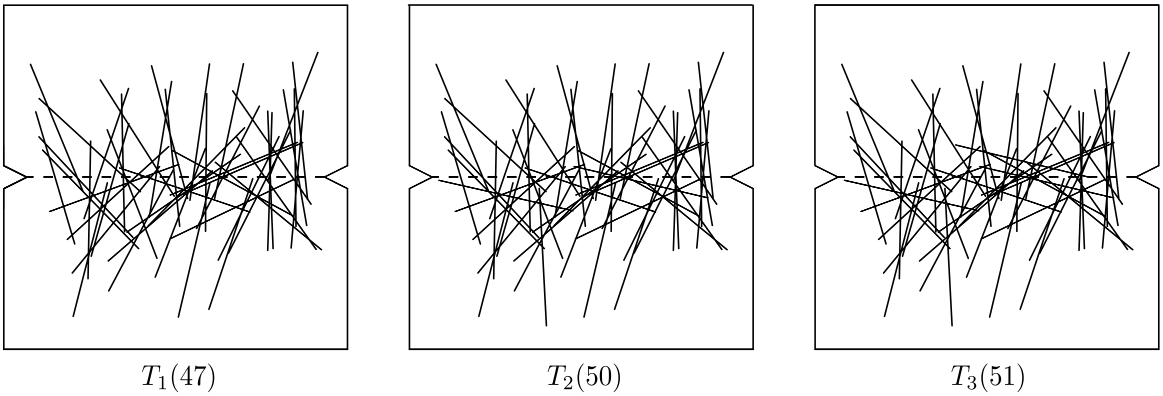

Figure 4.18: Straight fibers that have plastified in T_1, T_2 and T_3 with the number of plastified fibers in brackets.

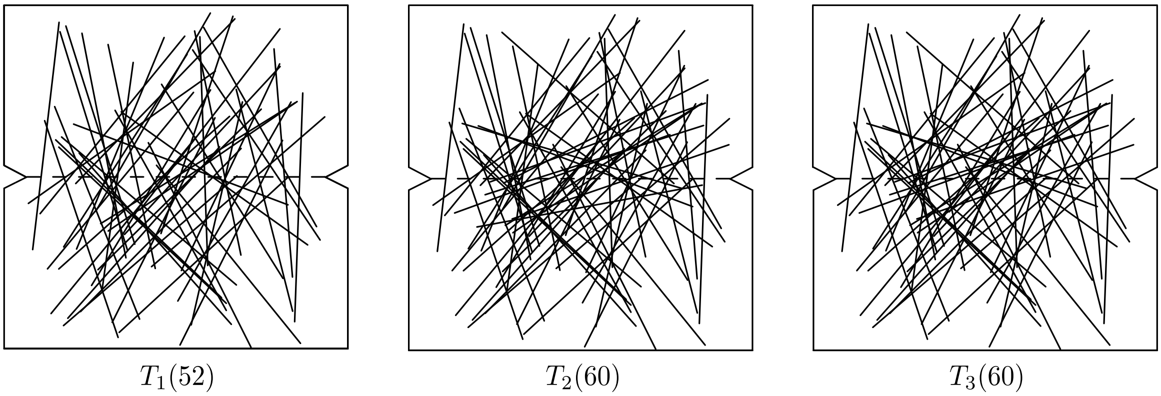

Figure 4.19: Hooked fibers that have plastified in T_1, T_2 and T_3 with the number of plastified fibers in brackets.

cross the fracture pattern, therefore, they are not in the elastic range, as observed.

4.6 Concluding remarks

A new numerical strategy is presented to numerically simulate SFRC. The main features of the proposed approach are the following:

- the mesh of the concrete bulk and the mesh of the fiber cloud are defined inde-

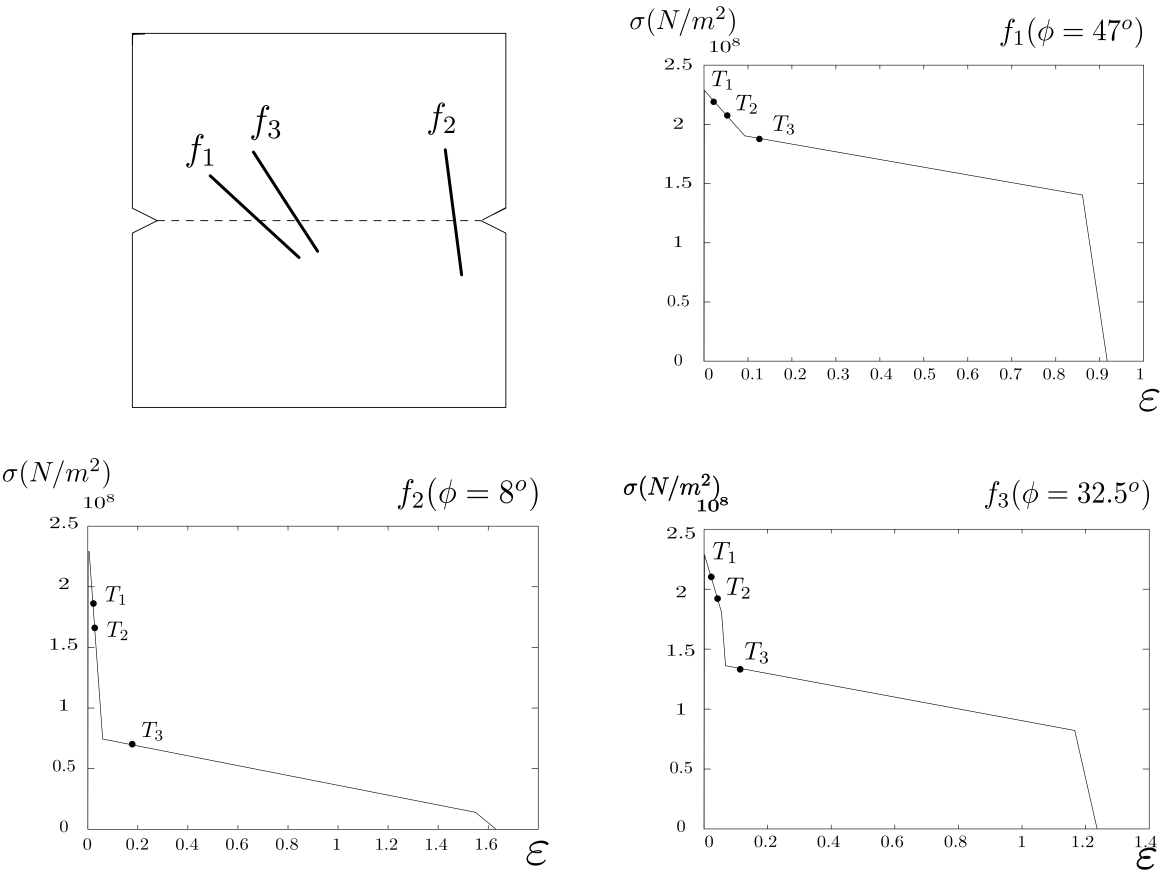

Figure 4.20: Straight fibers: behavior of three straight fibers (f_1, f_2 and f_3) crossing the crack with the constitutive equation of each fiber

pendently (nonconformal)

- the material models of the concrete bulk and the fiber cloud (which accounts also for the fiber-concrete interaction) are defined separately
- a phenomenological mesomodel is developed to characterize the constitutive equations for the steel fibers, accounting for the interaction with the concrete bulk
- coupling of the two systems (concrete and fibers) is based on the Immersed Boundary (IB) methods, imposing displacement compatibility and equilibrium

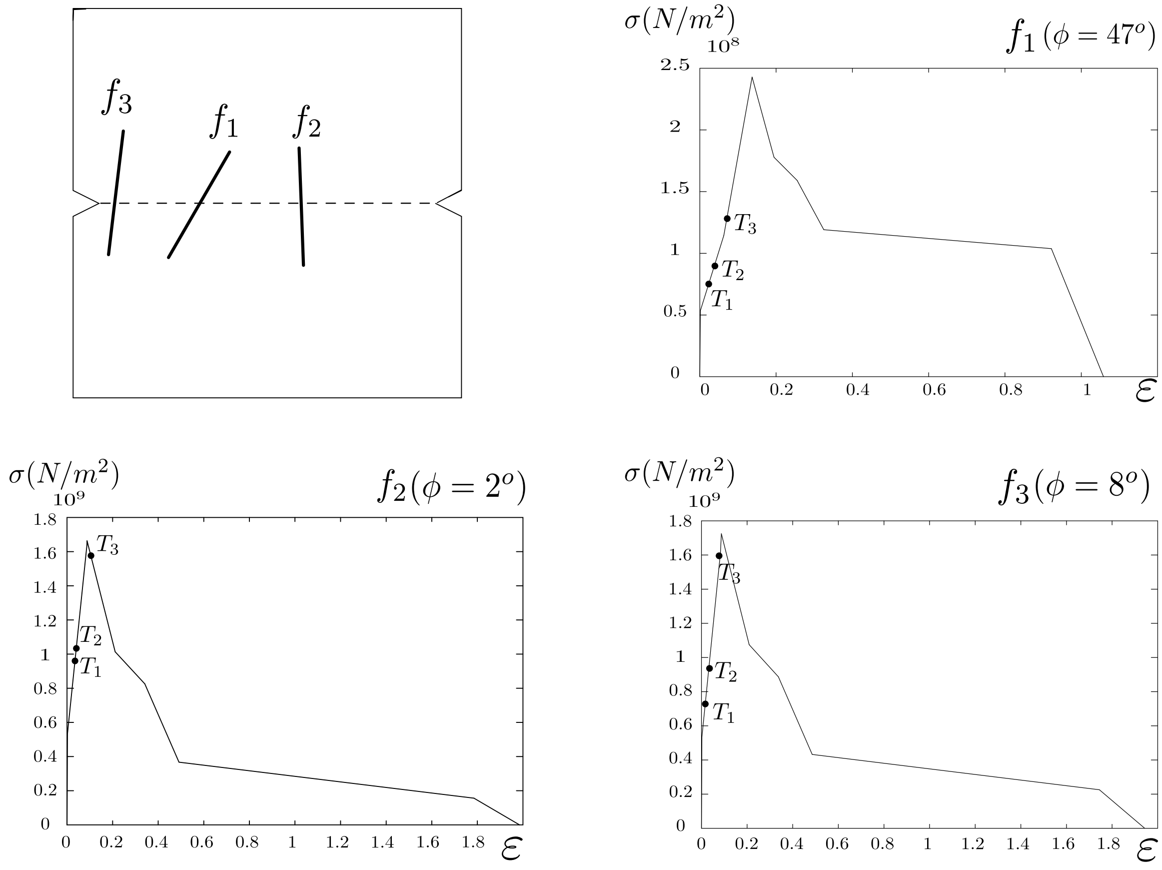

Figure 4.21: Hooked fibers: behavior of three hooked fibers (f_1, f_2 and f_3) crossing the crack with the constitutive equation of each fiber

The mesomodel is defined from the phenomenological analytical expressions describing the behavior of pullout tests. Thus, the constitutive equation for each steel fiber depends on (a) the angle between the fiber and the normal direction of the failure pattern (for the pullout test, the load direction coincides to the normal direction) and (b) the shape of the fiber. Further research has to be carried out to properly define the angle between each fiber and the crack pattern provided by the numerical model of the plain concrete bulk (the damage distribution). This is especially relevant in 3D cases.

The main advantage of this strategy is the possibility of using the actual number of fibers, with their location and orientation. In the examples, randomly distributed fiber clouds have been used. In this context, the 3D extension is straightforward and allows more realistic fiber distributions (in 2D, all the fibers are assumed to be coplanar).

In the application examples (two pullout tests with different fiber orientation and the direct tension test), the proposed strategy provides results in qualitative agreement with the experiments and expectations. For instance, the results of the direct tension test of SFRC show that both the energy dissipation and the residual strength increase when fibers are added.

Chapter 5

3D extension of the numerical approach for modeling SFRC. Experimental validation.

5.1 Introduction

In this chapter a three-dimensional extension of the tool proposed in chapter 4 is presented. The aim is to simulate the most used and common standard tests with SFRC accounting for the influence of the fibers in a realistic way (using both 3D meshes for the concrete matrix and 3D distributions and orientations of the fibers).

Working with 2D meshes for the concrete bulk, the whole behavior of the SFRC is not captured, due to the randomly distribution and orientation of the steel fibers into the plane (2D) corresponding to the concrete domain. Even under the hypotheses of plane stresses and strains or considering axisymmetric problems, the results are not realistic enough, because fibers are never oriented in a unique plane.

After describing the extension of the model to 3D, two tests are simulated in this chapter: the direct tension test (figure 2.3) and the three point bending test (figure 2.4).

Different experimental campaigns are available in the literature. In this chapter, on one hand, the campaign proposed by Laranjeira (2010), which consists of (1) the direct tension test with plain concrete and different quantities of steel fibers for the SFRC and (2) pullout tests with different fiber shapes and orientations inside the concrete specimen, is selected. On the other hand, an experimental campaign reproducing the three point bending test presented by Guàrdia (2007) is chosen.

The numerical results obtained considering the proposed numerical tool are compared to the results obtained experimentally. Therefore, the numerical approach is validated through these experimental campaigns.

The remainder of this chapter is structured as follows. First, in section 5.2, the numerical approach for modeling SFRC is presented. In section 5.3, the implementation of the numerical tool is described taking into account all the computational aspects. The experimental data from the two different experimental campaigns (one corresponding to the direct tension test and another one referring to the three point bending test) is described in section 5.4. In section 5.5, the numerical results obtained are presented and validated. All the computational problems are explained in section 5.6. Finally, in section 5.7, the most important conclusions are listed.

5.2 Numerical tool for modeling SFRC

For describing the numerical tool for modeling SFRC, firstly, the coupling between the two materials (concrete bulk and fiber cloud) is presented. Secondly, the two material models corresponding to the concrete bulk and the steel fibers are defined independently.

5.2.1 Coupling the concrete bulk and the fiber cloud

The main idea for coupling the concrete bulk and the fiber cloud is to enforce displacement compatibility between them. Following the ideas presented in chapter 4, this coupling is based on the Immersed Boundary (IB) methods (Boffi and Gastaldi (2003); Boffi et al. (2007); Mittal and Iaccarino (2003)), which were introduced for modeling problems with a solid structure immersed in a fluid domain. For modeling the SFRC, the concrete is playing the role of the fluid and the steel fibers account for

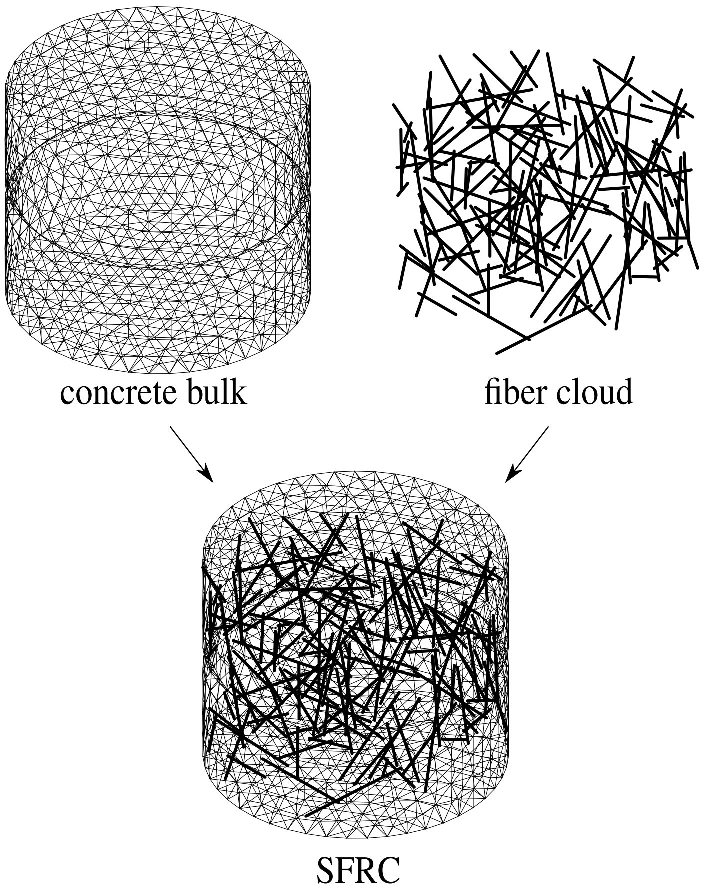

Figure 5.1: Meshes corresponding to the concrete bulk, the fiber cloud and SFRC

the solid structure immersed in the concrete.

The meshes discretizing the concrete bulk and the fiber cloud are nonconformal (without geometrical matching), as shown in figure 5.1.

The mesh corresponding to the fiber cloud is defined accounting for the actual geometry of each fiber (namely, steel fibers can be distributed and orientated randomly) and overlapping the domain occupied by the concrete bulk. Moreover, the steel fibers are assumed to be one dimensional bars. On the contrary, the concrete domain is discretized considering 3 dimensional meshes (figure 5.1).

Once the two domains are discretized, the problem to be solved is the same as the one described in chapter 4.

5.2.2 Concrete bulk material

For modeling the concrete bulk, any nonlinear material adequate for describing the brittle behavior of plain concrete in tension can be chosen. Both models presented in chapter 3 are useful for modeling the concrete bulk in the presented numerical tool for SFRC.

5.2.3 Fiber cloud model

The phenomenological mesomodel chosen for modeling the fiber cloud (introduced in chapter 4) accounts not only for the steel fibers behavior, but also for the whole concrete-fiber interaction behavior.

The proposed idea is to translate the analytical expressions describing the outputs of the pullout tests (defined by Laranjeira et al. (2010a,b)) into the constitutive equations of each fiber of the fiber cloud. Namely, the crack width (w) and the vertical load (P) of the pullout tests are translated into the strains (ε) and stresses (σ) corresponding to the constitutive equations of the fibers:

$$\begin{aligned} P &\rightarrow \sigma \\ w &\rightarrow \varepsilon \end{aligned} \tag{5.1}$$

The translation of (w, P) into (ε, σ) is done taking into account the area and the length of the fibers. Note that the outputs of the pullout tests are in the axis of the same test and the constitutive equations of the fibers (ε, σ) must be in the axis of the fiber. Thus, it is necessary to change the reference axis of the system (see expressions 4.7). The whole description of the constitutive equations is presented in Appendix A.

The pullout response depends on the inclination of the fiber immersed in the concrete matrix. Therefore, the analytical expressions of the pullout outputs depend on the angle between the fiber and the vertical load. Thus, for each fiber in the cloud, the angle between the fiber and the normal direction of the crack is computed and, depending on this angle, the constitutive equation is calculated (through the corresponding pullout response).

The outputs of the pullouts are also different depending on the shape of the fiber (in Appendix A both straight and hooked fibers are described). Therefore, the constitutive equations of the fibers also depend on their shape. Thus, the shape of each fiber is not defined geometrically, but inside its constitutive equation.

5.3 Implementation and computational aspects

In order to apply the numerical approach presented in the previous section, some implementation and computational aspects must be taken into account.

The constitutive equation of each fiber in the fiber cloud depends on the angle between the fiber and the normal direction of the failure pattern, as introduced in the previous section. Therefore, before simulating a test considering SFRC, the same test is simulated with only plain concrete (for example, modeling plain concrete with the nonlocal Mazars damage model) for knowing the failure pattern. Once the failure pattern is known, the normal direction is computed and, afterwards, the angle of all the fibers in the fiber cloud. Figure 5.2 illustrates the angle computation (θ) between the fiber and the normal direction of the failure pattern ($\mathbf{n}$).

If the failure pattern is composed by multiple cracks, with the same normal direction or not, for computing the angle of each fiber and the normal direction of the failure pattern, the position of each fiber must be known. Given the position, the angle is computed depending on the failure pattern in the current position of the fiber.

For distributing and orienting the steel fibers randomly into the concrete bulk domain, the uniform probability distribution function is used in order to calculate the coordinates of initial points and angles.

For each initial point, p_i, and two angles, φ and ϕ, given randomly, with a fixed fiber length (L), the final point is defined following the equation (5.2).

$$p_f = p_i + (L \cdot \cos\varphi \cdot \cos\phi, L \cdot \sin\varphi \cdot \cos\phi, L \cdot \sin\varphi \cdot \sin\phi) \tag{5.2}$$

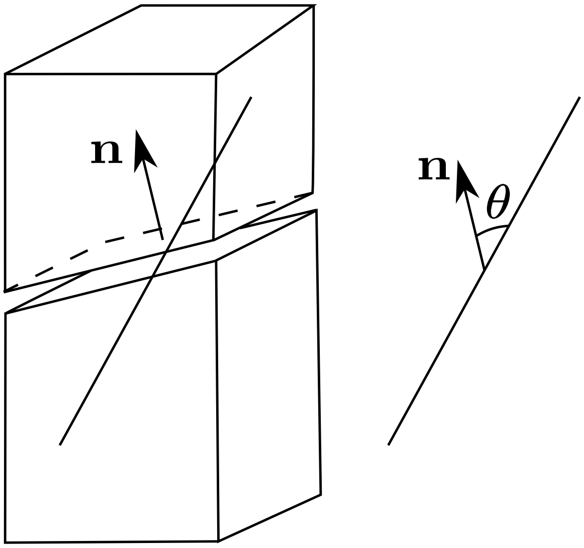

Figure 5.2: Computation of the angle between the fiber and the normal direction of the crack.

Therefore, given the coordinates of the initial point (p_i) and the final point (p_f), the fiber is defined with its two end-points.

If the fiber location parameters are such that the fiber is not included in the concrete bulk, then the values of φ and ϕ are iteratively modified to find a proper configuration (for example, considering equations (5.3)). Experimentally, these fibers are reoriented due to the wall effect.

$$\varphi = \varphi - 10^o \tag{5.3a}$$

$$\phi = \phi - 10^o \tag{5.3b}$$

All the numerical simulations of SFRC must be under the hypotheses of large displacements and deformations in order to capture the residual strength of the material due to the presence of the fibers. On the contrary, the effect of the fibers into the material is not reproduced.

For each fiber, in order to compute its constitutive equation (on the basis of the outputs of the pullout tests, see Appendix A), the corresponding embeded length,

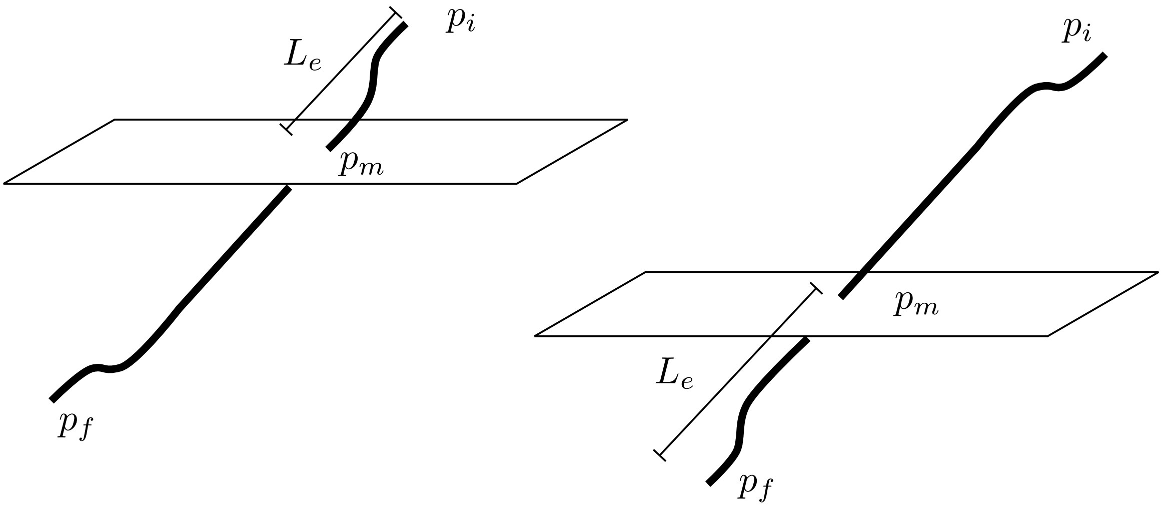

Figure 5.3: Computation of the embeded length.

L_e, must be known. Therefore, given the fiber, the intersection point (p_m) of the fiber with the crack is calculated. The embeded length (L_e) is defined as the shortest distance between one end-point of the fiber (p_i or p_f) and the intersection point (p_m) (equation (5.4)), as illustrated in figure 5.3.

$$L_e = \min(d(p_i, p_m), d(p_f, p_m)) \tag{5.4}$$

5.4 Experimental data

In order to validate the numerical tool for modeling SFRC, two three dimensional examples are simulated. The numerical results are compared with those obtained experimentally.

One direct tension test is studied (defined on the basis of RILEM-TC162-TDF (2001)) and, for analyzing the flexural behavior of SFRC, a flexural test is reproduced, the three point bending test (EN-14651 (2005)). The experimental results are from Laranjeira (2010) and Guàrdia (2007), respectively.

In both cases, the geometry and the material properties of the steel fibers are the

Table 5.1: Steel fibers geometry and mechanical properties

Length (L)	60 mm
Diameter (d)	0.75 mm
Aspect ratio (L/d)	80
Tensile yield strength (f_y)	2000 MPa

same, because they belong to the same experimental program. Moreover, the material characteristics of plain concrete are common in both tests too.

Steel fibers are of Dramix® RC 80/60 BP with circular cross-section and hooked ends. Fibers are made of high carbon steel and gathered into bundles by water-soluble glue. The main properties of the steel fibers are summarized in table 5.1.

For the constitutive equations of the steel fibers, the outputs of the pullout tests from Laranjeira et al. (2010b) (hooked fibers) are needed. However, the geometry of the fibers used by Laranjeira et al. (2010b) (presented in table A.2) is not the same that the geometry of the fibers used in the presented experimental campaigns (table 5.1). Therefore, the inputs used for the current fibers geometry are taken from the results presented by Blàzquez (2009).

Blàzquez (2009) reproduced pullouts considering both straight and hooked fibers with the same geometry as the fibers used in the experimental campaigns (presented in table 5.1). The obtained results are sumarized in figure 5.4 and correspond to the inputs used for the constitutive equations of the fibers. These inputs are used for calculating the pullout outputs following the equations presented by Laranjeira et al. (2010b) (see Appendix A).

Different fiber contents are considered: 20Kg/m^3 and 40Kg/m^3, which correspond to 0.25% and 0.5% volumetric substitution amount of fibers, respectively.

The concrete used in both experimental campaigns is selfcompacting and its mechanical properties are shown in table 5.2.

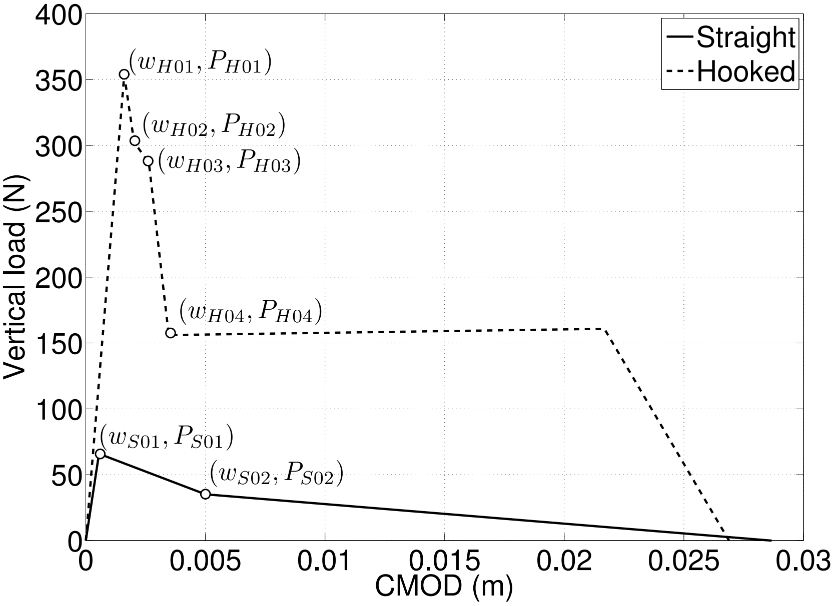

Figure 5.4: Inputs for the constitutive equations of the fibers.

Table 5.2: Concrete mechanical properties

Young modulus (E)	$35.5 \cdot 10^3$ MPa
Poisson ratio (μ)	0.25
Compressive strength ($\mathrm{f_c}$)	48.5 MPa
Tensile strength ($\mathrm{f_t}$)	3.84 MPa

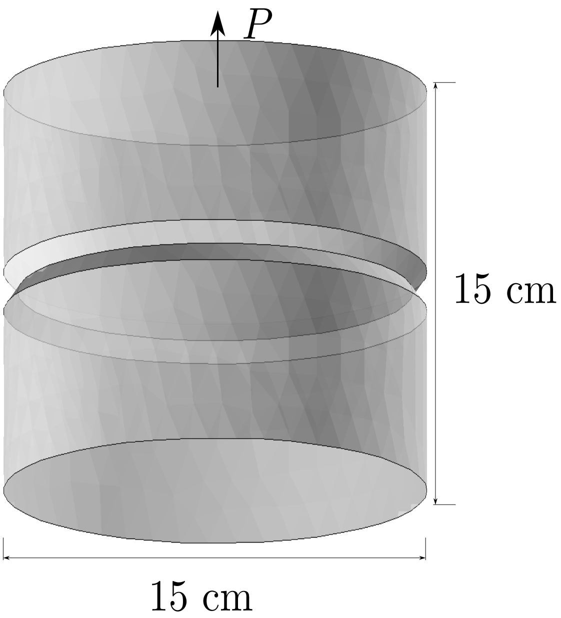

Figure 5.5: Direct Tension Test scheme

5.5 Numerical Examples

Before simulating the tests with SFRC, they are simulated considering only plain concrete modeled through the nonlocal Mazars damage model. Then, the failure pattern of the test is known for (a) computing the normal direction of the failure pattern and, therefore, the angle of each fiber and the normal direction and (b) simulating the same test, but with the discontinuous model for the concrete bulk.

In all the simulations, each fiber is discretized considering 5 straight bar elements of 12mm length (all the fibers are 60mm length).

5.5.1 Direct Tension Test

The direct tension test, illustrated in figure 5.5, consists of a cylindric specimen (made of plain concrete or SFRC) with a circumferential notch of 5mm width and 15mm depth to localize the crack, axially loaded according to RILEM-TC162-TDF (2001, 2003c,d).

The mesh corresponding to the concrete specimen is composed by tetrahedral

Table 5.3: Concrete material parameters of the nonlocal Mazars damage model for the direct tension test

parameter	value
Y_0	$1.08 \cdot 10^{-4}$
l_{car}	10^{-3} m
A_t	1.2
B_t	2500
A_c	1
B_c	266

elements. The minimum value corresponding to the length of the edges is 6.5mm, the maximum value is 28.5mm and the mean value is 15mm. Thus, each element of the fibers corresponds almost to one element of the concrete mesh.

Without taking into account the steel fibers, the test is carried out considering plain concrete modeled with the nonlocal Mazars damage model. The material parameters used in this simulation are presented in table 5.3, these parameters are chosen on the basis of the model and according to the geometry of the test, as presented in section 3.3.1 (see figure 3.5).

The damage distribution at the failure is presented in figure 5.6. Moreover, the normal direction of the failure pattern is computed observing the damage distribution, as also displayed in figure 5.6.

The distribution of the fibers into the concrete matrix of the direct tension test is represented in figure 5.7. For this test, two different fiber contents are considered: 20Kg/m^3 and 40Kg/m^3.

Continuous model for plain concrete

As a first approach, the plain concrete is modeled considering the nonlocal Mazars damage model and the material parameters are presented in table 5.3.

Figure 5.8 shows the obtained load-displacement curve of the direct tension test considering hooked SFRC with different amount of fibers. The displacement displayed in the load-displacement curve corresponds to the crack mouth opening displacement

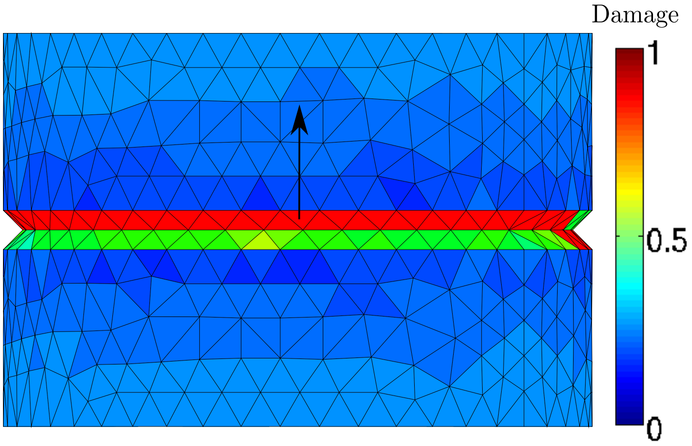

Figure 5.6: Fracture pattern and the normal direction for the direct tension test (damage distribution)

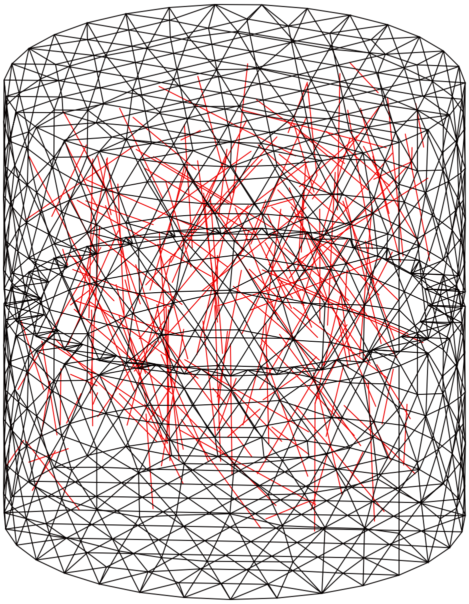

Figure 5.7: Fiber distribution in the direct tension test specimen for the case with 20Kg/m^3 in the concrete bulk.

(CMOD). It its observed that after cracking (after reaching the peak load), the load drops and then it increases again, corresponding to the residual strength due to the fibers. Moreover, for a larger amount of fibers, the residual strength is higher.

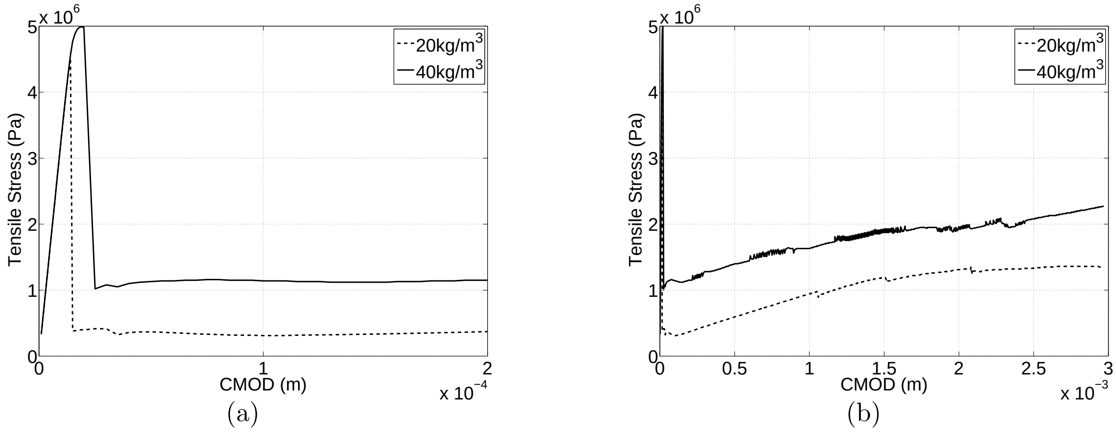

Figure 5.8: Direct Tension Test considering hooked SFRC with the nonlocal Mazars damage model: (a) zoom and (b) whole load-displacement curve.

In the load-CMOD diagrams, some jumps appear in both cases (20Kg/m^3 and 40Kg/m^3). Such jumps correspond to the collapse of one element of the concrete mesh (the element is completely damaged) which includes the end of one fiber bridging the crack.

Discontinuous model for plain concrete

On the other hand, the discontinuous model for plain concrete is considered and the chosen parameters are presented in table 5.4 on the basis of section 3.3.2. and considering the direct tension test geometry.

The same fiber distribution and orientation as in the continuous model is considered, for both cases of fiber contents.

In figure 5.9 the obtained results are presented considering the direct tension test with hooked fibers, considering different contents. As expected, hardening is observed after the load drop produced when the specimen cracks.

Table 5.4: Joint parameters for the concrete in the direct tension test

parameter	value
E	$30 \cdot 10^9 \mathrm{N/m^2}$
k_{n1}	$E/0.001 \mathrm{N/m^3}$
k_{n2}	$-E \mathrm{N/m^3}$
u_0	$(3.84 \cdot 10^6)/(30 \cdot 10^9)\mathrm{m}$
k_s	$E/0.001 \mathrm{N/m^3}$
f_t	$6 \cdot 10^6 \mathrm{N/m^2}$
c	$50 \cdot 10^6 \mathrm{N/m^2}$
φ	90^o

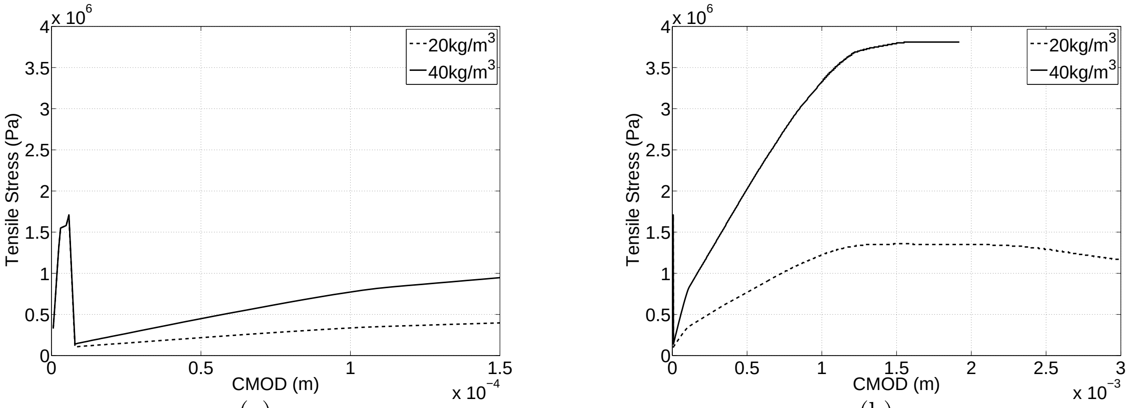

(a) (b)

Figure 5.9: Direct Tension Test considering hooked SFRC with the joint model model: (a) Zoom and (b) whole load-displacement curve.

Test validation

Figures 5.10 and 5.11 show the results obtained numerically (considering both the continuous and the discontinuous model for the concrete bulk) compared to the experimental ones for 20 and 40 Kg/m^3, respectively.

The overall response of the numerical results, considering both models for describing the concrete behavior, qualitatively fits with the experimental results.

Comparing the numerical results between them, it is observed that they are very similar and they both capture the real behavior: after the load drop, a hardening

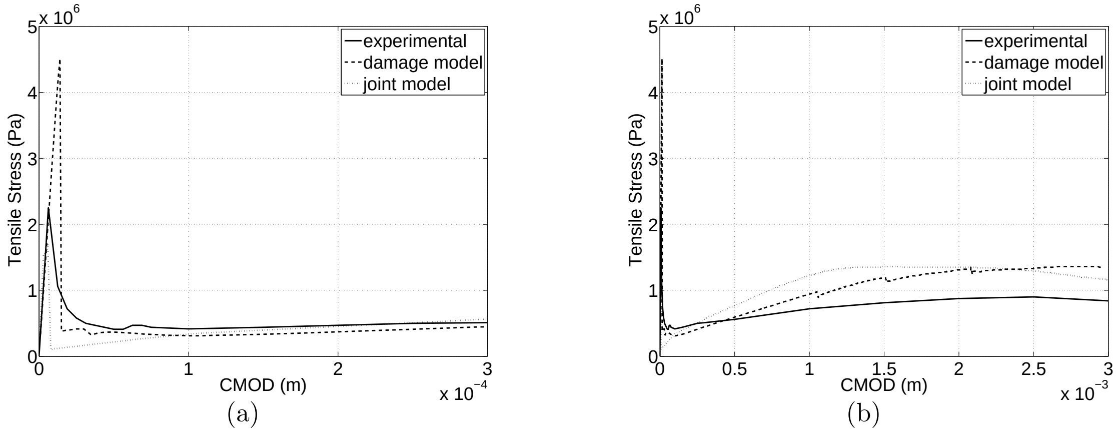

(a) (b)

Figure 5.10: Experimental and numerical results: direct tension test with 20Kg/m^3: (a) zoom and (b) whole load-displacement curve.

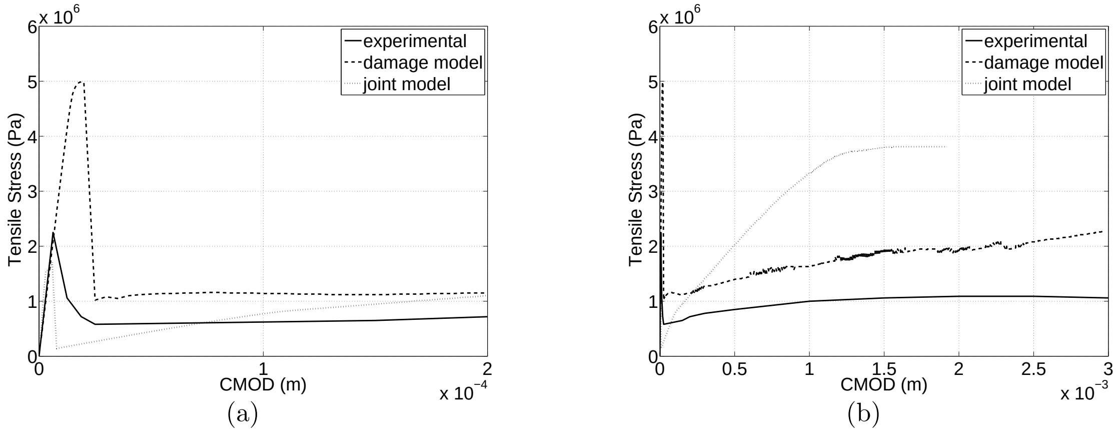

(a) (b)

Figure 5.11: Experimental and numerical results: direct tension test with 40Kg/m^3: (a) zoom and (b) whole load-displacement curve.

occurs due to the residual strength given by the fibers and, after reaching a CMOD of 10^{-3}m, the load stabilizes and becomes almost constant.

Referring the maximum value of the tensile stress, for the case with 20Kg/m^3 of fibers, the case corresponding to the joint model (1.8MPa) is closer to the experimental value (2.2MPa), than the nonlocal Mazars damage model (4.5MPa). The same behavior is reproduced for the case with 20Kg/m^3 of fibers: the maximum value of the tensile stress obtained experimentally is 2.2MPa and the numerical values are

5MPa and 1.1MPa, corresponding to the continuous model and the discontinuous one, respectively.

Observing figure 5.10, the maximum value of the residual strength obtained numerically is the same for both models: 1.3MPa, while the value obtained experimentally is 0.9MPa. On the other hand, for the case with 40Kg/m^3 of fibers, the experimental maximum value of the residual strength is 1.05MPa, while the maximum value obtained with the nonlocal Mazars damage model is 2.05MPa. The maximum value of the residual strength corresponding to the joint model for the plain concrete is 3.81MPa.

Moreover, considering the nonlocal Mazars damage model, the residual strength obtained for the case with 40Kg/m^3 of fibers is not twice the residual strength corresponding to the case of 20Kg/m^3, as expected, because the model captures some fibers interaction, when they are anchored in the same element.

Observing the area defined below each curve, the energy dissipation can be studied. For the case with 40Kg/m^3 of fibers, the energy dissipation is higher than the case with 20Kg/m^3 of fibers.

With the two amounts of fibers, the experimental drop takes place at the same CMOD value of the numerical case considering with the nonlocal damage model. Moreover, the lowest value of the tensile stress after the drop is also close to the experimental one. However, the drop corresponding to the joint model occurs before then in the experimental case and the corresponding tensile strength is lower.

Although the qualitative behavior is captured with the two numerical models, the maximum value of the tensile strength obtained before the drop off is no captured with the damage model. This particular behavior will deserve further research in order to obtain a satisfactory explanation.

5.5.2 Three Point Bending Test

For studying the flexural behavior of the SFRC, the three point bending test is reproduced with the numerical tool proposed in this thesis.

The three point bending test consists of a beam placed horizontally and fixed in two points which is loaded in the middle of the top of the beam, as reproduced in figure 5.12(a), according to RILEM-TC162-TDF (2000, 2003a,b).

The mesh corresponding to the concrete specimen of the three point bending test is composed by prismatic elements (brick elements). The maximum value corresponding to the edge length of the concrete mesh is 15mm and the minimum value is 12.4mm. Thus, each element of the fibers (bars of 12mm length) corresponds to one element of the concrete mesh.

First, the test is simulated considering only plain concrete with the nonlocal Mazars damage model, considering the same material parameters than the direct tension test (presented in 5.3), except the A_t. For this test, A_t is readjusted in order to get a better description of the test. Thus, $A_t = 1$ (instead of $A_t = 1.2$). With the damage distribution, the failure pattern is known and it is possible to calculate its normal direction (as shown in figure 5.12(b)). Given the normal direction, the angle of each fiber of the fiber cloud is computed.

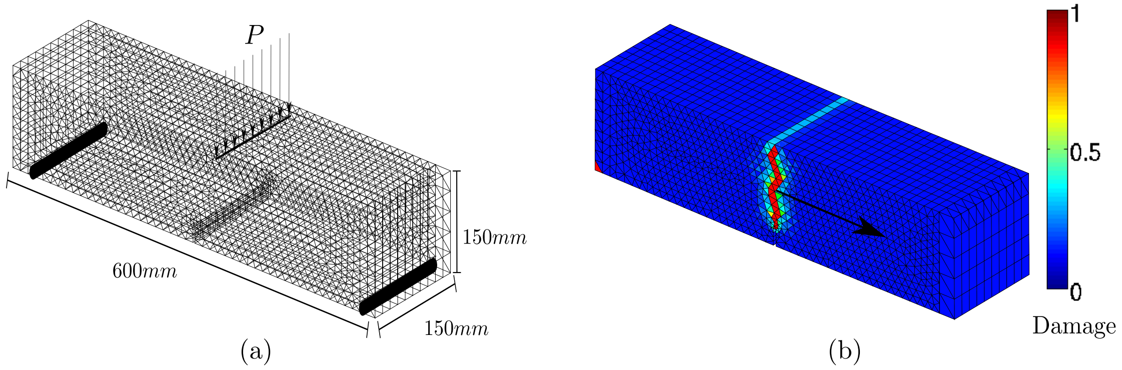

(a) (b)

Figure 5.12: Three point bending test scheme and its failure pattern (damage distribution) and the normal direction

Fibers are randomly distributed and oriented into the concrete bulk domain, as represented in figure 5.14. For this test, only one quantitiy of fibers is considered: 20Kg/m^3. Moreover, apart form the random distribution of the fibers, the same quantity of fibers is considered with all the fibers oriented in the same direction: both

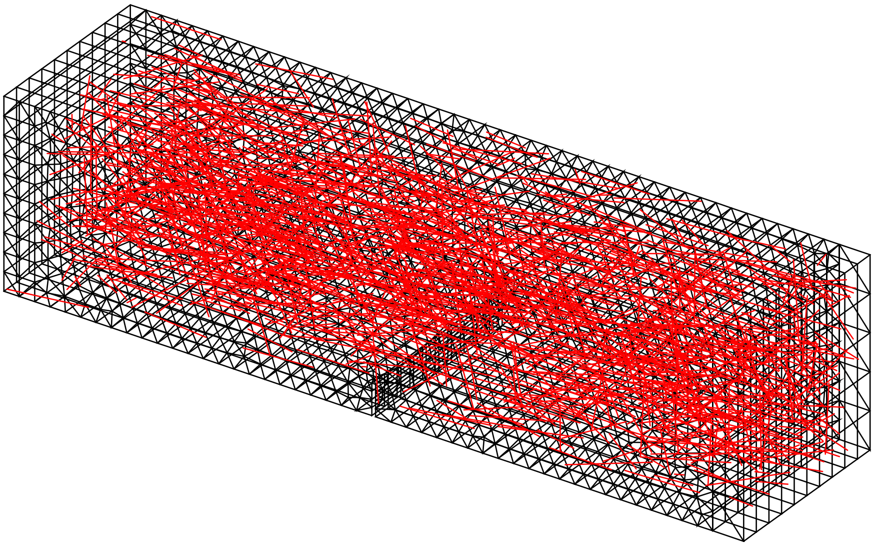

Figure 5.13: Fiber distribution in the specimen for the 3 Point Bending Test with 20Kg/m^3 of fibers randomly distributed and oriented

horizontal fibers (0^o) and inclined fibers (30^o) are considered.

Continuous model for plain concrete

The three point bending test is simulated modeling plain concrete with the nonlocal Mazars damage model (with the material parameters presented in table 5.3).

The obtained load-displacement curves are presented in figure 5.14 considering three different fiber orientation, but the same number of fibers. The displacement plotted is the crack mouth opening displacement (CMOD).

In all the cases, a hardening is observed after the load drop due to the fibers. Moreover, it is observed that the orientation of the fibers does influence on the response of the SFRC. Although the maximum vertical load is the same, the residual strength is higher for the horizontal fibers and with an inclination of 30^o, than for the random distribution. However, the qualitative behavior is the same in the three cases.

The energy dissipation (corresponding to the area behave the curve) is lower when fibers are randomly distributed than for a fixed angle. Moreover, it is higher considering an inclination of 30^o than with horizontal fibers.

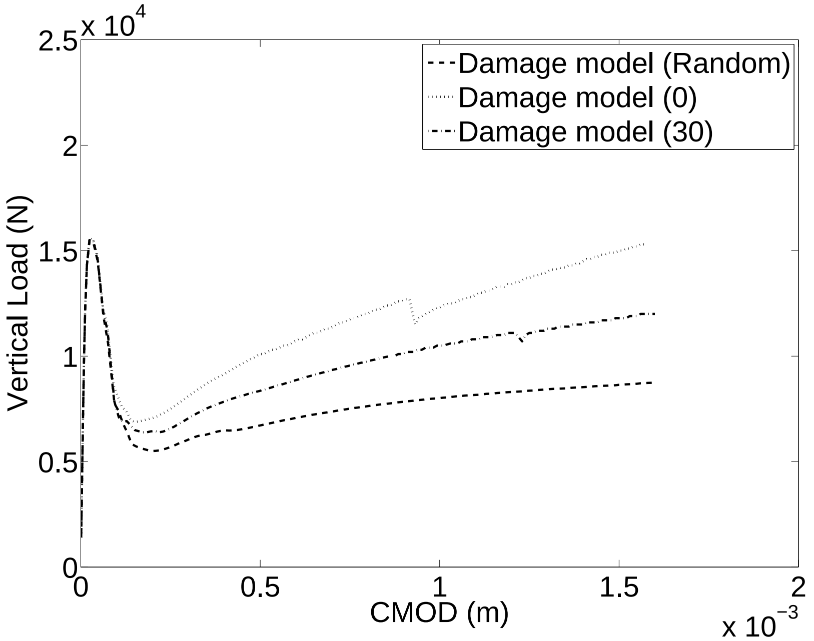

Figure 5.14: Numerical results of the 3 Point Bending Test considering plain concrete and hooked SFRC with the nonlocal Mazars damage model: 20kg/m^3 and 40kg/m^3.

Moreover, figure 5.15 shows the deformed mesh of the test for the case with the random distribution of the fibers.

Test validation

In figure 5.16, the experimental results of the three point bending test considering SFRC with 20kg/m^3 are presented with the numerical ones. For SFRC three cases are considered: (1) the fibers are randomly oriented, (2) all the fibers have $\theta = 0^o$ and (3) all the fibers have $\theta = 30^o$.

It is observed that the presence of the steel fibers is more evident in the experimental results than in the numerical ones. The hardening after the load drop is higher in the experimental campaign than for the numerical results. This is due to the fact that during the numerical simulations, the fiber cloud is generated randomly or with all the fibers with the same orientation. However, experimentally, it has been proved that the steel fibers have preferred orientations inside the concrete bulk. Thus, the

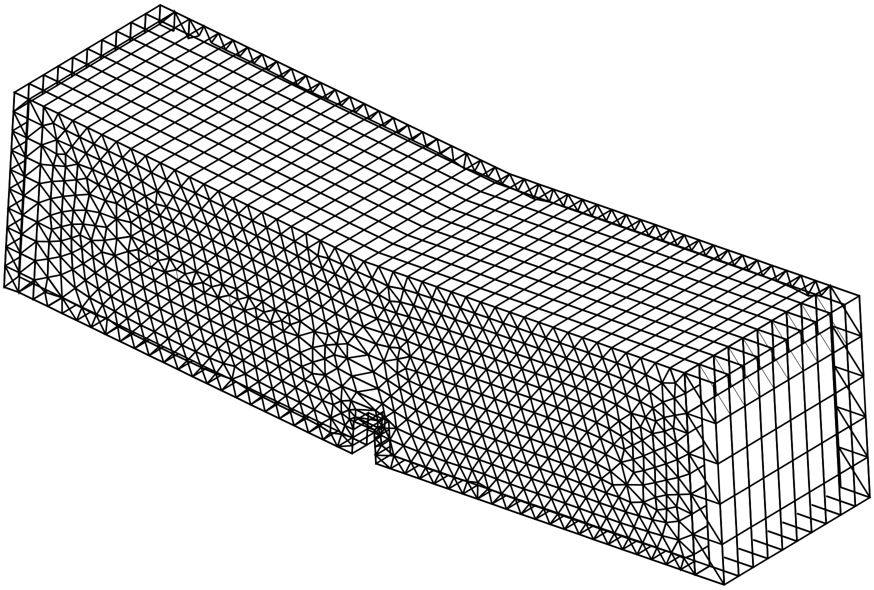

Figure 5.15: Deformed mesh of the 3 Point Bending Test considering hooked SFRC with the nonlocal Mazars damage model and 20kg/m^3 of fibers (aplified x10)

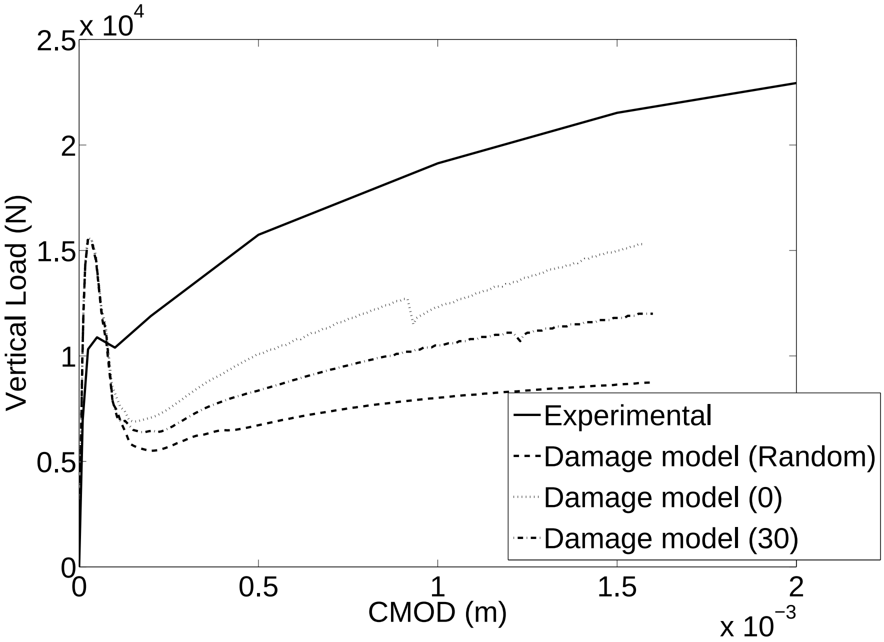

Figure 5.16: Experimental and numerical results: three point bending test with hooked SFRC considering 20kg/m^3 randomly oriented, considering all the fibers with $\theta = 0^o$ and considering all the fibers with $\theta = 30^o$.

numerical results are quite different than the experimental ones.

Moreover, as happened with the direct tension test, the maximum value of the load does not fit with the experimental one. Thus, the material parameters of the damage model should be readjusted for obtaining numerical results closer to the experimental ones.

5.6 Computational limits

Once the two 3D examples are reproduced numerically using the proposed numerical tool, some computational limits appeared. For a large number of fibers, the matrix of the system to be solved at each iteration of the incremental-iterative scheme is large. Thus, the computational cost and time are high.

Each fiber is discretized into 5 elements. Increasing the number of fibers means increasing almost proportionally the computational cost.

In the examples presented in this thesis, in order to reduce the computational cost, only the fibers crossing the failure pattern are included into the system. Although the computational cost is lower, it is not lower enough for large quantities of fibers.

Therefore, an alternative must be considered for being able to simulate larger and more realistic structures with SFRC considering the presented numerical approach.

An alternative which has been devised is to consider the idea presented by Pros et al. (2008) in which the system is solved following a block Gauss-Seidel strategy.

5.7 Concluding remarks

In this chapter, a numerical tool for simulating three dimensional SFRC tests which allows accounting for the actual geometry of the fibers into the concrete specimen is presented.

Both the concrete bulk and the fiber cloud are discretized nonconformally. The two materials are coupled imposing displacement compatibility between them. The concrete bulk can be modeled considering any nonlinear material. On the other hand, the mesomodel considered to be the constitutive model of the fiber cloud not only describes the steel fibers behavior, but also accounts for the interaction behavior between the fiber cloud and the concrete bulk.

Two realistic examples are reproduced using the proposed tool.

The tool is validated comparing the obtained results (numerically) with the experimental results from two different experimental campaigns.

The influence of the fibers is observed in the results of the 3D examples because: (1) the energy dissipation and (2) the residual strength increase comparing to the results obtained simulating the same tests with only plain concrete. For a higher number of fibers into the plain concrete, the energy dissipation and the residual strength of the SFRC is higher.

All the numerical results presented in this thesis are obtained generating the fiber cloud randomly. However, preferred orientations are observed in the SFRC specimens used in the experimental campaigns (for the direct tension test (Laranjeira et al. (2008); Laranjeira (2010)) and the three point bending test (Molins et al. (2008))). Therefore, the numerical results obtained taking into account these preferred orientations of the fibers should fit better with the experimental results.

The proposed tool for SFRC allows both to generate randomly the fiber cloud and to define the fiber cloud with a preferred orientation and distribution of the fibers.

Fixing the constitutive equations before the simulation on the basis of the fracture pattern known *a priori*, do not allow to take into account the change of the crack pattern due to the presence of the fibers. An improvement would be recalculating the angle between each fiber and the normal direction of the failure pattern at different time steps. The normal direction could be calculated as the gradient of the damage field.

However, for a large number of fibers, the computational cost is too high. Therefore, we should seek an alternative to solve efficiently the system of the problem.

Up to now, the presented examples have a fracture pattern well defined and with only one crack. The next step is to reproduce a test with SFRC with a fracture pattern not so easy to describe, for example the Barcelona Test (described by Molins et al.

(2009)). The used technique is the same, but it is necessary to take into account the position of each fiber and the corresponding normal direction to the failure pattern in this current position.

Chapter 6

Summary

6.1 Concluding remarks

The main conclusions of this thesis are drawn at the end of each chapter (chapters 3, 4 and 5). However, the most salient results are summarized below.

- Two different material models are studied for modeling plain concrete: (1) the nonlocal Mazars damage model and (2) a discontinuous model with the fracture pattern (known *a priori*) modeled considering joint elements, while the rest of the specimen is assumed to be elastic. Both the Brazilian test and the Double Punch Test are simulated considering the two models. The numerical results are validated through experimental results, after calibrating the material parameters. Although in chapter 3 only two tests are reproduced, the parametric study is useful also for all the other tests. Therefore, two nonlinear alternatives for modeling plain concrete are available with the corresponding parameter description.

- The main contribution of this thesis is the numerical approach for modeling SFRC. It is characterized by accounting for the actual geometry of the fibers inside the concrete matrix. It is possible to take into account the real position of the fibers and the preferred orientations of the fibers, if they are available. Moreover, the meshes corresponding to the concrete bulk and the fiber cloud are nonconformal (without geometrical matching). The material models corresponding to the concrete bulk and the fiber cloud are defined independently, but they are coupled enforcing displacement compatibility between them. A phenomenological mesomodel is chosen for describing the constitutive equations of the steel fibers accounting not only for the fibers behavior, but also for the whole concrete-fiber interaction behavior. The proposed phenomenological mesomodel for the fibers is defined on the basis of analytical expressions from the outputs of pullout tests (defined by Laranjeira et al. (2010a,b)). Thus, these constitutive equations depend on (1) the shape of the fiber, (2) the experimental results of an aligned pullout test, and (3) the angle between the fiber and the failure pattern of the concrete specimen. Therefore, each fiber of the fiber cloud has a different constitutive equation. Both the two models studied in the first part of the thesis for modeling plain concrete can be applied for modeling the concrete bulk in the proposed tool for SFRC.

- The proposed numerical tool is extended to 3D meshes. Therefore, different standard tests are reproduced numerically considering SFRC. For all the tests, in order to define the constitutive model for each fiber, the angle between the fiber and the failure pattern must be known before the simulation. Thus, before considering SFRC, the test is reproduced considering only plain concrete in order to know the failure pattern *a priori*. Precisely, plain concrete is modeled with the nonlocal Mazars damage model. Once the angle of each fiber is know and, consequently, the constitutive equations of the fibers are defined, the tests are reproduced numerically considering SFRC.

- The presence of the steel fibers into the concrete matrix is evidenced with the increase of the energy dissipation and the residual strength of the material (observed in the load-displacement curves). Moreover, it has been proved that the shape of the fibers influences on the effect of the SFRC: the residual strength is higher for hooked fibers than for straight fibers. The quantity of fibers composing the fiber cloud also influences on the behavior of SFRC: increasing the number of fibers means increasing the residual strength of the material.

- 3D examples are simulated considering SFRC under the same conditions than in different experimental campaigns (namely, one for the direct tension test and the other for the three point bending test). Then, the numerical results are compared to the experimental ones. Therefore, the numerical tool is validated experimentally.

6.2 Future work

The work carried out in this thesis leaves some open research lines that will be studied in the near future. We suggest the following points:

- We find interesting to study the influence of the preferred angle orientations for the three point bending test. Up to now, the numerical results are obtained considering random distributions and orientations of the fibers into the concrete matrix. However, experimentally, it has been proved that the orientations of the fibers into the concrete specimen have preferred directions for this specific example (due to the geometry of the specimen used for this test). Therefore, it would be interesting to generate the fiber cloud following the ideas presented by Molins et al. (2008); Laranjeira (2010) (instead of generate it randomly). The obtained results should fit better with those obtained experimentally. Given the results considering both randomly distributed and oriented fibers and real distributions of the fibers, it would be necessary to analyze the influence of the fiber orientation and distribution (apart from comparing the numerical results with the experimental ones).

- The numerical results calculated considering the proposed numerical approach should be compared to other numerical results obtained on the basis of different numerical tools for modeling SFRC available in the literature. For example, it would be interesting to define a test under the same conditions and carry out the simulation considering the ideas presented by Oliver et al. (2011); Radtke et al. (2011, 2010a). Moreover, apart from comparing the outputs of the numerical simulations (deformed meshes, load-displacement curves, energy dissipation, residual strength,etc.), the computational costs (for the mesh generation and for the whole simulation), the efficiency, the realism of the meshes,... should be analyzed and compared too.

- All the examples presented in this thesis with SFRC (pullout tests, direct tension test and three point bending test) have a common characteristic: its failure pattern presents only one crack. Therefore, it would be interesting to simulated standard tests with SFRC with more complex failure patterns or with multiple cracks, such as the Barcelona Test (namely, the extension of the Double Punch Test with SFRC). In the case of more complex failure patterns, the angle between each fiber and the failure pattern depends on the position of the fiber. However, once the angle of each fiber is defined, the rest of the process is the same.

- It would be interesting to study the changes of the failure pattern due to the presence of the fibers into the plain concrete. Therefore, instate of defining the constitutive equations of the fibers once before the simulation, these equations could be recalculated at different time steps during the simulation. In this case, the normal direction of the failure pattern at these time steps could be defined as the gradient of the current damage field.

- The proposed tool for modeling SFRC has been validated through different standard tests and their corresponding experimental campaigns. However, for a large quantity of fibers in the concrete bulk, the matrix of the system to be solved at each iteration of each incremental step of the incremental-iterative scheme is large and, consequently, the computational cost is high. Each fiber is discretized considering 5 elements, therefore, increasing the number of fibers means increasing proportionally the number of degrees of freedom of the system. Thus, an alternative for solving the system and, therefore, reducing the computational cost is necessary. As a first measure to reduce the computational cost, applied in the 3D examples presented in this thesis, only the fibers crossing the cracks are considered during the simulation. However, this measure is not enough to reduce the costs for large quantities of fibers. An alternative would be follow the strategy presented by Pros et al. (2008) in which, instead of consider the monolithic idea, the system is solved considering a block Gauss-Seidel method.

Appendix A

Parametrization of the constitutive equations for steel fibers

For a given steel fiber, its constitutive equation is calculated without taking into account the other fibers. The computation of the equations is based on the results from the pullout tests, which are presented in Laranjeira (2010), Laranjeira et al. (2010a) and Laranjeira et al. (2010b). The analytical expressions deduced from the pullout tests are different for each fiber shape (straight or hooked), therefore, the two different cases are presented independently.

Straight fibers

For a given steel fiber, once the angle between this fiber and the normal direction of the failure pattern, ϕ, is computed the corresponding constitutive equation is calculated. Based on Laranjeira et al. (2010a), the constitutive equations are defined phenomenologically considering five points (ε_i, σ_i), as presented in figure A.1.

Input data for the phenomenological model include fibers properties as fiber diameter (d), fiber length (L) and shorter fiber embedded length within the concrete matrix (L_e); concrete properties as the average tensile strength (f_{ctm}); experimental results of the aligned fiber pullout test (w_{S01}, P_{S01}) and (w_{S02}, P_{S02}); numerical parameters as the element size of the fiber (L_{elem}) and the area of the fiber (A_{fiber}); and, finally, the friction coefficient (μ) and the number of sides of the cracked section at

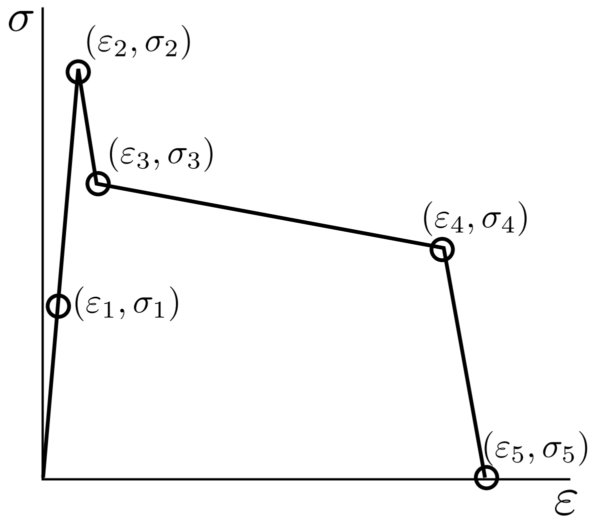

Figure A.1: Phenomenological constitutive equation of a straight fiber defined by five points

which spalling of the matrix occurs sensitive to fiber orientation (N).

Considering all the input parameters, the five points are defined:

- $\varepsilon_1 = \dfrac{w_{S01} \cos\phi}{L}$

  $\sigma_1 = \dfrac{P_{S01}}{A_{\text{fiber}}}$

- $\varepsilon_2 = \varepsilon_1 + \dfrac{(w_{S01} \cos\phi + \frac{L_d}{L_e}(w_{S02} - w_{S01}) \cos\phi + \Delta w_{SP1}) \cos\phi}{L_{\text{elem}}} - \dfrac{w_{S01} \cos\phi}{L_{\text{elem}}}$

  $\sigma_2 = \dfrac{P_{S01} \cos\phi L_{\text{eff}}(\frac{L_e - L_d}{L_e} + \frac{P_{S02} L_d}{P_{S01} L_e}) + \mu D_{F1}}{A_{\text{fiber}} \cos\phi}$

- $\varepsilon_3 = \varepsilon_1 + \dfrac{(w_{S02} \cos\phi + \Delta w_{SP1}) \cos\phi}{L_{\text{elem}}} - \dfrac{w_{S01} \cos\phi}{L_{\text{elem}}}$

  $\sigma_3 = \dfrac{P_{S02} \cos\phi L_{\text{eff}} + \mu D_{F1}}{A_{\text{fiber}} \cos\phi}$

- $\varepsilon_4 = \varepsilon_1 + \dfrac{(L_e - (L_{SP1} + d)) \cos\phi}{L_{\text{elem}}} - \dfrac{w_{S01} \cos\phi}{L_{\text{elem}}}$

  $\sigma_4 = \dfrac{\mu D_{F1}}{A_{\text{fiber}} \cos\phi}$

- $\varepsilon_5 = \varepsilon_1 + \dfrac{(L_e - L_{SP1})\cos\phi}{L_{\text{elem}}} - \dfrac{w_{S01}\cos\phi}{L_{\text{elem}}}$

  $\sigma_5 = 0$

- being
  - L_{SP1} the matrix spalled length which satisfies $aL_{SP1}^2 + bL_{SP1} + c = 0$ with $a = \dfrac{\sqrt{2}}{\sin\phi} + \dfrac{\cos\phi}{\sin^2\phi}$, $b = \dfrac{d}{\sin\phi}$ and $c = -\dfrac{P_{S01}\sin\phi}{f_{ctm}}$
  - $L_d \approx 6L_{SP1}$ if $6L_{SP1} \leq L_e$. Otherwise, $L_d = L_e$
  - $\Delta w_{SP1} = NL_{SP1}(1 - \cos\phi)$
  - $L_{\text{eff}} = \dfrac{L_e - L_{SP1}}{L_e}$
  - $D_{F1} = P_{S01}\sin\phi\cos\frac{\phi}{2}$

For the examples studied in the present work, the input parameters used are presented in table A.1, as introduced in Laranjeira et al. (2010a).

Table A.1: Input parameters for straight fibers

P_{S01}(N)	P_{S02}(N)	w_{S01}(mm)	w_{S02}(mm)	d(mm)	L_e(mm)	f_{ctm}(MPa)	μ	N
44.9	12	0.05	0.4	0.5	10	2.8	0.6	1

Hooked fibers

As in the previous case, for hooked fibers, the constitutive equations are also defined depending on the angle (ϕ) and considering different points. However, due to the fiber shape, the interaction is more complex than for the straight fibers. Therefore, eight points (ε_i, σ_i) are required for describing the constitutive equations, as shown in figure A.2, as presented in Laranjeira et al. (2010b).

Input data for the phenomenological model include fibers properties as fiber diameter (d), fiber length (L), shorter fiber embedded length within the concrete matrix

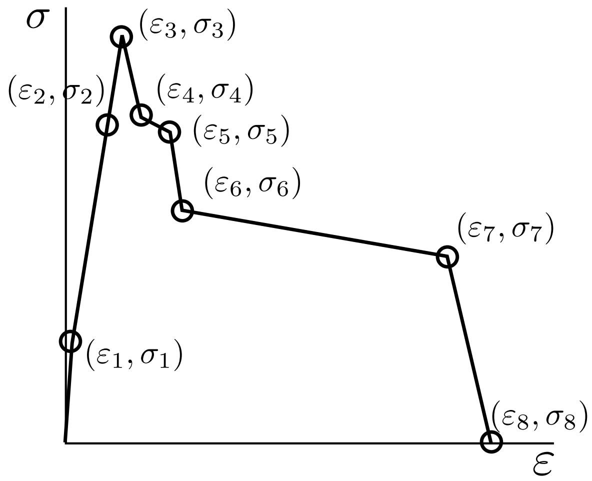

Figure A.2: Phenomenological constitutive equation of a hooked fiber defined by eight points

(L_e) and the ultimate tensile strength of aligned steel fibers (σ_u); concrete properties as the average tensile strength (f_{ctm}); experimental results of the aligned fiber pullout test (w_{S01}, P_{S01}) and (w_{S02}, P_{S02}); experimental information from pullout test derived from the direction of the original embedded part of the fiber (w_{H01}, P_{H01}), (w_{H02}, P_{H02}), (w_{H03}, P_{H03}) and (w_{H04}, P_{H04}); numerical parameters as the element size of the fiber (L_{elem}) and the area of the fiber (A_{fiber}); and, finally, the friction coefficient (μ),the number of sides of the cracked section at which spalling of the matrix occurs sensitive to fiber orientation (N) and a parameter taking into account the pullout test configuration (κ).

Considering all the input parameters, the eight points are defined:

- $\varepsilon_1 = \dfrac{w_{S01}\cos\phi}{L}$

  $\sigma_1 = \dfrac{P_{S01}}{A_{\text{fiber}}}$

- $\varepsilon_2 = \varepsilon_1 + \dfrac{(w_{S01} + \Delta w_{H01}\cos\phi\frac{L_e - 6\cdot L_{SP1}}{L_e} + \Delta w_{SP1})\cos\phi}{L_{\text{elem}}} - \dfrac{w_{S01}\cos\phi}{L_{\text{elem}}}$

  $\sigma_2 = \dfrac{(P_{S01}L_{\text{eff}(H2)} + \Delta P_{H01}\frac{L_e - 6\cdot L_{SP1}}{L_e})\cos\phi + \mu D_{F1}}{A_{\text{fiber}}\cos\phi}$

- $\varepsilon_3 = \varepsilon_1 + \dfrac{(w_{S01} + \Delta w_{H01}\cos\phi + \Delta w_{SP1} + \Delta w_{SP2})\cos\phi}{L_{\text{elem}}} - \dfrac{w_{S01}\cos\phi}{L_{\text{elem}}}$

$$\sigma_3 = \frac{(P_{S01}L_{\text{eff}(H3)} + \Delta P_{H01})\cos\phi + \mu D_{F2}}{A_{\text{fiber}}\cos\phi}$$

- $\varepsilon_4 = \varepsilon_1 + \varepsilon_3 + \dfrac{\Delta w_{H02}\cos^2\phi}{L_{\text{elem}}} - \dfrac{w_{S01}\cos\phi}{L_{\text{elem}}}$

  $$\sigma_4 = \frac{(P_{S01}L_{\text{eff}(H4)} + \sum\limits_{i=1}^{2}\Delta P_{H0i})\cos\phi + \mu D_{F2}}{A_{\text{fiber}}\cos\phi}$$

- $\varepsilon_5 = \varepsilon_1 + \varepsilon_4 + \dfrac{\Delta w_{H03}\cos^2\phi}{L_{\text{elem}}} - \dfrac{w_{S01}\cos\phi}{L_{\text{elem}}}$

  $$\sigma_5 = \frac{(P_{S01}L_{\text{eff}(H5)} + \sum\limits_{i=1}^{3}\Delta P_{H0i})\cos\phi + \mu D_{F2}}{A_{\text{fiber}}\cos\phi}$$

- $\varepsilon_6 = \varepsilon_1 + \varepsilon_5 + \dfrac{\Delta w_{H04}\cos^2\phi}{L_{\text{elem}}} - \dfrac{w_{S01}\cos\phi}{L_{\text{elem}}}$

  $$\sigma_6 = \frac{(P_{S02}L_{\text{eff}(H6)} + \sum\limits_{i=1}^{4}\Delta P_{H0i})\cos\phi + \mu D_{F2}}{A_{\text{fiber}}\cos\phi}$$

- $\varepsilon_7 = \varepsilon_1 + \dfrac{(L_e - (L_{SP1} + L_{SP2} + d))\cos\phi}{L_{\text{elem}}} - \dfrac{w_{S01}\cos\phi}{L_{\text{elem}}}$

  $$\sigma_7 = \frac{(\sum\limits_{i=1}^{4}\Delta P_{H0i})\cos\phi + \mu D_{F2}}{A_{\text{fiber}}\cos\phi}$$

- $\varepsilon_8 = \varepsilon_1 + \dfrac{(L_e - (L_{SP1} + L_{SP2}))\cos\phi}{L_{\text{elem}}} - \dfrac{w_{S01}\cos\phi}{L_{\text{elem}}}$

  $\sigma_8 = 0$

- being
  - L_{SP1} the matrix spalled length defined for straight fibers
  - L_{SP2} the increment of spalled matrix along fiber axis which satisfies $aL_{SP2}^2 + bL_{SP2} + c = 0$ with $a = \dfrac{\sqrt{2}}{\sin\phi} + \dfrac{\cos\phi}{\sin^2\phi}$, $b = \dfrac{d}{\sin\phi} + \dfrac{2L_{SP1}(\cos\phi + \sqrt{2})}{\sin\phi}$ and $c = (-\dfrac{P_{S01}\sin\phi}{f_{ctm}})\dfrac{P_{H01}}{P_{S01}} + \dfrac{L_{SP1}}{\sin\phi}(d + L_{SP1}\dfrac{\cos\phi}{\sin\phi})$
  - $\Delta P_{H01} = P_{H01} - P_{S01}$ and $\Delta w_{H01} = w_{H01} - w_{S01}$

- for $i = 1, 2, 3$, $\Delta P_{H0(i+1)} = P_{H0(i+1)} - P_{S0i}$ and $\Delta w_{H0(i+1)} = w_{H0(i+1)} - w_{S0i}$
- The effective length factors at each key point H_i are defined as

$$\begin{aligned}
L_{\text{eff}(H2)} &= \frac{L_e - L_{SP1}}{L_e} \\
L_{\text{eff}(H3)} &= \frac{L_e - (L_{SP1} + L_{SP2})}{L_e} \\
L_{\text{eff}(H4)} &= \frac{L_e - (L_{SP1} + L_{SP2} + \Delta w_{H02})}{L_e} \\
L_{\text{eff}(H5)} &= \frac{L_e - (L_{SP1} + L_{SP2} + \sum_{i=2}^{3} \Delta w_{H0i})}{L_e} \\
L_{\text{eff}(H6)} &= \frac{L_e - (L_{SP1} + L_{SP2} + \sum_{i=2}^{4} \Delta w_{H0i})}{L_e}
\end{aligned}$$

- $D_{F1} = P_{S01} \sin\phi \cos\frac{\phi}{2}$ and $D_{F2} = P_{H01} \sin\phi \cos\frac{\phi}{2}$
- $\Delta w_{SP1} = N L_{SP1}(1 - \cos\phi)$ and $\Delta w_{SP2} = L_{SP2}(1 - \cos\phi)$

For the examples studied in the present work, the input parameters used are presented in table A.2, as introduced in Laranjeira et al. (2010b).

Table A.2: Input parameters for hooked fibers

P_{S01}(N)	P_{S02}(N)	w_{S01}(mm)	w_{S02}(mm)	d(mm)	L_e(mm)	f_{ctm}(MPa)
25	12.5	0.035	0.3	0.5	20	4.46

σ_u(MPa)	μ	N	κ	P_{H01}(N)	w_{H01}(mm)
1150	0.6	1	9	192	0.769

P_{H02}(N)	w_{H02}(mm)	P_{H03}(N)	w_{H03}(mm)	P_{H04}(N)	w_{H04}(mm)
110	2.6	90	4.5	65	5

Appendix B

Stability of the Lagrange multipliers

In this thesis, a numerical approach for modeling Steel Fiber Reinforced Concrete is presented. Imposing the proposed coupling between the fiber cloud and the concrete bulk means solving a discrete system:

$$\begin{bmatrix} K_c & 0 & \Pi^{\mathsf{T}} \\ 0 & K_s & -I_s \\ \Pi & -I_s & 0 \end{bmatrix} \begin{bmatrix} u_c \\ u_s \\ \widetilde{\lambda} \end{bmatrix} = \begin{bmatrix} F_c^{\text{ext}} \\ F_s^{\text{ext}} \\ 0 \end{bmatrix}, \tag{B.1}$$

being $\widetilde{\lambda}$ the Lagrange Multipliers.

The system B.1 corresponds to the unrealistic case where both the concrete bulk and the fiber cloud are supposed to be elastic. However, it is enough for studying the stability of the proposed approach.

This system (equation B.1) is the discrete version of a continuous system:

- Concrete equilibrium ($\boldsymbol{u}_C \in \Omega$):

$$\begin{aligned} -\nabla \cdot \boldsymbol{\sigma}(\boldsymbol{u}_C) &= \boldsymbol{b}_C + \boldsymbol{f}_{S\to C} && \text{in } \Omega \\ \boldsymbol{\sigma}(\boldsymbol{u}_C) \cdot \boldsymbol{n} &= g_N && \text{on } \Gamma_N \\ \boldsymbol{u}_C &= \boldsymbol{u}_{\boldsymbol{D}} && \text{on } \Gamma_D \end{aligned} \tag{B.2}$$

with the corresponding weak form:

$$\int_{\Omega} \nabla \boldsymbol{v}_C : \boldsymbol{\sigma}(\boldsymbol{u}_C) d\Omega = \int_{\Omega} \boldsymbol{v}_C \boldsymbol{b}_C d\Omega + \int_{\widetilde{\Omega_S}} \lambda \boldsymbol{v}_C|_{\widetilde{\Omega_S}} d\widetilde{\Omega_S} + \int_{\Gamma_N} \boldsymbol{v}_C g_N d\Gamma_N \quad \forall \boldsymbol{v}_C \in H^1(\Omega) \tag{B.3}$$

- Fiber equilibrium ($\boldsymbol{u}_S \in \widetilde{\Omega_S}$):

$$-\nabla \cdot \boldsymbol{\sigma}(\boldsymbol{u}_S) \ = \boldsymbol{f}_{C\rightarrow S} \quad \text{in } \widetilde{\Omega_S} \tag{B.4}$$

with the corresponding weak form:

$$\int_{\widetilde{\Omega_S}} \nabla \boldsymbol{v}_S : \boldsymbol{\sigma}(\boldsymbol{u}_S) d\widetilde{\Omega_S} = \int_{\widetilde{\Omega_S}} \lambda \boldsymbol{v}_S d\widetilde{\Omega_S} \quad \forall \boldsymbol{v}_S \in H^1(\widetilde{\Omega_S}) \tag{B.5}$$

- Displacement compatibility:

$$\boldsymbol{u}_C|_{\widetilde{\Omega_S}} = \boldsymbol{u}_S \quad \text{in } \widetilde{\Omega_S} \tag{B.6}$$

with the corresponding weak form:

$$\int_{\widetilde{\Omega_S}} \mu(\boldsymbol{u}_S - \boldsymbol{u}_C|_{\widetilde{\Omega_S}}) d\widetilde{\Omega_S} \quad \forall \mu \in H^{-1/2}(\widetilde{\Omega_S}) \tag{B.7}$$

Therefore, considering $\boldsymbol{u}^* = (\boldsymbol{u}_C, \boldsymbol{u}_S)$ and $\boldsymbol{v}^* = (\boldsymbol{v}_C, \boldsymbol{v}_S)$, the weak form of the system can be written as:

$$\begin{array}{cc} a(\boldsymbol{u}^*, \boldsymbol{v}^*) + b(\boldsymbol{v}^*, \lambda) = l(\boldsymbol{v}^*) & \forall \boldsymbol{v}^* \in H^1(\Omega) \times H^1(\widetilde{\Omega_S}) \\ b(\boldsymbol{u}^*, \mu) = 0 & \forall \mu \in H^{-1/2}(\widetilde{\Omega_S}) \end{array} \tag{B.8}$$

with

$$\begin{array}{rcc} a(\boldsymbol{u}^*, \boldsymbol{v}^*) & = & \int_{\Omega} \nabla \boldsymbol{v}_C : \boldsymbol{\sigma}(\boldsymbol{u}_C) d\Omega + \int_{\widetilde{\Omega_S}} \nabla \boldsymbol{v}_S : \boldsymbol{\sigma}(\boldsymbol{u}_S) d\widetilde{\Omega_S} \\ b(\boldsymbol{u}^*, \mu) & = & \int_{\widetilde{\Omega_S}} \mu(\boldsymbol{u}_S - \boldsymbol{u}_C|_{\widetilde{\Omega_S}}) d\widetilde{\Omega_S} \\ l(\boldsymbol{v}^*) & = & \int_{\Omega} \boldsymbol{v}_C \boldsymbol{b}_C d\Omega + \int_{\Gamma_N} \boldsymbol{v}_C g_N d\Gamma_N \end{array} \tag{B.9}$$

Although during this thesis no instability problems occurred in the simulations using the proposed approach, an study of the stability of the Lagrange Multipliers is needed.

The inf-sup condition (already known as Ladyzhenskaya-Babuŝka-Brezzi (LBB) condition (Brezzi (1974))) allows demonstrating the stability of the Lagrange Multipliers (Bathe et al. (2000)).

In the following, a general problem is formulated with the inf-sup condition.

General form of the exact problem:

Given $b : X \times M \mapsto \mathbb{R}$ bilinear form, $a(.,.) : X \times X \mapsto \mathbb{R}$, $g \in M$ and $X^g := \{\boldsymbol{v} \in X : b(\boldsymbol{v}, \mu) = (g, \mu), \forall \mu\}$, find the solution $(\boldsymbol{u}, \lambda) \in X \times M$ of

$$\begin{cases} a(\boldsymbol{u}, \boldsymbol{v}) + b(\boldsymbol{u}, \lambda) = l(\boldsymbol{v}) >, \forall \boldsymbol{v} \in X \\ b(\boldsymbol{u}, \mu) = (g, \mu), \forall \mu \in M \end{cases} \tag{B.10}$$

being f the imposed constrains and λ the corresponding Lagrange Multipliers.

Discrete approximation:

Find u_H and λ_H such that

$$\begin{aligned} \boldsymbol{u} &\approx u_H \in X_H \subset X \\ \lambda &\approx \lambda_H \in M_H \subset M \end{aligned} \tag{B.11}$$

are the solution of the discrete problem corresponding to B.10:

$$\begin{cases} a_H(u_H, v_H) + b_H(u_H, \lambda_H) = l_H(u_H) >, \forall v_H \in X_H \\ b_H(u_H, \mu_H) = (g_H, \mu_H), \forall \mu_H \in M_H \end{cases} \tag{B.12}$$

Ladyzhenskaya-Babuŝka-Brezzi (LBB) theorem:

If $\exists \beta^* \geq 0$ such that

$$\inf_{\mu \in M_H} \sup_{\boldsymbol{v} \in X_H} \frac{b(\boldsymbol{v}, \mu)}{\|\mu\|_M \|\boldsymbol{v}\|_X} \geq \beta^*, \tag{B.13}$$

then the solution of the problem is stable.

In the continuous problem proposed above, we can assume

$$\begin{aligned} X &= H^1(\Omega) \times H^1(\widetilde{\Omega_S}) \\ M &= \quad H^{-1/2}(\widetilde{\Omega_S}) \end{aligned} \tag{B.14}$$

and

$$\|\boldsymbol{v}^*\|^2 = \|\boldsymbol{v_c}\|^2_{H^1(\Omega)} + \|\boldsymbol{v_s}\|^2_{H^1(\widetilde{\Omega_S})}. \tag{B.15}$$

Therefore, if $\exists \beta^* \geq 0$ such that

$$\inf_{\mu \in H^{-1/2}(\widetilde{\Omega_S})} \sup_{\boldsymbol{v}^* \in H^1(\Omega) \times H^1(\widetilde{\Omega_S})} \frac{b(\boldsymbol{v}^*, \mu)}{\|\mu\|_{H^{-1/2}(\widetilde{\Omega_S})} \|\boldsymbol{v}^*\|_{H^1(\Omega) \times H^1(\widetilde{\Omega_S})}} \geq \beta^* \tag{B.16}$$

the proposed coupling though the Lagrange multipliers is stable.

Numerical inf-sup test:

In some cases, it is difficult to identify whether the inf-sup condition is satisfied. Thus, Bathe et al. (2000) propose some numerical tests, easier to perform, for studying the stability of a problem. Although a numerical tool is no as encompassing as an analytical proof, their experience is that when a numerical test is passed, the inf-sup condition is satisfied.

In the same direction, Béchet et al. (2009) introduce an algorithm to define a stable Lagrange multiplier space to impose stiff interface conditions in the context of the eXtended Finite Element Method (XFEM).

Both Bathe et al. (2000) and Béchet et al. (2009) use a numerical inf-sup test proposed by Chapelle and Bathe (1993) and detailed by Brezzi and Fortin (1991). This test reduces to the computation of eigenvalues for a sequence of meshes of increasing density and it is presented in the following.

Given a discrete system

$$\begin{pmatrix} \boldsymbol{A} & \boldsymbol{B}^{\mathsf{T}} \\ \boldsymbol{B} & \mathbf{0} \end{pmatrix} \begin{pmatrix} \boldsymbol{u} \\ \lambda \end{pmatrix} = \begin{pmatrix} \boldsymbol{f} \\ 0 \end{pmatrix}, \tag{B.17}$$

with $\boldsymbol{A}$ standing for the stiffness matrix associated with the Laplace operator and $\boldsymbol{B}$ corresponding to the coupling matrix, the value of β^* is the minimum of μ (non-zero and positive) in the following generalized eigenvalue problem:

$$\boldsymbol{B}^{\mathsf{T}}\boldsymbol{K_M}^{-1}\boldsymbol{B}\boldsymbol{w} = \mu^2\boldsymbol{K_X}\boldsymbol{w} \tag{B.18}$$

being $\boldsymbol{w}$ the eigenvector and μ the eigenvalue.

Moreover, $\boldsymbol{K_M}$ and $\boldsymbol{K_X}$ are the matrix associated to the norm of the spaces M and X, respectively.

The stability of β^* is checked on a sequence of meshes, with respect to h, which corresponds to the element size of each concrete mesh.

In the proposed coupling, based on the system presented in B.1,

$$\begin{aligned} \boldsymbol{A} &= \begin{pmatrix} K_c & \mathbf{0} \\ \mathbf{0} & K_s \end{pmatrix} \\ \boldsymbol{B} &= \begin{pmatrix} \Pi^{\mathsf{T}} & -I_s \end{pmatrix}. \end{aligned} \tag{B.19}$$

Moreover, K_M is the matrix associated to the norm of the space $H^{-1/2}(\widetilde{\Omega_S})$, which is similar to the L_2 norm, and K_X is the matrix associated to the metric of $H^1(\Omega) \times H^1(\widetilde{\Omega_S})$, corresponding to the energy norm. Thus,

$$\begin{aligned} \boldsymbol{K_M} &= diag(\frac{1}{L}, \frac{2}{L}, ..., \frac{2}{L}, \frac{1}{L}) \\ \boldsymbol{K_X} &= \boldsymbol{A} \end{aligned} \tag{B.20}$$

being L the length of the elements of the fibers.

For studying the stability of the problem, the inf-sup test is applied. Thus, it is necessary to find the minimum eigenvalue μ (non zero and positive) such that

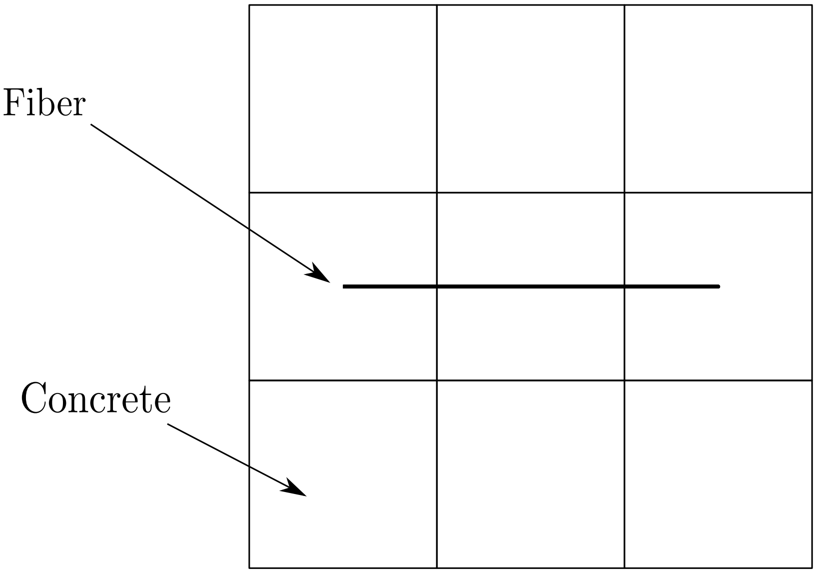

Figure B.1: Concrete domain and fiber

$$(\boldsymbol{B}^{\mathsf{T}}(diag(\frac{1}{L},\frac{2}{L},...,\frac{2}{L},\frac{1}{L}))^{-1}\boldsymbol{B})\overline{\lambda} = \mu^2\boldsymbol{A}\overline{\lambda} \tag{B.21}$$

considering different meshes for both the concrete domain and the fibers.

Numerical test for the proposed tool

Considering a plain concrete domain with a fiber immersed on it, as presented in figure B.1, the stability of the Lagrange multipliers is studied through the inf-sup test.

Four different nested meshes are considered in order to find the minimum eigenvalue of B.21 and the results are presented in figure B.2. It is possible to observe that the values of $\log_{10}(\mu)$ converge to a number different from zero. Therefore, the inf-sup test is passed.

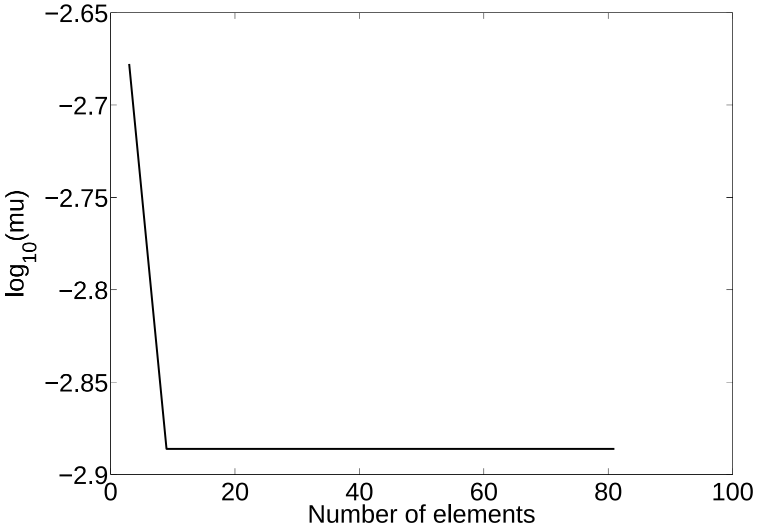

Figure B.2: Obtained values of $\log_{10}(\mu)$ for different nested meshes

Appendix C

Most important related contributions

C.1 Participations in congresses

Numerical modeling of a test assessing the tensile strength of Steel Fiber Reinforced Concrete
Alba Pros, Pedro Díez and Climent Molins
8th. World Congress on Computational Mechanics (WCCM8) 5th European Congress on Computational Methods in Applied Sciences and Engineeering (ECCOMAS 2008)
June 30 - July 5, 2008
Venice, Italy

Simulación numérica del ensayo Barcelona para hormigón reforzado con fibras de acero
Alba Pros, Pedro Díez and Climent Molins
Congreso de métodos numéricos en ingeniería 2009
June 29 - July 2, 2009
Barcelona, Spain

Model validation of the numerical simulation of the Double Punch Test
Alba Pros, Pedro Díez and Climent Molins
IV European Conference on Computational Mechanics (ECCM 2010)

May 16-21, 2010
Paris, France

Numerical Modeling for Steel Fiber Reinforced Concrete: Flexural Behavior
Alba Pros, Pedro Díez and Climent Molins
CFRAC 2011 - International Conference on Computational Modeling of Fracture and Failure of Materials and Structures
June 6-8, 2011
Barcelona, Spain

Numerical simulation of steel fiber reinforced concrete: including fibers into plain concrete
Alba Pros, Pedro Díez and Climent Molins
CMNE 2011 - Congress on Numerical Methods in Engineering
June 14-17, 2011
Coimbra, Portugal

Discrete meso-modeling of Steel Fiber Reinforced Concrete: simulation of flexural behavior
Alba Pros, Pedro Díez and Climent Molins
COMPLAS XI - XI International Conference on Computational Plasticity Fundamentals and Applications
September 7-9, 2011
Barcelona, Spain

Simulación numérica de hormigón reforzado con fibras de acero
Alba Pros, Climent Molins and Pedro Díez
V Congreso de ACHE (Asociación Cientifico-Técnica del Hormigón Estructural)
October 25-27, 2011
Barcelona, Spain

C.2 Publications

A. Pros, P. Díez and C. Molins. **Numerical modeling of double punch test for plain concrete.** International Journal of solids and structures (2011). Vol. 48 (7-8), 1229 - 1238.

A. Pros, P. Díez and C. Molins. **Modeling steel fiber reinforced concrete: numerical immersed boundary approach and a phenomenological mesomodel for concrete-fiber interaction**. International Journal for Numerical Methods in Engineering (2011). Accepted for publication.

A. Pros, C. Molins and P. Díez. **3D numerical modeling of steel fiber reinforced concrete with experimental validation**. In preparation.

Bibliography

ASTMC-1018 (1992). Standard test method for flexural toughness and first-crack strength of fiber-reinforced concrete (using beam with third-point loading). *American Society for Testing and Materials, Philadelphia.*

Balakrishnan, S. and D. Murray (1986). Finite element prediction of reinforced concrete behavior. *Structural Engineering Report 138*, (www.uofaweb.ualberta.ca/structures/pdfs/SER138BalakrishnanandMurray.pdf).

Barragán, B. E. (2002). *Failure and toughness of steel fiber reinforced concrete under tension and shear.* Ph. D. thesis, Universitat Politècnica de Catalunya.

Bathe, K. J., A. Iosilevich, and D. Chapelle (2000). An inf-sup test for shell finite elements. *Computers and Structures 75*, 439–456.

Bažant, Z. P. (2002). Concrete fracture models: testing and practice. *Engineering Fracture Mechanics 69*, 165–205.

Bažant, Z. P. and B. H. Oh (1983). Crack band theory for fracture of concrete. *Materials and Structures 16*(3), 155–177.

Béchet, E., N. Moës, and B. Wohlmuth (2009). A stable lagrange multiplier space for stiff interface conditions within the extended finite element method. *International Journal for Numerical Methods in Engineering 78*, 931–954.

Beer, G. (1985). An isoparametric joint/interface element for finite element analysis. *International Journal For Numerical Methods in Engineering 21*, 585–600.

Blàzquez, X. (2009). Caracterització experimental de l'arrencament de fibres d'acer en provetes de formigó. Master's thesis, Univeristat Politècnica de Catalunya.

Boffi, D. and L. Gastaldi (2003). A finite approach of the immersed boundary method. *Computers and Structures 81*, 491–501.

Boffi, D., L. Gastaldi, and L. Heltai (2007). On the cfl condition for the finite element immersed boundary method. *Computers and Structures 85*, 775–783.

Bortolotti, L. (1988). Double-punch test for tensile and compressive strengths in concrete. *IACI Materials Journal 85-M4*, 26–32.

Brezzi, F. (1974). On the existence, uniqueness and approximation of saddle-point problems arising from lagrangian multipliers. *Revue française d'automatique, informatique, recherche opérationelle, Analyse numérique 8*(2), 129–151.

Brezzi, F. and M. Fortin (1991). *Mixed and Hybrid Finite Element Method.* Springer-Verlag.

Carmona, S., R. Gettu, and A. Aguado (1998). Study of the post-peak behavior of concrete in the splitting-tesnion test. In H. Mihashi and K. Rokugo (Eds.), *FRAMCOS 3, Fracture Mechanics of Concrete Structures, Gifu (Japan), October 12-16*, pp. 111–120. AEDIFICANDO, Felburg, Alemania.

Carneiro, F. L. and A. Barcelos (1953). Tensile strength of concretes. *Rilem Bulletin. Union of Testing and Research Laboratories for Materials and Structures, Paris 13*, 97–123.

Chapelle, D. and K. J. Bathe (1993). The inf-sup test. *Computers and Structures 47*, 537–545.

Chau, K. T. and X. X. Wei (2000a). Finite solid circular cylinders subjected to arbitrary surface load. part i: Analytic solution. *International Journal of Solids and Structures 37*, 5707–5732.

Chau, K. T. and X. X. Wei (2000b). Finite solid circular cylinders subjected to arbitrary surface load. part ii: Application to double-punch test. *International Journal of Solids and Structures 37*, 5733–5744.

Chen, W. F. (1970). Double punch test for tensile strength of concrete. *ACI Mater J. 67 (2)*, 993–995.

Chen, W. F. and B. E. Tumbauer (1972). Double-punch test and tensile strength of concrete. *Journal of Materials, American Society of testing and materials. 7 (2)*, 148–154.

Chen, W. F. and R. L. Yuan (1980). Tensile strength of concrete: Double punch test. *Journal of structural divisions, ASCE. 106*, 1673–1693.

Díez, P. and P. Pegon (2002). Error assessment of structural computations including joints. In *Proceedings of the Fifth World Congress on Computational Mechanics, Vienna, Austria.*

Elwi, A. and T. Hrudey (1989). Finite element model for curved embedded reinforcement. *Journal of Engineering Mechanics 115*, 740–754.

Elwi, A. and D. W. Murray (1980). Nonlinear analysis of axisymmetric reinforced concrete structures. *Structural Engineering Report (University of Alberta, Edmonton, Alberta, Canada) 87.*

EN-14651 (2005). Test method for metallic fibred concrete. measuring the flexural tensile strength (limit of proportionality (lop), residual). *European Committee for Standardization, Brussels.*

Guàrdia, J. (2007). Caracterització del comportament a tracció del formigó d'alta treballabilitat reforçat amb fibres d'acer mitjançant l'assaig barcelona. Master's thesis, Univeristat Politècnica de Catalunya.

Hofstetter, G., B. Peer, G. Niederwanger, and G. Fritsche (2005). Numerical simulation of ultimate load tests on fiber reinforced concrete beams. In *VIII International Conference on Computational Plasticity (COMPLAS VIII), Barcelona, Spain.*

Jirásek, M. (1998). Nonlocal models for damage and fracture: comparison of approaches. *International Journal of Solids and Structures 35*(31-32), 4133–4145.

Konig, G. and L. Kutzing (1999). Modelling the increase of ductility of hpc under compressive forces - a fracture mechanics approach. *High performance fiber reinforced cement composites 6*, 251–259.

Laranjeira, F. (2010). *Design-oriented constitutive model for steel fiber reinforced concrete.* Ph. D. thesis, Universitat Politècnica de Catalunya.

Laranjeira, F., A. Aguado, and C. Molins (2008). Evaluating uniaxial tensile behavior of steel fiber reinforced concrete using a meso-scale model. In *Fibre reinforced concrete: design and applications. Proceeding of the Seventh RILEM international Symposium (BEFIB 2008), Chennai, India*, pp. 1055–1064. Publications S. A. R. L.

Laranjeira, F., A. Aguado, and C. Molins (2010a). Predicting the pullout response of inclined straight steel fibers. *Materials and structures 43*, 875–895.

Laranjeira, F., C. Molins, and A. Aguado (2010b). Predicting the pullout response of inclined hooked steel fibers. *Cement and Concrete Research 40*, 1471–1487.

Lilliu, G. and J. G. M. V. Mier (1999). Analysis of crack growth in the brazilian test, in construction materials -theory and application. *Eligehausen R. (Ed.) H. W. Reinhardt 60th birthday commemorative volume*, 123–138.

Lilliu, G. and J. G. M. V. Mier (2003). 3d lattice type fracture model for concrete. *Engineering Fracture Mechanics 70*, 927–941.

López, C. M., I. Carol, and A. Aguado (September 6-10, 1999). Estudio de la fractura del hormigón mediante un modelo numérico micromecánico con elementos junta. In *MECOM 99, Mendoza, Argentina.*

Markeset, G. and A. Hillerborg (1995). Softening of concrete in compression - localization and size effects. *Cement and Concrete Research 25*(4), 702–708.

Marti, P. (1989). Size effect in double-punch test on concrete cylinders. *ACI Materials Journal 86-M58*, 597–601.

Mazars, J. (1986). A description of micro- and macroscale damage of concrete structures. *Journal of Engineering Fracture Mechanics 25*(5-6), 729–737.

Mittal, R. and G. Iaccarino (2003). Immersed boundary method. *Annu Rev Mech. 37*, 239–261.

Molins, C., A. Aguado, and S. Saludes (2009). Double punch test to control the energy dissipation in tension of frc (barcelona test). *Materials and Structures 42*, 415–425.

Molins, C., A. Aguado, S. Saludes, and T. Garcia (2007). New test to control tension properties of frc. In *ECCOMAS Thematic Conference on Computational Methods in Tunnelling (EURO:TUN 2007), Vienna, Austria.*

Molins, C., J. A. Martínez, and N. Arnáiz (2008). Distribución de fibras de acero en probetas prismáticas de hormigón. In *Congreso internacional de estructuras, IV Congreso, ACHE, Valencia, Spain*, pp. 304–305.

NBN-B-15-238 (1992). Test on fibre reinforced concrete: bending test on prismatic samples. *Institut Belge de Normalisation, Brussels..*

Oliver, J. (2002). Topics on failure mechanics. *International Center for Numerical Methods in Engineering (CIMNE) 68.*

Oliver, J., A. E. Huespe, and J. C. Cante (2008). An implicit/explicit integration scheme to increase computability of non-linear material and contact/friction problems. *Computer Methods in Applied Mechanics and Engineering 197*, 1865–1889.

Oliver, J., A. E. Huespe, and D. F. Mora (2011). Multiscale modeling of fiber reinforced cement composites with microstructure. In *CFRAC: International Conference on Computational Modeling of fracture and failure of Materials and Structures, Barcelona, Spain.*

Oliver, J., A. E. Huespe, M. D. G. Pulido, and E. Chaves (2002). From continuum mechanics to fracture mechanics: the strong discontinuity approach. *Engineering Fracture Mechanics 69*, 113–136.

Oliver, J., D. L. Linero, A. E. Huespe, and O. L. Mansoli (2008). Two-dimensional modeling of material failure in reinforced concrete by means of a continuum strong discontinuity approach. *Computer Methods in Applied Mechanics and Engineering 197*, 332–348.

Phillips, D. and O. Zienkiewicz (1976). Finite element non-linear analysis of concrete structures. *ICE Proceedings 61*(1), 59–88.

Pijaudier-Cabot, G. and Z. P. Bažant (1991). Finite element analysis of bifurcation in nonlocal strain softening solids. *Computer Methods in Applied Mechanics and Engineering 90*, 905–919.

Pijaudier-Cabot, G. and A. Huerta (1991). Finite element analysis of bifurcation in nonlocal strain softening solids. *Computer Methods in Applied Mechanics and Engineering 90*, 905–919.

Planas, J., M. Elices, G. V. Guinea, F. J. Gómez, D. A. Cendón, and I. Arbilla (2003). Generalizations and specifications of cohesive crack models. *Engineering Fracture Mechanics 70*(14), 1759–1776.

Pros, A., P. Díez, and C. Molins (2008). Numerical modeling of a test assessing the tensile strength of steel fiber reinforced concrete. In *8th. World Congress on Computational Mechanics (WCCM8). 5th European Congress on Computational Methods in Applied Sciences and Engineeering (ECCOMAS 2008), Venice, Italy.*

Pros, A., P. Díez, and C. Molins (2011a). Modeling steel fiber reinforced concrete: numerical immersed boundary approach and a phenomenological mesomodel for concrete-fiber interaction. *International Journal for Numerical Methods in Engineering Accepted for publication.*

Pros, A., P. Díez, and C. Molins (2011b). Numerical modeling of double punch test for plain concrete. *International Journal of solids and structures 48*(7-8), 1229–1238.

Radtke, F., A. Simone, and L. Sluys (2010a). A computational model for failure analysis of fibre reinforced concrete with discrete treatment of fibres. *Engineering Fracture Mechanics 77*(4), 497–620.

Radtke, F., A. Simone, and L. Sluys (2010b). A partition of unity finite element method for obtaining elastic properties of continua with embedded thin fibres. *International Journal for Numerical Methods in Engineering 84*(6), 708–732.

Radtke, F., A. Simone, and L. Sluys (2011). A partition of unity finite element method for simulating non-linear debonding and matrix failure in thin fibre composites. *International Journal for Numerical Methods in Engineering 86*(4-5), 453–476.

RILEM-TC162-TDF (2000). Test and design methods for steel fibre reinforced concrete: Bending test. recommendations. *Materials and Structures 33*, 3–5.

RILEM-TC162-TDF (2001). Recommendations of rilem tc 162-tdf: Test and design methods for steel fibre reinforced concrete uniaxial tension test for steel fibre reinforced concrete. *Materials and Structures 34*(235), 3–6.

RILEM-TC162-TDF (2003a). Test and design methods for steel fibre reinforced concrete: Round-robin analysis of the rilem tc 162-tdf beam-bending test: part 1. test method evaluation. *Materials and Structures 36*, 609–620.

RILEM-TC162-TDF (2003b). Test and design methods for steel fibre reinforced concrete: Round-robin analysis of the rilem tc 162-tdf beam-bending test: part 2. approximation of δ from the cmod response. *Materials and Structures 36*, 621–630.

RILEM-TC162-TDF (2003c). Test and design methods for steel fibre reinforced concrete: Round-robin analysis of the rilem tc 162-tdf uni-axial tensile test: part 1. test method evaluation. *Materials and Structures 36*, 265–274.

RILEM-TC162-TDF (2003d). Test and design methods for steel fibre reinforced concrete: Round-robin analysis of the rilem tc 162-tdf uni-axial tensile test: part 2. fibre distribution. *Materials and Structures 36*, 275–280.

RILEM-TC162-TDF (2003e). Test and design methods for steel fibre reinforced concrete: uniaxial tension test for steel fibre reinforced concrete. final recommendations. *Materials and Structures 36*, 560–567.

Rodríguez-Ferran, A. and A. Huerta (2000). Error estimation and adaptivity for nonlocal damage models. *International Journal of Solids and Structures 37*(48-50), 7501–7528.

Schumacher, P. (2006). *Rotation capacity of Self-Compacting Steel Fiber Reinforced Concrete*. Ph. D. thesis, Delft University of Technology.

Simone, A. (2003). *Continuous-Discontinuous Modelling of Failure*. Ph. D. thesis, Technische Universiteit Delft.

Snyman, M. F., W. W. Bird, and J. B. Martin (1991). A simple formulation of a dilatant joint element governed by coulomb friction. *Engineering Computations 8*, 215–229.

Tschegg, E. K. and H. N. Linsbauer (1986). Test method for the determination of fracture mechanics properties. *Patent specification No. A-233/86 390 328, Austrian Patent Office*.

Zhang, J. and V. C. li (2004). Simulation of crack propagation in fiber-reinforced concrete by fracture mechanics. *Cement and Concrete Research 34*, 333–339.